AUGUST 1958 VOLUME 3 (1958) No. 2

GREGG M. SINCLAIR LIBRARY
UNIVERSITY OF HAWAII
8-763

NUCLEAR INSTRUMENTS

A JOURNAL ON ACCELERATORS, INSTRUMENTATION AND TECHNIQUES IN NUCLEAR PHYSICS

EDITOR: K. SIEGBAHN – UPPSALA

CONTENTS

A. M. HOOGENBOOM, A new method in gamma-ray spectroscopy: a two crystal scintillation spectrometer with improved resolution 57
L. BIANCHI, E. COTTON et C. MILEIKOWSKY, Spectromètre pour particules lourdes 69
B. R. F. KENDALL, Direct-coupled amplifier for the measurement of small currents 73
R. W. P. MCWHIRTER, P. PALIT and E. H. BELLAMY, Distinguishing between He^3 and He^4 particles by "dE/dx" and "E" measurements 80
IGOR SAAVEDRA, On the theory of the diffusion cloud chamber 85
NEIL ASHBY, Relativistic theory of the spherical electrostatic analyzer. 90
H. REICH, Das Entkopplungsglied in der Hf-Transmissionslinie eines Mikrotons 97
INGVAR LINDGREN, Investigation of a beta-ray spectrometer with a triangular field 104
J. VAN BLADEL, Fields in slanted-gap excited rectangular ducts. 109
B. COLLINGE and G. B. HUXTABLE, 20 Mc/s scaling circuit 116
S. WAGNER, Umwandlung eines im binären Zahlensystem angezeigten Impulshöhenspektrums in eine registrierte Kurve (Note to the Editor) 119

NORTH-HOLLAND PUBLISHING COMPANY – AMSTERDAM

NUCLEAR INSTRUMENTS

A journal on accelerators, instrumentation and techniques in nuclear physics

EDITOR: K. SIEGBAHN, UPPSALA

EDITORIAL BOARD:

J. B. ADAMS (CERN)
E. AMALDI (Rome)
H. L. ANDERSON (Chicago)
K. T. BAINBRIDGE (Cambridge, Mass.)
C. J. BAKKER (CERN)
P. R. BELL (Oak Ridge)
R. E. BELL (Montreal)
A. BERTHELOT (Saclay)
H. BRINKMAN (Groningen)
E. H. COOKE-YARBOROUGH (Harwell)
S. DE BENEDETTI (Pittsburgh)
M. DE HEMPTINNE (Louvain)
A. DE-SHALIT (Rehovoth)
M. DEUTSCH (Cambridge, Mass.)
S. DU TOIT (Pretoria)
B. S. DŽELEPOV (Leningrad)
W. GENTNER (CERN)
P. C. GUGELOT (Amsterdam)
H. HALBAN (Paris)
O. HAXEL (Heidelberg)
P. HUBER (Basel)
D. J. HUGHES (Brookhaven)
S. KIKUCHI (Tokyo)
J. KOCH (Copenhagen)
M. S. KOZODAEV (Moscow)
S. LIVINGSTON (Cambridge, Mass.)
E. M. MCMILLAN (Berkeley)
M. G. MEŠČERJAKOV (Moscow)
P. B. MOON (Birmingham)
M. L. OLIPHANT (Canberra)
W. PAUL (Bonn)
A. S. RAO (Bombay)
G. SALVINI (Rome)
P. SAVIĆ (Belgrade)
P. SCHERRER (Zürich)
CH. SCHMELZER (CERN)
H. W. B. SKINNER (Liverpool)
R. TANGEN (Blindern)
D. TAYLOR (Harwell)
V. I. VEKSLER (Moscow)
O. WERNHOLM (Stockholm)
G. VON DARDEL (CERN)
R. R. WILSON (Cornell)
S. D. WINTER (Saclay)

Contributions may be sent to the Editor, Professor K. Siegbahn, Institute of Physics, the University of Uppsala, either directly or through the intermediary of one of the members of the Editorial Board of the country or region in which the author is working. Contributions may be written in English, French or German, with an abstract in English.

Books for review should be sent to Professor Siegbahn.

Nuclear Instruments is published monthly. The subscription price of a volume of 360 pages is $ 17.00 (130 s), postage free.

Subscriptions should be sent to the publishers, North-Holland Publishing Company, P.O.Box 103, Amsterdam or to any subscription-agent.

No part of this issue may be reproduced in any form, by print, photoprint, microfilm or any other means without written permission from the publisher. Reprints, photoprints or microfilms are obtainable at cost from the publisher.

A Beta-Ray Spectrometer in commercial production, engineered to highest standards of performance

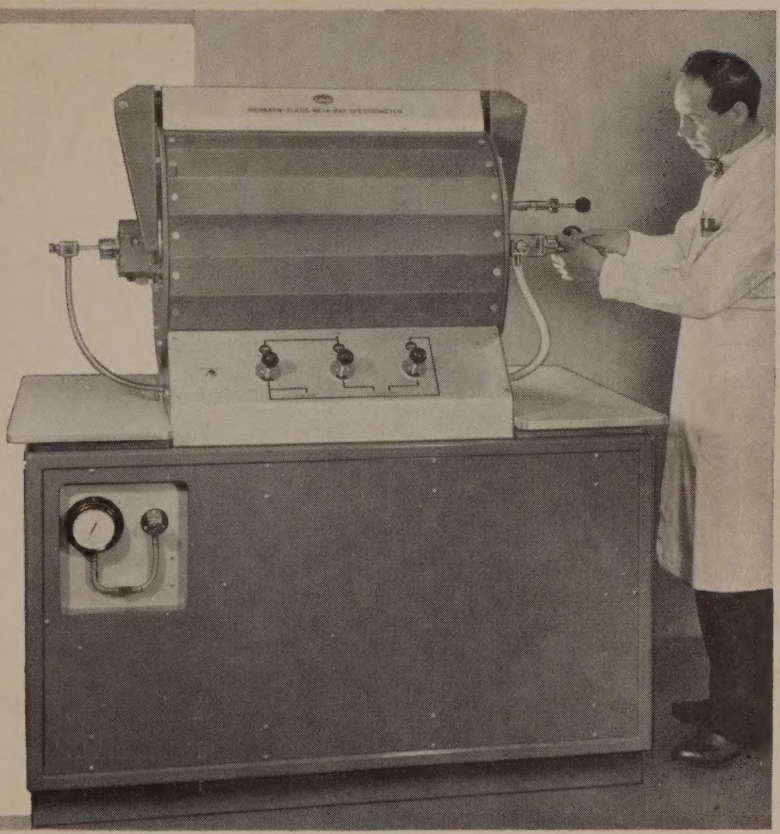

▲ Operator inserting source holder into spectrometer chamber through lock valve. Control console and 50 kW motor-generator set not shown.

The LKB 3024 B Siegbahn-Slätis Intermediate Image Beta-Ray Spectrometer

Features distinguishing the LKB Beta-Ray Spectrometer include:

Energy Range: 1 keV to 8.3 MeV electrons, or, when used as pair spectrometer, up to 17.6 MeV gammas.

Transmission: up to 8% of 4π.

Resolution: 0.7% at 1% transmission or 1.2% at 6% transmission.

Linearity: $B\varrho$ proportional to magnet current within ±0.11% between 36 keV and 8.3 MeV.

Shielding: Spectrometer is iron-jacketed, insuring extremely low stray-field level.

Operation: Safe and fast. There are protective devices against all possible kinds of failure. Precision electronic regulator with follow-up servo facilitates current setting.

To be shown at the Geneva "Atoms for Peace" Exhibition, Sept. 1–14, 1958

Other LKB Products for the Nuclear Physicist:
Custom-built Precision-Stabilized and Transient-Free High Current D. C. Power Supplies.
Autovac Vacuum Gauge.

LKB

Write for details and references to:

LKB-PRODUKTER

Fabriksaktiebolag

P.O. Box 12220, Stockholm 12, Sweden

Distributors throughout the world

Scintillators in 5 forms

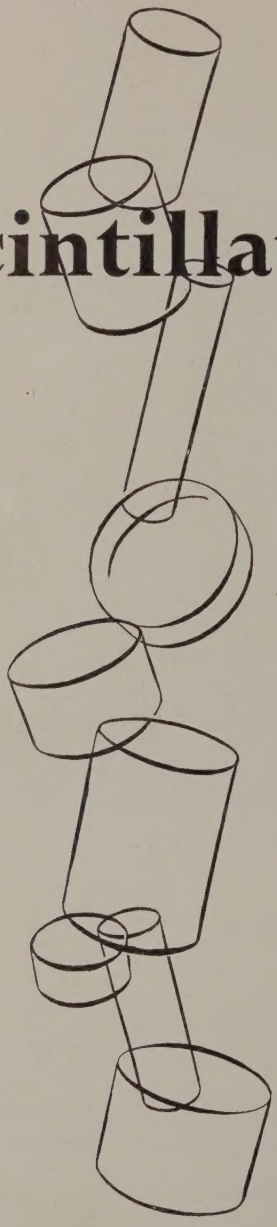

Scintillators in five forms are now available from Nash and Thompson Ltd.

CRYSTALS

Anthracene, Stilbene, Diphenylacetylene, in discs and cylinders.

PLASTICS

N.11 and N.11-X-ray, high sensitivity, high transmission polyvinyl toluene based.

LIQUIDS

Ready made, sealed in glass containers to your specification, or as scintipaks.

SCINTIPAKS

Accurately mixed dry constituents sealed in polythene envelopes, ready for dissolving in a suitable solvent as required.

POWDERS

Scintillation purity chemicals for crystal growing experiments, and the manufacture of special scintillators.

Meet Nash and Thompson on the S.I.M.A. Stand at the 'Atoms for Peace' Exhibition, Geneva, September 1st-14th, 1958.

Write or telephone for full information to

Nash and Thompson LTD

OAKCROFT ROAD · CHESSINGTON · SURREY · ENGLAND
ELMBRIDGE 5252

WHG/NT64

Hamner

POWER SUPPLY SURPASSES EXPECTATIONS

The Ultimate in Stability Proved In Precision X-Ray Spectroscopy Laboratory Test

MODEL N-401 REGULATED HIGH VOLTAGE POWER SUPPLY

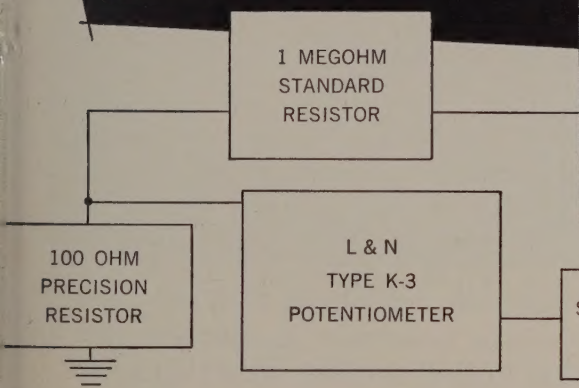

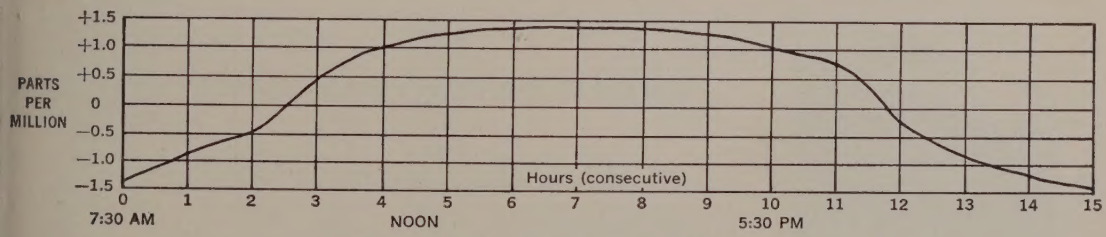

Graph Shows Long Term Stability To Be Better Than ±1.5 Parts Per Million

The Johns Hopkins University Precision X-Ray Laboratory recently tested the stability of a Model N-401 Regulated High Voltage Power Supply *for a period of 15 hours. The voltage was constant within ±1.5 part per million* as shown by the graph. The power supply was in use approximately 2000 hours and tested in an ambient temperature of 24.00° ±0.05° centigrade.

- **The Model N-401 is a new concept in regulated power supply design — it provides up to 5 MA of current and negative or positive DC voltage — continuously variable from 500 to 1800 volts.**
- **Unmatched stability against line change; less than 0.003% per volt — Regulation, 0.0025% per MA @ 1000 volts — Output impedance, 2.5 ohms.**
- **Low noise and ripple; less than 1 MV RMS.**
- **Designed for use with scintillation and proportional counters or for general laboratory use — anywhere the ultimate in stability is required at a reasonable price.**

Hamner Electronics Co., Inc.

P.O. BOX 531, PRINCETON, NEW JERSEY, U.S.A. • Phone: Pennington 7-1320

Export Department: H.E.C.I., 202 East 44th Street, New York, New York, U.S.A.

nner's complete line of nuclear instruments includes: Mercury Switch Pulsers, Scalers, Photomultiplier Preamplifiers, Scintillation Counters, High Voltage ver Supplies, Recording and Manual Spectrometers, Log Count Rate Meters, High Gain Non-Overloading Amplifiers, etc. Complete Catalog Available.

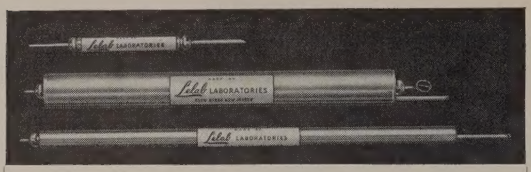

LELAB METAL-WALLED G-M TUBES

for anti-coincidence applications where uniformity counts !

Lelab Counter Tubes are individually constructed, filled, and tested. Each is fabricated almost entirely of metal. All components are confined within the diameter of the tube shell to permit close stacking.

Compare our low prices on these superior tubes!

(Makers of Lelab [Robinson-Selverstone Type] Probe Counters for neurosurgery and where a fine needle-like probe for highly localized measurements is useful.)

Write for complete information

H. W. Leighton Laboratories

York & Sunset Lane-Hatboro, Pa. U.S.A.

MODEL 412 MERCURY RELAY

PRECISION SLIDING PULSER

for Precise Calibration of Single & Multi-Channel Pulse Height Analyzers

Determines Window Widths Using Principle of *Constant Angular Velocity* } **AUTOMATICALLY** **10 × more accurately** **40 × faster than conventional pulsers**

Incorporates Both Manual Control and Precision Motor Drive

Simulates Pulses from Scintillation, Proportional or Geiger Counters

RISE TIME—Less than .003 usec.

DECAY TIME CONSTANT—1, 10, 100, 350, usec.

LINEARITY—0.1% 10 turn potentiometer with 5" dial.

CALIBRATION—Self contained standard cell and null balance circuit for precision adjustment.

MERCURY PULSER, Model 401

Featuring Versatility and Precision

Specifically designed for the Nuclear Physics Laboratory

RISE TIME—Less than .003usec

DECAY TIME CONSTANT—1, 10, 100 usec

Fast rise and exponential decay simulates scintillation, proportional or geiger counter pulses for test and calibration of amplifiers, pulse height analyzers, scalers, etc.

MODEL 412 . . . $ 450.00 — MODEL 401 . . . $ 125.00

RADIATION INSTRUMENT CO.

P. O. BOX 733, SILVER SPRING, MARYLAND, U.S.A.

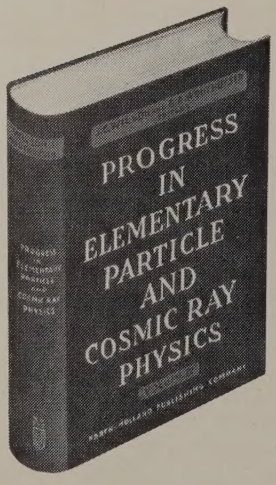

PROGRESS IN ELEMENTARY PARTICLE AND COSMIC RAY PHYSICS VOL. IV

Editors

J. G. WILSON, *Professor of Physics, University of Leeds*

and

S. A. WOUTHUYSEN, *Professor of Physics, University of Amsterdam*

6 × 9″ XII + 482 p. 110 illus. Guilders 45.00 (90 s)

CONTENTS

1. *Some Theoretical Aspects of the Strong Interactions of the New Particles* (B. D'Espagnat and J. Prentki). 2. *The Properties and Production of K-mesons* (W. D. Walker). 3. *The Interaction of μ-Mesons with Matter* (G. N. Fowler and A. W. Wolfendale). 4. *The Primary Cosmic Radiation and its Time Variations* (S. F. Singer). 5. *The Origin of Cosmic Radiation* (V. L. Ginzburg).

Sole Agency for U.S.A.: Interscience Publishers, Inc. — New York

NORTH-HOLLAND PUBLISHING COMPANY - AMSTERDAM

Send your order to your bookseller or directly to us

arco APPLIED RADIATION news

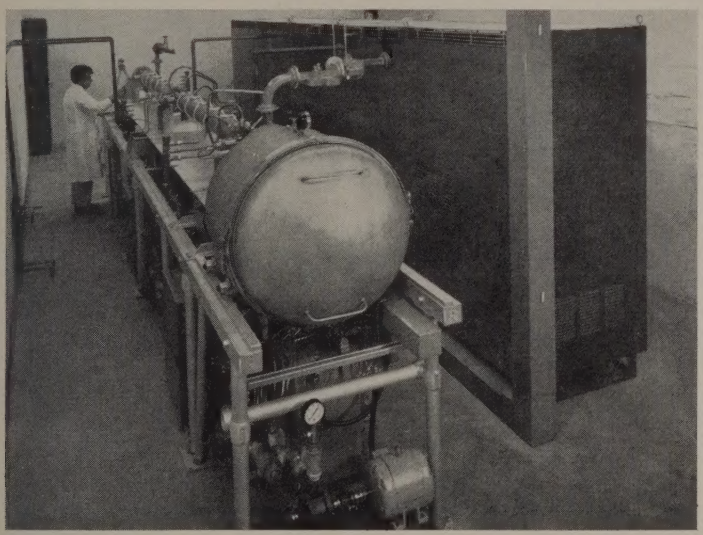

Linear electron accelerator for nuclear research

GA plans studies in power reactor design, neutron and solid state physics, nuclear and radiation chemistry

Intense neutron, x-ray and electron beams from a 2 to 32 Mev ARCO Mark 1-T4 linear electron accelerator will open another area of General Atomic's expanding program of nuclear research when the accelerator is installed this spring. GA physicists will use the (γ,f) and (γ,n) reactions in uranium to produce up to 10^{16} neutrons per second (peak rate during pulse) for research in neutron physics and for studies with sub-critical power reactor cores. Nuclear chemists will study photonuclear processes with precisely controlled bremsstrahlung of the order of 5000 times as intense as has been attainable with betatrons and synchrotrons. The accelerator's pulsed electron and x-ray beam will also be used for fundamental investigations in solid state physics and radiation chemistry.

General Atomic Division of General Dynamics Corporation is the corporate unit responsible for research, development, and production in the nuclear field. Its new John Jay Hopkins Laboratory for Pure and Applied Science in northern San Diego is conducting research in reactors, nuclear and solid state physics, chemistry, and controlled thermonuclear reactions. A source of radiation was needed which would meet the diverse demands of the Laboratory.

General Atomic chose an ARCO Mark 1-T4 linear electron accelerator. Initially operable at energies continuously variable to 32.5 Mev with electron beam power to 4 kilowatts, this accelerator is designed for subsequent 2-fold expansion in both power and energy.

For Neutron Physics—10^{16} Neutrons/Second during Pulse

High energy photofission reactions in uranium are among the most efficient neutron-producing reactions. High energy linear accelerators are intense x-ray generators and hence are useful sources of fast neutrons. General Atomic's ARCO Mark 1-T4 linear accelerator will produce neutrons at a rate of 10^{16} per second during pulses of ½ to 5 microseconds duration; it will generate average yields of 10^{13} per second.

Photofission reactions yield a characteristic fission neutron energy spectrum; monoenergetic neutrons will be obtained by time-of-flight techniques. General Atomic plans to measure neutron cross-sections as well as detailed parameters characteristic of sub-critical reactor systems such as neutron spectra, diffusion constants, and neutron lifetimes.

For Nuclear Chemistry—Gamma Yields 5000 Times Greater than from a Betatron

Both the efficiency of bremsstrahlung production and the average energy of the bremsstrahlung spectrum increase with the energy of the primary electron beam. High beam power allows magnetic energy analysis to within 0.1-0.01 percent for precise bremsstrahlung generation. General Atomic's nuclear chemists plan fundamental investigations of (γ,n), (γ,p), (γ,α), (γ,d) and (γ,f) reactions as well as processes induced by neutrons. Photonuclear reactions will also be utilized for activation analysis and the production of nuclides which cannot be produced in a reactor.

For Solid State Physics—½ to 5 Microsecond Electron Pulses

General Atomic will utilize the accelerator's pulsed electron and x-ray beams to study both transient and gross radiation damage in semiconductors and structural materials. Electrons with energies of a few million volts will produce isolated interstitials and vacancies. With full machine energy, atoms knocked out of the lattice by a direct bombarding electron hit will have sufficient momentum to displace about ten other atoms. Thus, more complicated forms of radiation damage can be studied.

For Radiation Chemistry—High Intensity, Deep Penetration

G.A.'s pulsed electron beam will permit study of free radicals and other short-lived chemical species induced by ionizing radiation, for a sufficient number can be created in a single pulse or short series of pulses to allow direct identification. High beam energies make possible electron and x-ray irradiation of pressurized systems and thick specimens; high power operation makes study of low-yield reactions practical.

General Atomic plans to make time on its ARCO accelerator available to selected research and development organizations and users of radiation. It also will conduct contract research studies of interest to the Laboratory.

Write for Information

Applied Radiation Corporation specializes in the development and manufacture of electron and positive ion accelerators. Modular construction allows ARCO to tailor accelerators to the needs of individual organizations, whether modest or demanding.

Write for technical data on ARCO accelerators and reports, AM-105, *Isotope Production with a Linear Accelerator* and AM-100, *Production of Gamma Radiation with a Linear Electron Accelerator*. Department I-6.

APPLIED RADIATION CORPORATION

High energy radiation for research and processing

Walnut Creek, California, YEllowstone 5-2250, Cable "ARCO"

4911

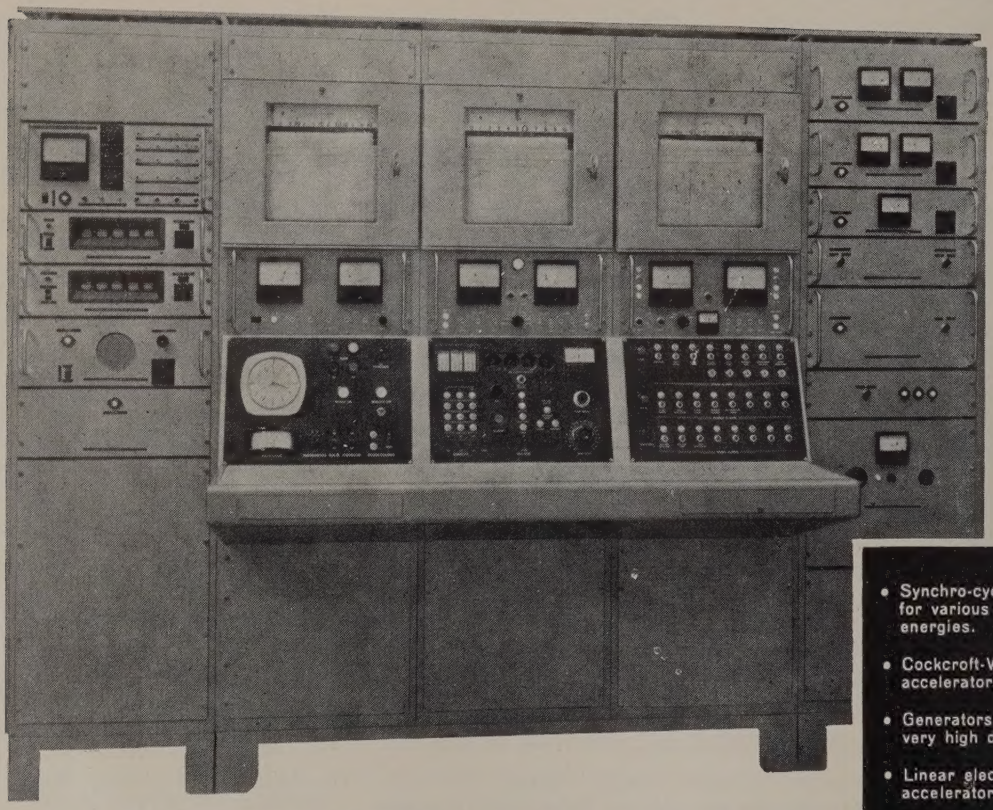

PHILIPS *equipment for*
Nuclear Physics and Atomic Energy

Shown here is a complete instrument panel for a "swimming pool" nuclear reactor. The panel contains full flux measuring facilities covering the entire range of operation. All controls and indicators for the operation of control rods, safety system, multi-point area monitoring and auxiliary units are included. The reactor will be installed at Delft Technical University. Similar systems designed to exactly fill your needs can be supplied.

- Synchro-cyclotrons for various final energies.
- Cockcroft-Walton accelerators.
- Generators for very high d.c. voltages.
- Linear electron accelerators.
- Reactor control instrumentation.
- Radiation measuring and detection equipment.
- Civil defence instruments.
- Area monitoring instrumentation.
- Geiger counter tubes.
- Photomultipliers.
- Radio-active isotopes.
- Air liquefiers.

PHILIPS

PHILIPS
Nuclear Equipment

For further information please apply to one of the following addresses:

N.V. PHILIPS' GLOEILAMPENFABRIEKEN, Scientific Equipment Department, Eindhoven-Holland
RESEARCH & CONTROL INSTRUMENTS LTD., Instrument House, 207/215, King's Cross Road, London WC 1
PHILIPS ELECTRONICS INC., Instruments Division, 750, South Fulton Avenue, Mount Vernon N.Y. U.S.A.

ZDO

THE *Ultimate* IN LOW-LEVEL COUNTING

RIDL Model 41-1
LOW LEVEL
Counting Systems

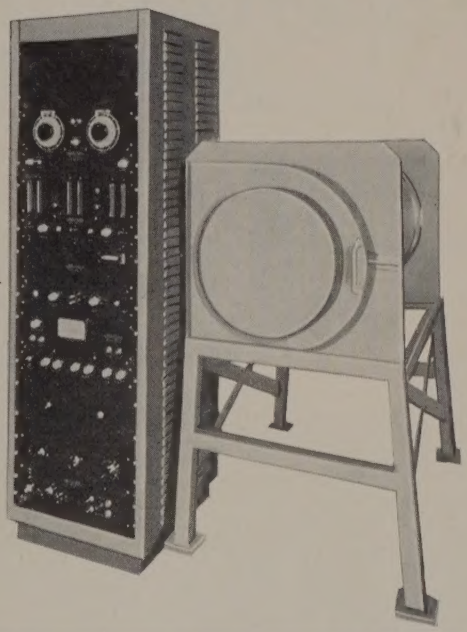

RESEARCH STUDIES

- Self-diffusion
- Reaction mechanisms
- Surface phenomena
- Kinetics
- Isotope effects

INDUSTRIAL DEVELOPMENT and CONTROL

- Flow rates
- Volumetric measurements
- Flow patterns
- Mixing rates
- Chemical arrangements

RIDL is proud to present the Model 41-1 Low-Level Counting System. Regardless of whether your work involves *solid* or *gas* samples, this system is fitted to your every need.

THE "BASIC PACKAGE" FOR THE MODEL 41-1 CONSISTS OF:

Model 60-4 Massive Shield
Model 9-1 Anti-coincidence Ring
Model 32-1 Anti-coincidence Analyzer
Model 49-2 Multi-channel Scaler
Model 40-1 Triple 500-2500 volt High Voltage Supply
Model 2-2 Dual Soft Beta Flow Counter (for solid samples) or
Model 8-1 Gas Sample Counter (for gas samples)

THIS "BASIC PACKAGE" MAY BE USED FOR GEIGER-MULLER COUNTING AS IT STANDS. BY ADDING THE

Model 214 "Ultra Stable" 500-5000 volt High Voltage Supply
Model 33-1 Pulse Height Analyzer and
Model 60-5 Electrostatic Shield,

the system may be used for proportional counting work.

REMEMBER, whatever your counting problem may be, RIDL has the solution. Our staff is always available to answer your inquiries. Write today for complete information.

RIDL

Radiation Instrument Development Laboratory, Inc.

5737 South Halsted Street, Chicago 21, Illinois • TRiangle 3-2345

FOR
STEAM AND NUCLEAR
POWER STATIONS

BROWN
BOVERI

One of the four 150-MW steam turbines for a large power station

Brown, Boveri & Co., Ltd., Baden (Switzerland)

Representatives in most countries

NUCLEAR INSTRUMENTS 3 (1958) 57–68; NORTH-HOLLAND PUBLISHING CO. – AMSTERDAM

A NEW METHOD IN GAMMA-RAY SPECTROSCOPY: A TWO CRYSTAL SCINTILLATION SPECTROMETER WITH IMPROVED RESOLUTION

A. M. HOOGENBOOM

Fysisch Laboratorium der Rijksuniversiteit te Utrecht

Received 11 March 1958

A new method has been developed to measure the spectra of gamma radiation emitted in cascade disintegrations. Use is made of a two-crystal scintillation spectrometer and a gated multi-channel analysing device. The pulses produced by summing the outputs of the two crystal-photomultiplier combinations are selected by a single-channel differential discriminator. The output of this differential discriminator gates the multi-channel analyser whenever the sum pulse corresponds to the release in the crystals of the full energy available in the cascade. The spectrum displayed is that of either of the two detectors.

The most important features of the technique are:

(a) only "full-energy" peaks are detected;

(b) improved resolution is obtained especially at higher gamma-ray energies;

(c) one γ–γ or p–γ–γ angular correlation experiment determines the angular correlation of the gamma rays of all double cascades deexciting a given level.

Details of operation and typical spectra are presented. It is suggested that the technique be called the "sum-coincidence" method.

1. Introduction

In a normal single-crystal gamma-ray scintillation spectrometer the pulse-height distribution produced by monoenergetic gamma radiation is rather complicated because of the different processes which arise in the conversion of the gamma-ray energy into an electric pulse. Therefore, since the beginning of gamma-ray scintillation spectroscopy there has been a tendency to simplify the observed spectra by using more than one crystal. In the two-crystal coincidence spectrometer developed by Hofstadter and McIntyre[1]) Compton-scattering processes are selected by a coincidence arrangement between the incident radiation and the radiation scattered at a certain angle. In the two-crystal anticoincidence spectrometer introduced by Albert[2]) only those pulses from one crystal are accepted which are not in coincidence with a pulse in a large crystal surrounding the first one. In the three-crystal triple-coincidence spectrometer constructed by Johansson[3]), and independently by Maienschein and Bair[4]), only those pair processes are accepted which are in coincidence with the detection of both annihilation quanta in lateral crystals. All these solutions suffer from the disadvantage that if the resolution is good the efficiency becomes very small and vice versa. This is especially serious if the gamma-ray spectrum is complicated and contains a number of coincident lines. It is almost impossible to use one of these spectrometers to measure γ–γ coincidence spectra or γ–γ angular correlations.

In the present paper a new type of scintillation spectrometer is described especially suited to measure γ–γ coincidence spectra and γ–γ angular correlations. The new spectrometer combines good resolution with a relatively high efficiency for both low and medium gamma-ray energies. The main features are:

(a) The pulse distribution shows only one peak, the "full energy" peak, for one specific gamma transition. There is no contribution to the spectrum from processes in which only part

[1]) R. Hofstadter and J. A. McIntyre, Phys. Rev. **78** (1950) 619.

[2]) R. D. Albert, Rev. Sci. Instr. **24** (1953) 1096.

[3]) S. A. E. Johansson, Nature **166** (1950) 794.

[4]) F. C. Maienschein and J. K. Bair, Phys. Rev. **82** (1951) 317 (A).

of the available gamma-ray energy is absorbed.

(b) The absolute half-widths of the peaks due to coincident gamma rays are, to first approximation, equal.

(c) The detection efficiences of coincident gamma rays are equal.

2. Principle of operation

In many cases (e.g. in all (p,γ) reactions) a complicated nuclear decay scheme can be subdivided into a number of cascades starting all at one single level and ending at the ground state of a nucleus. The principle of operation is based on the fact that the total energy involved in different cascades is the same. For simplicity the discussion will be limited to cascades of two gamma rays only.

The two gamma rays of one of these cascades can be detected in coincidence with two scintillation counters. If both scintillation counters have the same energy calibration the sum of their output pulses is proportional to the sum of the energies absorbed in the two crystals. Therefore, if both gamma quanta of a cascade are fully absorbed, this sum pulse as obtained from a linear adding network corresponds to the release of the total energy involved in the cascade. Pulses from one of the scintillation counters which are in coincidence with these special sum pulses all belong to processes of full-energy absorption of one or both gamma quanta in this crystal. Thus this coincidence spectrum shows only the full-energy peaks of the gamma rays of the cascade, accompanied by a peak due to the absorption of both gamma quanta in one crystal. In practice this "sum-coincidence" spectrum is obtained by gating a multi-channel pulse-height analyser. The gate

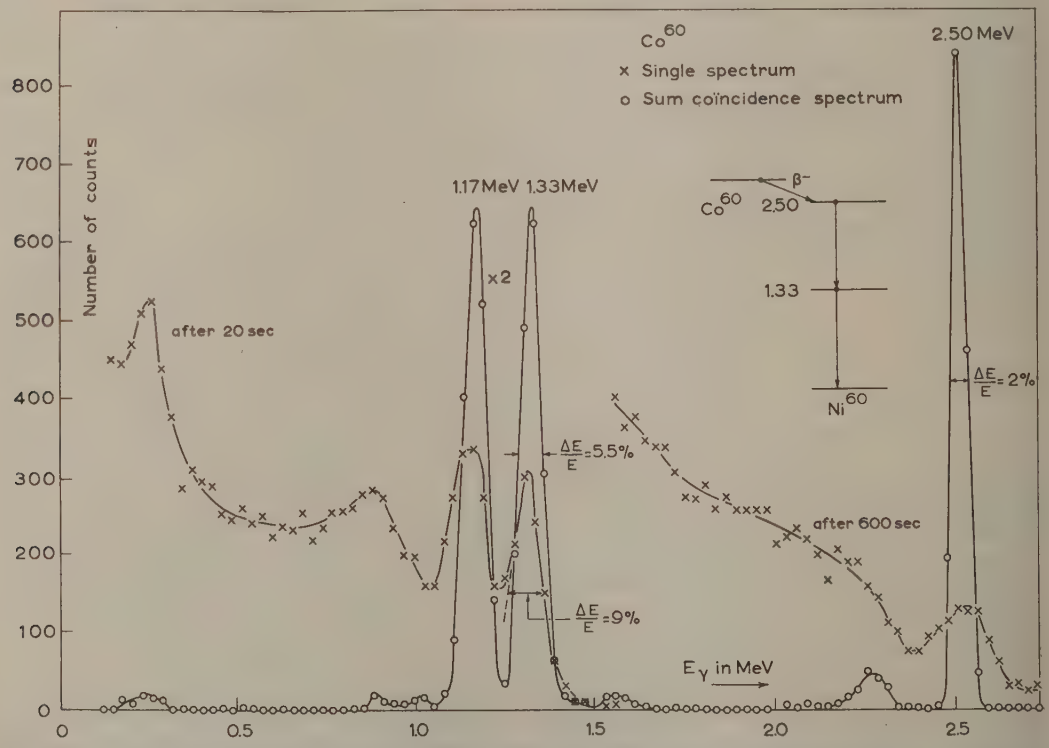

Fig. 1. Single and sum-coincidence spectrum of Co^{60} using 2″ crystals. The single spectrum indicated by crosses is on an arbitrary scale. The sum-channel setting is at 2.50 MeV. In this measurements no lead shielding was applied between crystals. The small peaks at 0.25, 1.0, 1.6, and 2.30 MeV are due to back-scattering.

pulse is selected from the spectrum of sum pulses by a differential discriminator.

The sum-coincidence method will be elucidated by a simple example of a single cascade. The nuclide Co^{60} decays by β^- emission to the 2.50 MeV level in Ni^{60}. The 2.50 MeV level is deexcited by a cascade of 1.17 and 1.33 MeV gamma rays to the ground state. No cross-over is observed. In fig. 1 the pulse spectrum is shown obtained by applying the sum-coincidence method. In this case the channel of the differential discriminator of 2% width was set at 2.50 MeV. A further explanation of fig. 1 is given in section 5.

In the next section a description will be given of the necessary apparatus.

3. Apparatus

In this section a description is given of a sum-coincidence scintillation spectrometer. A schematic diagram is shown in fig. 2. The crystals CR1 and CR2 are shielded from each other by lead cones. About 7 cm of lead is put around the crystals to reduce background. The pulses from the cathode followers CF1a and CF2a are fed to the amplifiers 1 and 2, and to the linear adding network. The linear adding network comprises the cathode followers CF1b and CF2b, the resistors R_1 and R_2, and a potentiometer RV1. The values of R_1 and R_2 are about 10 times the output impedance of the cathode followers. As mentioned in the preceding section the energy calibration of both detectors has to be the same. This is done by adjusting the high voltage of one of the multiplier tubes. The potentiometer RV1 serves as a fine adjustment. After amplification the sum pulses are fed into a differential discriminator to select the sum channel. The multi-channel analyser is gated with these selected pulses.

In fig. 2 no special coincidence arrangement is included. Actually the adding network acts as a slow coincidence circuit with a time resolution of about 3 μsec. However, at high counting rates a coincidence circuit between CF1a and CF2a will be necessary. The extension to a system for high counting rates comprises also a second coincidence circuit between the output pulse from "D.D. sum" and the output pulse from the first coincidence circuit.

The output of amplifier 2 can be used as a monitor in angular correlation experiments.

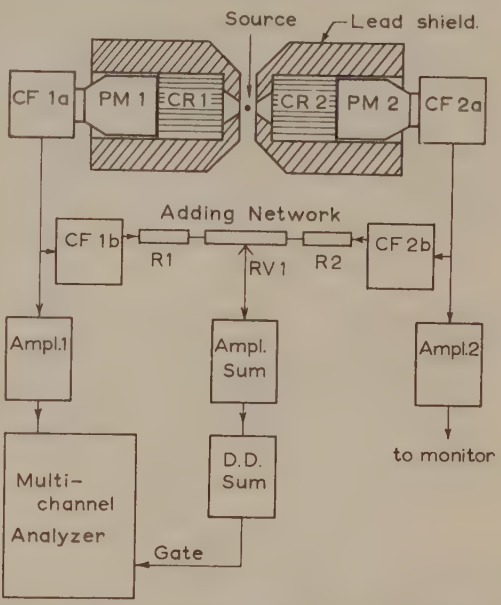

Fig. 2. Experimental arrangement of the sum-coincidence method. CR1 and CR2 are the two crystals, PM1 and PM2 indicate photomultipliers. The four cathode followers are labelled CF1a and b and CF2a and b. The pulses summed in the adding network are amplified by the amplifier "Sum". The sum-channel is chosen with the differential discriminator "D.D.sum".

The bias and channel width of the differential discriminator "D.D. sum" influence the shape of individual gamma-ray peaks. This is discussed in the next section.

4. Resolution and Efficiency

It is assumed that the gamma rays γ_1 and γ_2 with energies E_{01} and E_{02} respectively, are in cascade, and that the pulse distributions $f_1(E_1 - E_{01})$ and $f_2(E_2 - E_{02})$ corresponding to the "full-energy" peaks are gaussian with half-widths (full width at half maximum) of Γ_1 and Γ_2, respectively. For mathematical simplicity the sum channel will also be assumed to have a gaussian transmission $f_s(E_1 + E_2 - E)_{0s}$

with a half-width Γ_s. The bias of the sum channel is set such that $E_{0s} = E_{01} + E_{02}$. The functions f_1 and f_2 are normalized such that the total numbers of pulses in the corresponding full-energy peaks equal ε_1 and ε_2, where ε_1 and ε_2 are the full-energy efficiencies (including solid angle) for detection of γ_1 and γ_2, respectively. The area under f_s amounts to Γ_s.

By multiplying f_1, f_2, and f_s, and by integrating over E_2 one obtains the pulse distribution in the sum-coincidence spectrum of the peak corresponding to γ_1. The half-width Γ_{s1} of this peak is given by:

$$\Gamma_{s1} = \Gamma_1 \sqrt{\Gamma_2^2 + \Gamma_s^2} / \sqrt{\Gamma_1^2 + \Gamma_2^2 + \Gamma_s^2} . \quad (1)$$

This proves that a peak in the sum-coincidence spectrum is always narrower than the corresponding peak in the single spectrum.

The best energy resolution is obtained, of course, if the sum channel is made vanishingly narrow ($\Gamma_s \ll \Gamma_1$ and $\Gamma_s \ll \Gamma_2$). Then:

$$\Gamma_{s1} = \Gamma_{s2} = \Gamma_1\Gamma_2 / \sqrt{\Gamma_1^2 + \Gamma_2^2} . \quad (2)$$

In this case the peaks in the sum-coincidence spectrum corresponding to γ_1 and γ_2 have the same width. Both peaks are narrower than the narrowest of the two peaks in the single spectrum. This especially serves to improve the resolution in the high-energy region. If a 1 MeV and a 6 MeV gamma ray are in cascade, both having full-energy peaks in the single spectrum of 6% width, the width of the high-energy gamma ray in the sum-coincidence spectrum will only be 1%. If γ_1 and γ_2 have about equal energies and widths (which applies to the Co^{60} case) the improvement in resolution will still be a factor $\sqrt{2}$. The improvement obtained is especially welcome when the single-spectrum resolution is low, which is the case e.g. for large crystals. In practice there is no advantage in making Γ_s smaller than the smallest of Γ_1 and Γ_2.

If the bias of the sum channel is not set correctly ($E_{0s} \neq E_{01} + E_{02}$) the peaks in the sum spectrum corresponding to γ_1 and γ_2 are still gaussian but they are shifted. This shift is not a constant percentage of the setting error $E_{0s} - (E_{01} + E_{02})$ and thus the spectrum is distorted. Careful bias setting is thus necessary.

The efficiency ε_{s1} for detection of γ_1 with the sum-coincidence method is easily found by integrating the corresponding pulse distribution over E_1. This yields:

$$\varepsilon_{s1} = 2\sqrt{\ln 2/\pi}\, \varepsilon_1\varepsilon_2\Gamma_s / \sqrt{\Gamma_1^2 + \Gamma_2^2 + \Gamma_s^2} . \quad (3)$$

As this is symmetric in the indices 1 and 2 the areas of the peaks corresponding to γ_1 and γ_2 have to be equal. Any deviation from equality, outside statistics, can only be caused by a wrong setting of the potentiometer RV1 in the adding circuit. The fact that (3) contains the product of the full-energy efficiencies means that the detection efficiency in the sum-coincidence spectrum does not depend strongly on gamma-ray energy.

In every sum-coincidence spectrum a "sum peak" appears corresponding to the energy E_{0s} chosen by the sum channel. The intensity of this peak contains contributions from:

(a) the full-energy peak of the cross-over transition;

(b) events in which the two gamma rays of one cascade both dissipate their total energy in crystal 1;

(c) background.

If the experimental arrangement is symmetric (crystals of equal size at equal distance from the source) contribution (b) exactly amounts to one half the sum of the intensities of all other peaks in the sum-coincidence spectrum. Contribution (c) can easily be measured. In a symmetric arrangement the sum peak can thus be used as a sensitive measure to obtain the intensity of the cross-over transition relative to that of the cascades. With the analysis given above it is not difficult to deduce an expression relating this intensity ratio to the areas of the relevant peaks.

5. Measurements of spectra

To demonstrate the possibilities of the sum-coincidence method a number of gamma-ray spectra were measured. In the following discussion γ_1, E_{γ_1}, and Γ_1 will be used for the lower-energy gamma ray of a cascade.

5.1. SPECTRA MEASURED WITH TWO 2″ CRYSTALS

The two 2″ crystals used to measure the following spectra were both of medium quality giving about 10% half-width at $E_\gamma = 1$ MeV and about 7% at 8 MeV.

5.1.1. Co^{60}

The spectrum already mentioned in section 2 consists only of one cascade. As shown in fig. 1 this cascade gives rise to two well resolved peaks at 1.17 and 1.33 MeV. Because the energies of γ_1 and γ_2 are nearly the same while the sum channel is relatively narrow (2%) one has

$$\Gamma_{s_1} \approx \Gamma_{s_2} \approx \Gamma_1 / \sqrt{2} \ .$$

Fig. 1 also shows the single spectrum giving 9% half-width for the 1.33 MeV peak. Substitution of this value predicts a 6% half-width for this peak in the sum spectrum. This is in good agreement with the measured value of 5.5%.

somewhat smaller than that to crystal 2. Therefore the number of counts in the sum peak is higher than the number of counts in the 1.17 and 1.33 MeV peaks. The latter numbers are equal as they should be.

The small peaks at about 0.25, 1.0, 1.6, and 2.3 MeV originate from back-scattering of one detector to the other. In fig. 1 these peaks are relatively high because the lead shielding between the detectors was removed in order to show this effect clearly. Back-scattering can be avoided easily by only one centimeter of lead between the crystals in the way shown in fig. 2.

5.1.2. Na^{22}

The decay of Na^{22} by β^+ emission gives rise to two 0.51 MeV annihilation quanta emitted from the source in opposite directions and coincident with the gamma ray of 1.28 MeV from the first level in Ne^{22} to the ground state.

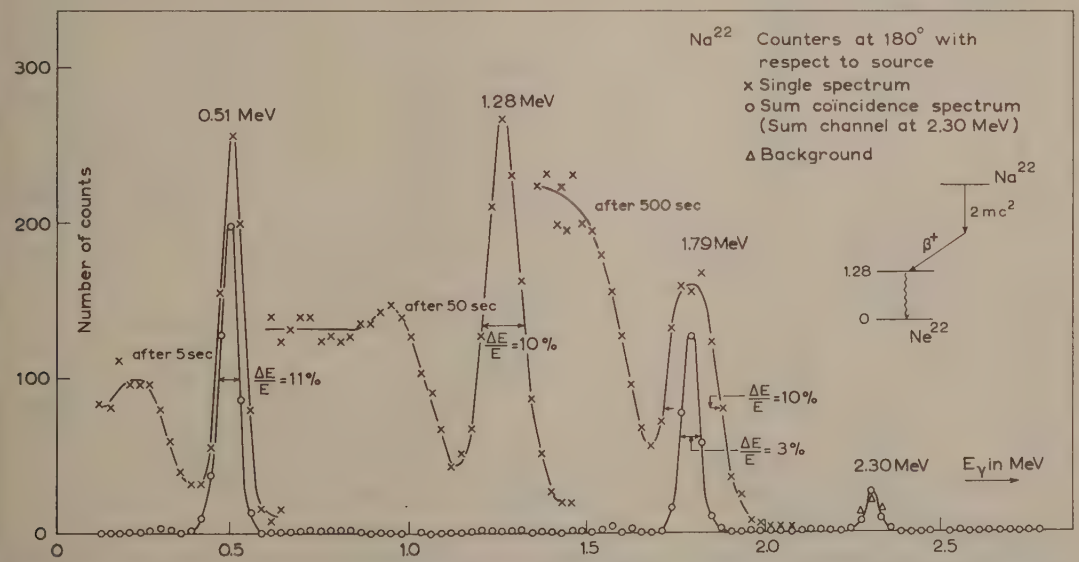

Fig. 3. Single and sum-coincidence spectrum of Na^{22} using 2″ crystals. The counters are placed at 180° with respect to the source. The sum channel is set at 2.30 MeV. The single spectrum is given on an arbitrary scale. Note the background measured near 2.30 MeV.

Because Co^{60} is known to emit no 2.50 MeV gamma ray the sum peak in this case is only due to events in which both gamma rays are absorbed in one crystal. In this measurement the distance from the source to crystal 1 was

Therefore, depending on the position of the counters and the setting of the sum channel, two different spectra can be obtained:

(a) Putting the counters at 180° with respect to the source gives the possibility of absorption

of one 0.51 MeV quantum in one crystal in coincidence with the absorption of the other 0.51 MeV quantum plus the 1.28 MeV quantum in the second crystal. In this case the sum of the energies involved amounts to 2.30 MeV. Fig. 3 represents a measurement with the sum channel set at 2.30 MeV. It clearly shows the impossibility of absorption of the two annihilation quanta

$\Gamma_s \ll \Gamma_2$, and also $\Gamma_1 \ll \Gamma_2$. Using eq. (2) one finds for this case $\Gamma_{s2} \approx \Gamma_1$. Because also $\Gamma_{s1} \approx \Gamma_1$ the absolute half-width of the peaks at 0.51 MeV and 1.79 MeV should be the same. The measurement gives $\Gamma_{s1} = 55$ keV and $\Gamma_{s2} = 54$ keV. This means a relative half-width for γ_2 of only 3% compared with a 10% half-width in the single spectrum in fig. 3.

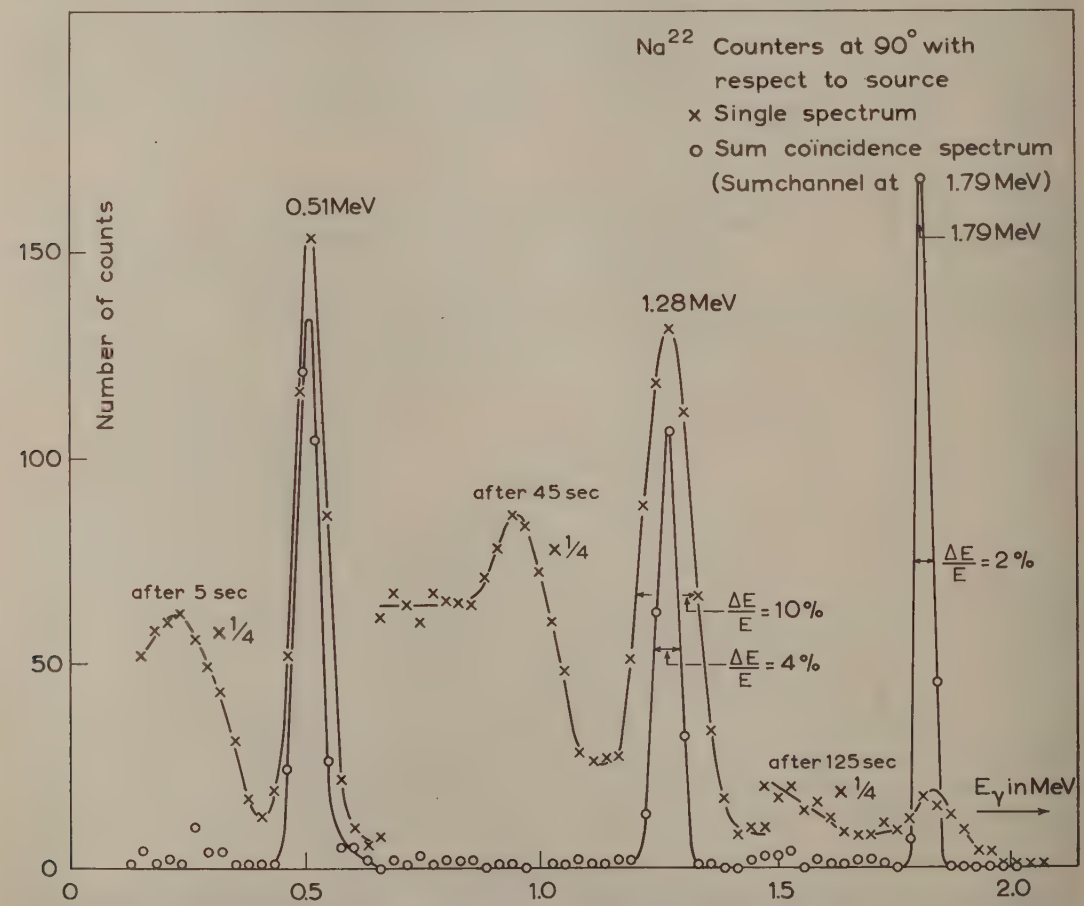

Fig. 4. Single and sum-coincidence spectrum of Na^{22} using 2″ crystals. The counters are placed at 90° with respect to the source. The sum channel is set at 1.79 MeV. The single spectrum is given on an arbitrary scale.

in one crystal by the complete absence of the 1.28 MeV line. For the same reason the height of the sum peak reduces to zero after subtraction of background. The width of the sum peak as determined by the channel width of the differential discriminator amounts to 1.5%. Therefore

Because in this measurement the source was nearer to crystal 2 than to crystal 1 the intensity of the 0.51 MeV peak is somewhat higher than the intensity of the 1.79 MeV peak.

(b) Putting the counters at 90° with respect to the source limits the sum of the energies of

the gamma rays absorbed in coincidence to 1.79 MeV. Therefore, setting the sum channel at 1.79 MeV one gets the spectrum of fig. 4 showing the 0.51 MeV and the 1.28 MeV gamma ray. Here the sum peak arises from the absorption of both gamma rays in one crystal. Substituting the values 125 keV for Γ_2, 50 keV for Γ_1, and 36 keV for Γ_s, as taken from the single spectrum and from the sum peak in fig. 4, into eq. (1), gives $\Gamma_{s2} = 58$ keV. The measured value amounts to 53 keV or about 4%.

5.2. SPECTRA MEASURED WITH TWO 4″ CRYSTALS

In this case the counters consisted of two 4″ Harshaw crystals and two 5″ Dumont 6394 photomultiplier tubes. These counters gave a relative half-width in the single spectrum of about 15% at 0.51 MeV and about 10% at 8 MeV.

spectrum of Co^{60} (taken to be equal to that of the 1.28 MeV line in Na^{22}) amounts to $\Gamma_1 \approx \Gamma_2 \approx 145$ keV. From fig. 5 one finds $\Gamma_s = 100$ keV. Using eq. (1) one gets $\Gamma_{s1} \approx \Gamma_{s2} \approx 110$ keV or about 8.5%. The measured value is 9%.

In this experiment the shielding between the crystals was rather good. Comparison of fig. 1 with fig. 5 indeed shows the suppression of the scattering peaks in the latter.

5.2.2. $Mg^{24}(p,\gamma)Al^{25}$ resonance at $E_p = 222$ keV

The decay scheme of the resonance at $E_p = 222$ keV in the reaction $Mg^{24}(p,\gamma)Al^{25}$ is shown in fig. 6. The relative intensities indicated are taken from the review article by Endt and Braams[5]). The spectrum comprises the two cascades 2.06, 0.45 MeV and 1.56, 0.95 MeV. The relative half-width of 5% found for the

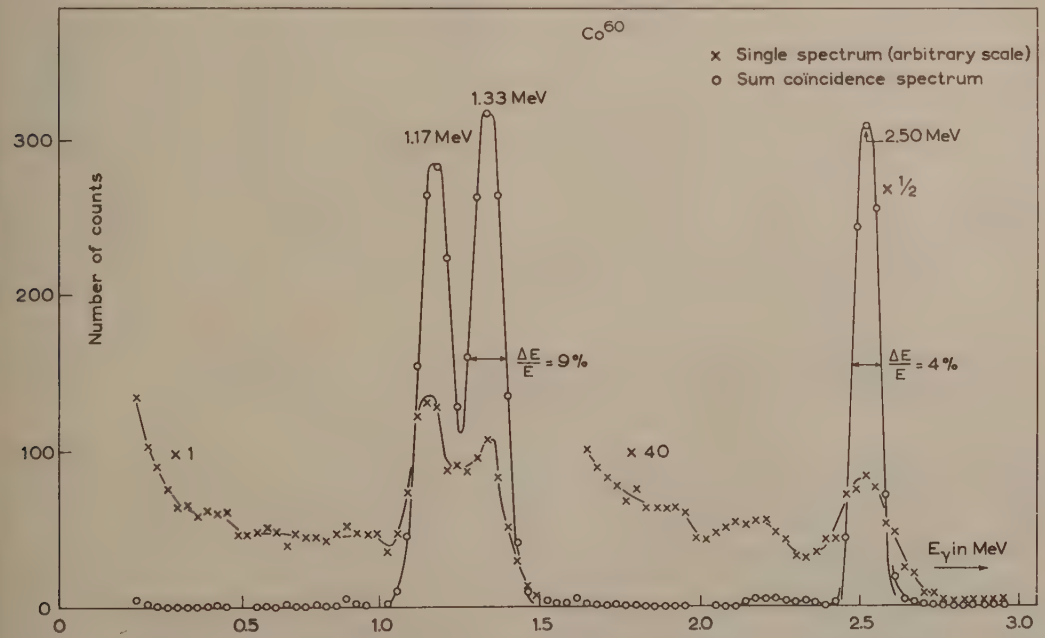

Fig. 5. Sum-coincidence and single spectrum of Co^{60} taken with 4″ crystals. The sum channel is placed at 2.50 MeV.

5.2.1. Co^{60}

The peaks in the spectrum of fig. 5 are somewhat broader than the peaks in the Co^{60} spectrum of fig. 1 because of the lower quality of the large crystals. The half-width in the single 2.06 MeV line is in agreement with the calculated value from eq. (1) assuming a 10% relative half-width for the single spectrum and using the

[5]) P. M. Endt and C. M. Braams, Revs. Mod. Phys. 29 (1957) 683.

measured value of 100 keV for Γ_s. The widths of the lines corresponding to the 0.95 and 1.56 MeV gamma rays are also reduced. Because in this experiment the lead shielding between the ground-state transition of about 6%. The spectrum of the 5.27, 0.69 MeV cascade represented in fig. 7 clearly shows the good resolution for two high-energy gamma rays having an

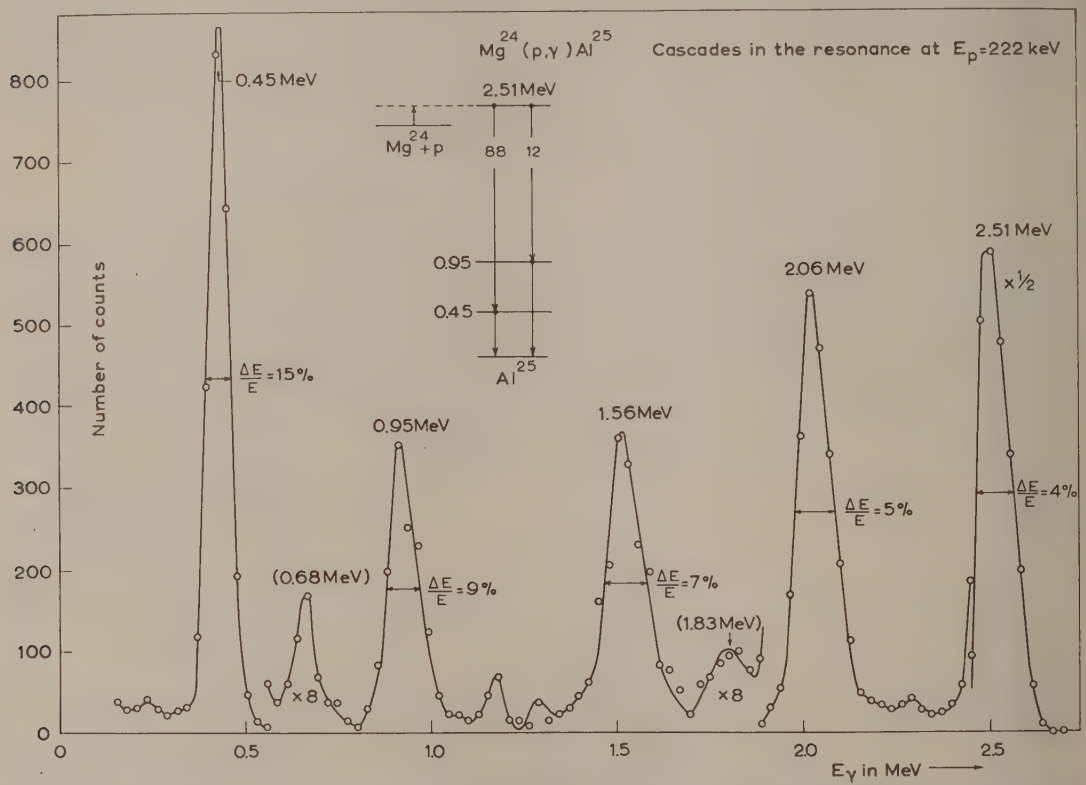

Fig. 6. Sum-coincidence measurement with 4″ crystals showing cascades of 1.56, 0.95 MeV and 2.06, 0.45 MeV in the reaction $Mg^{24}(p,\gamma)Al^{25}$ at $E_p = 222$ keV. The peaks at 0.68 and 1.83 MeV are explained in the text. The sum channel is put at 2.51 MeV.

crystals was partly removed the strong cascade 2.06, 0.45 MeV is accompanied by scattering peaks. The most evident scattering peak is observed at 0.68 MeV, whereas its complement is present as a small shoulder near 1.83 MeV. The low peaks in the 1.1 and 1.35 MeV region are not due to scattering because they appear with equal intensity in measurements with good lead shielding. They are unexplained at the present time.

5.2.3. $Si^{29}(p,\gamma)P^{30}$ resonance at $E_p = 414$ keV

This resonance decays primarily by a cascade of 5.27 and 0.69 MeV gamma rays. There is a energy difference about equal to their single-spectrum half-width. The dotted line shows the single spectrum measured with the same 4″ crystal. Even with the rather broad sum channel of 4%, Γ_{s2} is about 0.5 Γ_2.

5.2.4. $Si^{30}(p,\gamma)P^{31}$ resonance at $E_p = 622$ keV

This resonance shows a very strong ground-state transition as can be seen clearly from the single spectrum given in fig. 8. The low-energy part (below 3 MeV) of this spectrum suggests the existence of two cascades by the appearance of the rather clear 1.27 MeV peak and the low peaks at 2.4 and 2.9 MeV. However, the

high-energy complements of these gamma rays are not resolved in the single spectrum. The sum-coincidence spectrum clearly shows 2.88, 5.01 MeV and 6.62, 1.27 MeV cascades. The intensities of these cascades relative to the ground-state transition amount to about 3% for each. The large intensity of the ground-state transition is The complement of this peak appears as a small shoulder near 7.4 MeV.

At this strong resonance a background is visible resulting from random coincidences. A reduction by a factor of about 100 would be possible by the use of the fast-slow coincidence technique as indicated in section 3.

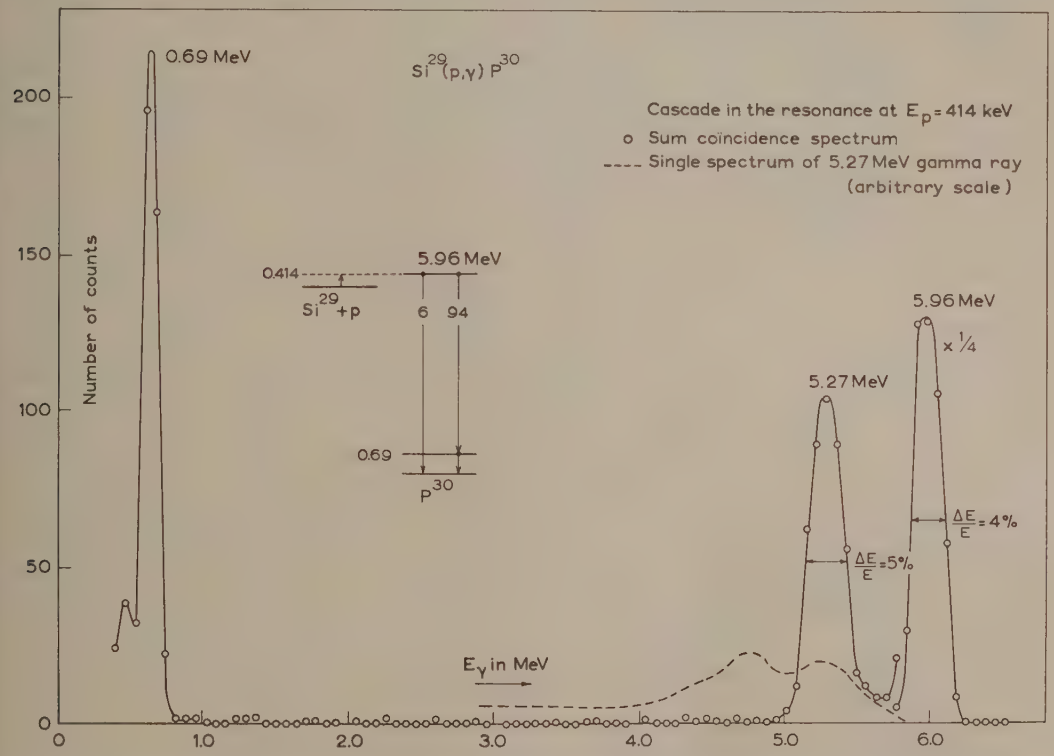

Fig. 7. Sum-coincidence measurement with 4″ crystals showing a cascade of 5.27, 0.69 MeV in the reaction $Si^{29}(p,\gamma)P^{30}$ at $E_p = 414$ keV. The sum channel is set at 5.96 MeV. The dotted line represents the single spectrum.

apparent from the reduction factor of 1080 used in drawing the 7.89 MeV sum peak in fig. 8.

The decay scheme shown in fig. 8 was derived from the observed cascades using the known level scheme[5]) of P^{31}. Because it is known that there is no level at 2.88 MeV, it is concluded that the 2.88, 5.01 MeV cascade decays through a level at 5.01 MeV.

The peak at 0.51 MeV arises from pair formation by 7.89 MeV quanta in crystal 2 and detection of one of the annihilation quanta in crystal 1.

5.2.5. $Si^{30}(p,\gamma)P^{31}$ resonance at $E_p = 675$ keV

The resonance at $E_p = 675$ keV in the reaction $Si^{30}(p,\gamma)P^{31}$ presents a rather complicated decay scheme. The sum-coincidence spectrum showing the cascades in this decay is given in fig. 9. There are three strong cascades namely the 6.67, 1.27 MeV, the 4.81, 3.13 MeV, and the 4.43, 3.51 MeV cascade. Three known levels[5]) through which these three cascades can proceed are the levels at 1.27, 3.13, and 3.51 MeV. The relative intensities are given in the decay scheme

inserted in fig. 9. In this decay scheme three weak cascades are indicated as derived from this experiment. The corresponding relative intensities have not been corrected for possible strong triple cascades with two gamma rays of the three absorbed in one crystal. Therefore, triple coincidence measurements are necessary to confirm the results given.

relative intensities as derived from the sum-coincidence spectra have not been corrected for triple angular correlation effects. In the case of the 622 keV resonance no such effect could occur because the spin of the resonance level is $\frac{1}{2}$[5]). However, the spin of the 675 keV resonance is known to be $\frac{3}{2}$. For this resonance a correction would have been necessary.

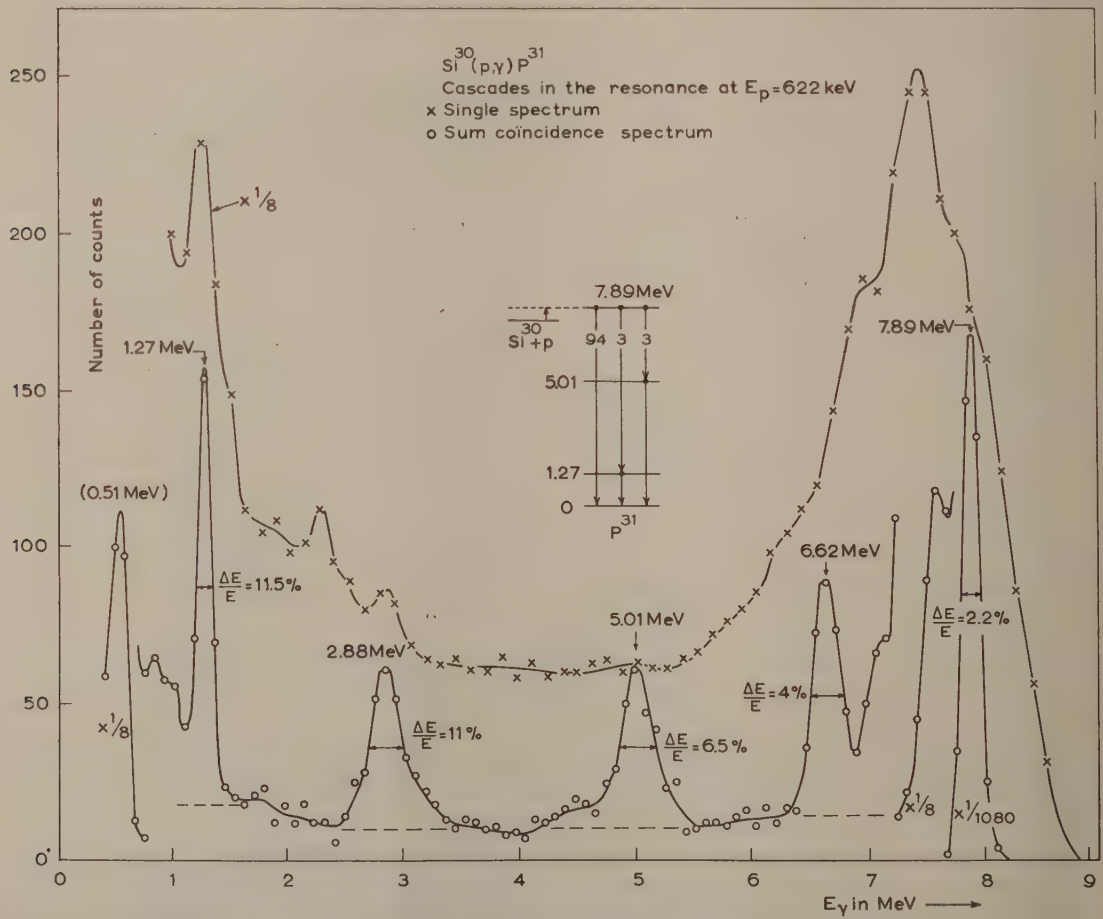

Fig. 8. Sum-coincidence measurement with 4″ crystals showing the cascades 6.62, 1.27 MeV and 2.88, 5.01 MeV in the reaction $Si^{30}(p,\gamma)P^{31}$ at $E_p = 622$ keV. The sum channel is set at 7.89 MeV. Comparison with the single spectrum shows the gain in resolution obtained with the sum-coincidence method. Note the strong ground-state transition (the sum peak has a reduction factor of 1080).

6. Angular correlation measurements

In the $Si^{30}(p,\gamma)P^{31}$ experiments described above the detectors were placed at $+90°$ and $-90°$ with respect to the proton beam. The

The measurement of triple angular correlations serves as a tool to determine, in many cases uniquely, spins and parities of the levels involved. Therefore a description of the

application of the sum-coincidence method to a triple angular correlation measurement is included here.

The example chosen is the resonance at $E_p = 760$ keV in the reaction $Si^{30}(p,\gamma)P^{31}$. In this experiment the detectors are placed at a distance of 10 cm from the target. Crystal 1 can rotate in the plane determined by the proton beam and by crystal 2 as elucidated in the lower insert in fig. 10. The resonance level decays through a weak ground-state transition and through three cascades via the levels at 1.27, 2.23, and 3.51 MeV. The spectra given in fig. 10 are taken at angles of 90°, 45°, and 0°, respectively. They show a strong anisotropy of the 1.27 and 6.76 MeV gamma rays. The other gamma rays all are slightly anisotropic. The sum peak itself gives (after correction for back-ground and summing effects in crystal 1) the angular distribution for the ground-state transition. In the measurement the ground-state transition appears almost isotropic. The implications of these measurements will not be discussed here.

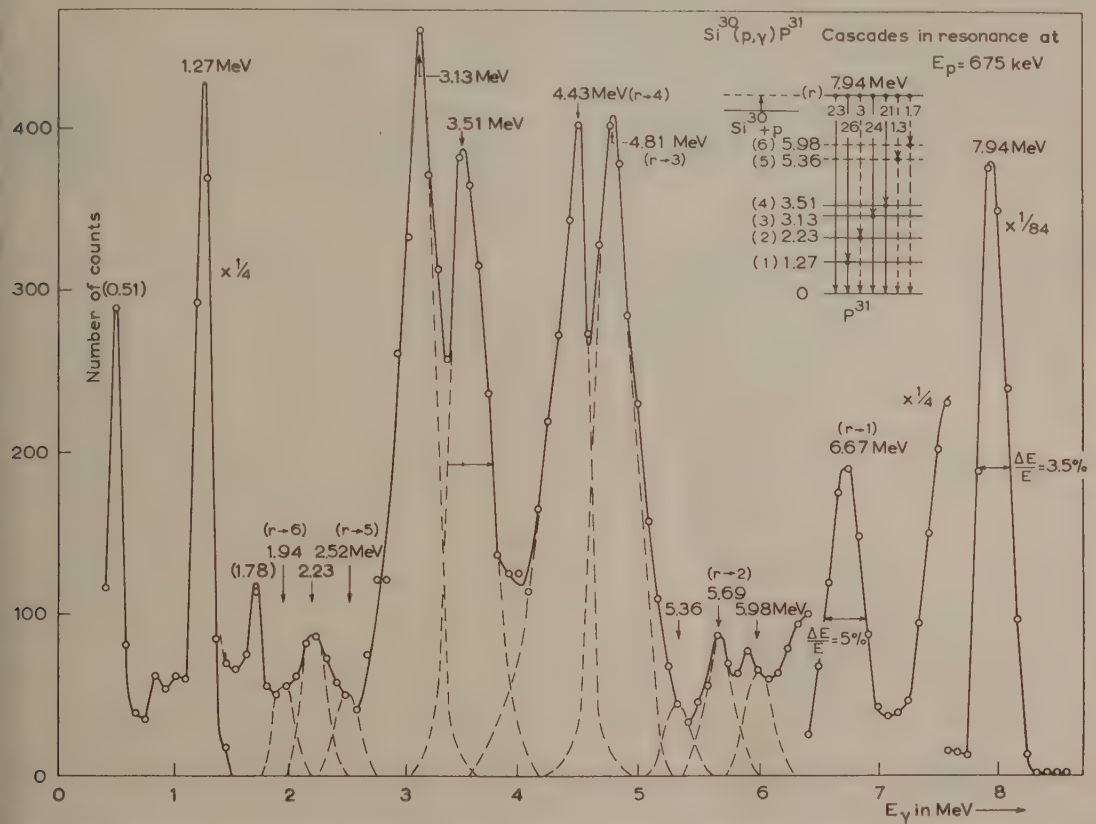

Fig. 9. Sum-coincidence measurement with 4″ crystals showing cascades in the reaction $Si^{30}(p,\gamma)P^{31}$ at $E_p = 675$ keV. The sum channel is set at 7.94 MeV. The decay scheme given in the insert can be derived from this measurement. An indication $(r \rightarrow i)$ above a peak points to the position of the corresponding transition in the decay scheme. The peak at 1.78 MeV is of analogous origin as the peak at 0.51 MeV (see § 5.2.4).

7. Conclusions

In sections 4 and 5 theoretical and experimental results are given for the application of the sum-coincidence method to the measurement of cascades of two gamma rays. An extension of this method to cases where three

transitions determine a sequence is easily possible. It will not always be necessary to sum the signals from all three detectors involved. For example triple cascades having one transition γ_1 in common (where E_{γ_1} is smaller than the energy of all other gamma rays) can be observed by detecting γ_1 with a third crystal and requiring a coincidence between the signal from crystal 3 and the sum signal from crystals 1 and 2. The sum channel in this case has to be set at the total available energy minus E_{γ_1}.

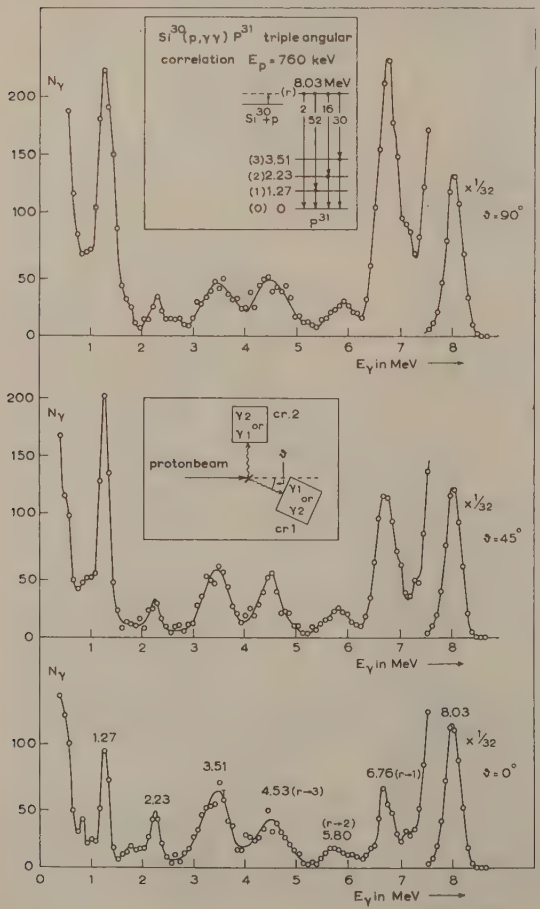

Fig. 10. $Si^{30}(p,\gamma\gamma)P^{31}$ triple angular correlation at $E_p = 760$ keV. The arrangement of the crystals with respect to the proton beam is given in the lower insert. The first and the second gamma ray of a cascade are denoted by γ_2 and γ_1 respectively. The spectra taken at angles of 90°, 45°, and 0° show the angular correlations of six gamma rays with respect to the proton beam. The energies of the gamma rays are given in the spectrum at $\vartheta = 0°$. The decay scheme is presented in the upper insert. Note the strong anisotropies of the gamma rays at 1.27 and 6.76 MeV. The sum peak represents (after subtraction of background and correction for summing effects in one crystal) the angular distribution of the ground-state transition with repsect to the proton beam.

Another example is a radioactive isotope emitting beta and gamma radiation. Here a special sequence of one beta transition and two gamma transitions can be selected by using a beta detector insensitive to gamma rays. Then the requirement that beta particles in a certain energy range be in coincidence with a sum pulse from the gamma detectors can select this special sequence. Thus all gamma cascades are observed deexciting the level fed by the selected beta transition.

8. Acknowledgements

This investigation is part of the research program of the "Stichting voor Fundamenteel Onderzoek der Materie", and was made possible by financial support from the "Nederlandse Organisatie voor Zuiver Wetenschappelijk Onderzoek".

The author wishes to express his gratitude to Prof. P. M. Endt and Dr. P. B. Smith for their participation in the experiments and for kindly reading the manuscript and suggesting valuable improvements.

NUCLEAR INSTRUMENTS 3 (1958) 69–72; NORTH-HOLLAND PUBLISHING CO. – AMSTERDAM

SPECTROMETRE POUR PARTICULES LOURDES

L. BIANCHI, E. COTTON et C. MILEIKOWSKY†

Centre d'Etudes Nucléaires de Saclay

Reçu le 10 Décembre 1957

For light nuclei reactions, the energy of the emitted particle depends appreciably on the emission angle with a double focusing spectrometer using a large entrance angle, this variation can be of several %. Our experiments allowed to test for the first time this improvement of energy resolution with our astigmatic system ($n = 0.57$) and with a variable tilting angle of exit slit (after suggestion of Curt Mileikowsky).

1. Caractéristiques de l'Appareil

Ce spectromètre est d'un type proposé par l'un de nous[1]) et réalisé par la firme L.K.B. (Suède) pour le Centre d'Etudes Nucléaires de Saclay.

L'angle solide d'entrée étant assez important et afin de pouvoir étudier les réactions sur noyaux légers dont l'effet de recul est notable, le principe suivant a été adopté:

On introduit un astigmatisme ($n = 0.57$) qui sépare les images radiales et axiales. Dans le cas où la distribution en énergie des particules est indépendante de l'angle d'émission (source radioactive ou pratiquement diffusion sur noyaux lourds), l'image d'un point est une droite parallèle au champ. Dans le cas contraire (réactions sur noyaux légers), on obtient une raie inclinée d'un angle ψ sur cette direction. Cet angle a été calculé en fonction de $\partial H/\partial r$ et $\partial E_2/\partial\theta$ [2]) et nous avons appliqué cette formule approchée ici:

$$\psi \sim \text{arc tg}\left[\frac{2}{5}\frac{1}{(1-n)(2n-1)}\sqrt{M_1M_2\frac{E_1}{E_2}}\frac{\sin\theta}{M_2+M_3}\right. . \tag{1}$$

1.1. CHAMPS DE FUITE

Les études faites sur l'appareil initial de Stockholm ($n = 0.5$) ont montré que les champs de fuite déterminent un secteur réel de déviation de 191° 4 au lieu des 180° des pièces polaires (voir fig. 1).

[1]) C. Mileikowsky, Arkiv för Fysik **7** (1954) no. 3.
[2]) C. Mileikowsky, Arkiv för Fysik **7** (1954) no. 5.

Tenant compte de ce secteur réel, nous avons disposé l'objet et le système de détection suivant le schéma et avons vérifié sur les trajectoires des

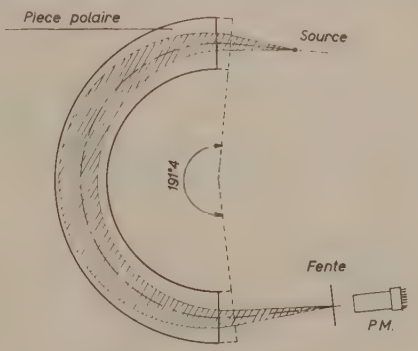

Fig. 1. Schéma de l'appareil.

particules que nous avions effectivement le même secteur de déviation avec $n = 0.57$ et non 0.5.

1.2. RÉGULATION DU COURANT DE L'ÉLECTRO-AIMANT

Grâce à une régulation électronique classique, L.K.B., le courant a été maintenu à 2×10^{-4} près, alors qu'il nous était garanti à 1 pour mille. La courbe d'aimantation montre une bonne linéarité de 0 à 12 000 gauss. Comme nous n'avions pas à notre disposition de mesure du champ et que nous travaillions entre 3 et 4 000 gauss, il nous a été possible de garder une bonne

† A.S.E.A. Västerås (Suède).

précision sur la résolution, sinon sur les mesures d'énergie, par une simple lecture de l'intensité du courant d'aimantation.

2. Dispositif Expérimental

2.1. DIAPHRAGMES DE DÉFINITION DE L'OBJET

Après les entretiens avec le Dr. Phillips (Rice Institute), nous avons disposé des diaphragmes en série de façon à éviter les effets de diffusion sur les lèvres réglables du diaphragme initial.

2.2. DÉTECTION

Nous avons utilisé des photomultiplicateurs Dumont dont la photocathode était enduite de sulfure de zinc. Le grandissement étant sensiblement égal à 1, nous avons disposé des fentes de définition devant le P.M. ayant la même hauteur que l'objet.

2.3. NATURE DES CIBLES

Nous disposions de cibles minces fabriquées par évaporation d'or sur formvar. Différentes épaisseurs ont été employées, entre autres, 10 μg d'or sur 10 μg de formvar et 50 sur 50.

3. Expériences

3.1. ENERGIE DES PROTONS INCIDENTS

L'étalonnage de la machine ayant été modifié, nous avons pu évaluer l'énergie des protons

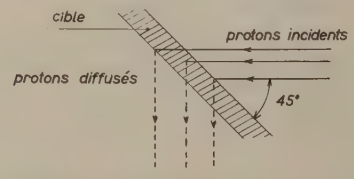

Fig. 2. Disposition de la cible par rapport au faisceau.

incidents en faisant le rapport de l'énergie des protons diffusés élastiquement sur l'or à celle des α du Th C précédemment utilisés comme test de l'appareil. La valeur de E était sensiblement 3.18 MeV.

L'expérience consistait en l'étude des diffusions élastiques de protons sur l'or, le carbone, l'oxygène, observées à 90° par rapport à la direction du faisceau incident.

3.2. EXPÉRIENCE SUR L'OR

Afin de retrouver rapidement le pic sur l'or, nous avons d'abord utilisé un spot large de 1 à 2 mm, pour avoir un comptage suffisant. La résolution obtenue était évidemment assez mauvaise (largeur à mi-hauteur 4 pour mille).

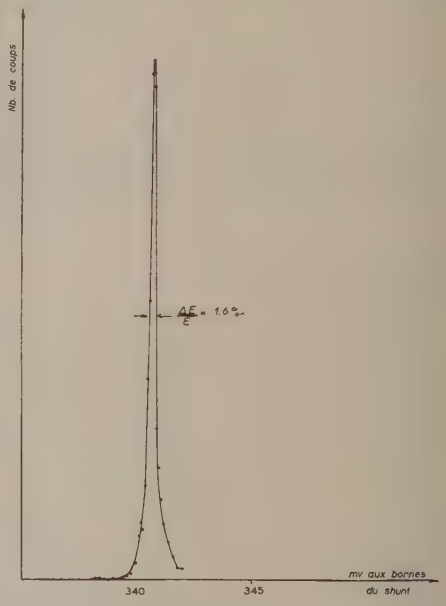

Fig. 3. Pic de diffusion sur Au (hauteur objet: 0.5 mm).

Par la suite, nous avons réduit la hauteur du spot, donc de l'objet, jusqu'à ½ mm. La largeur à mi-hauteur était alors de 1.5 pour mille (fig. 3).

3.3. EXPÉRIENCES SUR LE CARBONE

Les expériences précédentes nous ont servi de référence, puisque nous désirions observer des réactions sur noyaux légers. Nous avons tout d'abord calculé l'angle d'inclinaison de l'image d'après la formule de Mileikowsky[1]) et avons trouvé $\psi \approx 30°$ avec $\theta = 90°$ (en fait un calcul précis donne $\psi = 29° 5'$).

Avec la fente de définition parallèle au champ, nous avons facilement trouvé le pic du carbone, ayant une grande largeur comme prévu (1.2% à mi-hauteur) (fig. 4). Nous avons ensuite placé la fente dans deux positions à $\pm 30°$: la variation de la largeur à mi-hauteur observée a été

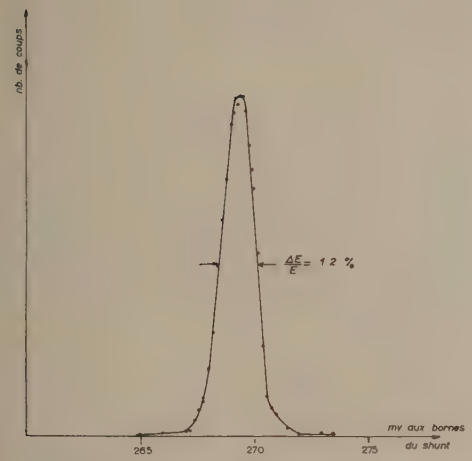

Fig. 4. Pic de diffusion sur ^{12}C (fente parallèle au champ).

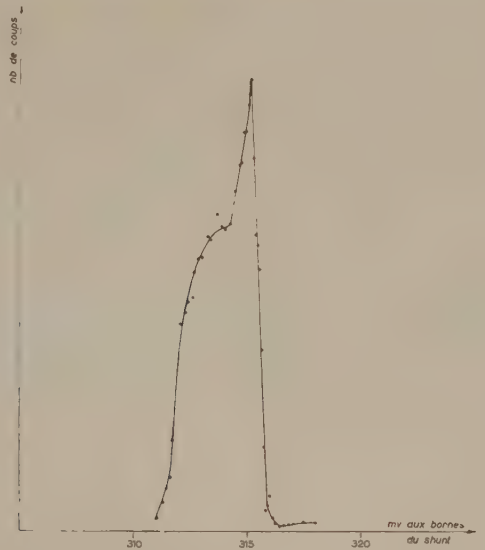

Fig. 5. Pic de diffusion sur ^{12}C (fente image inclinée de + 30°).

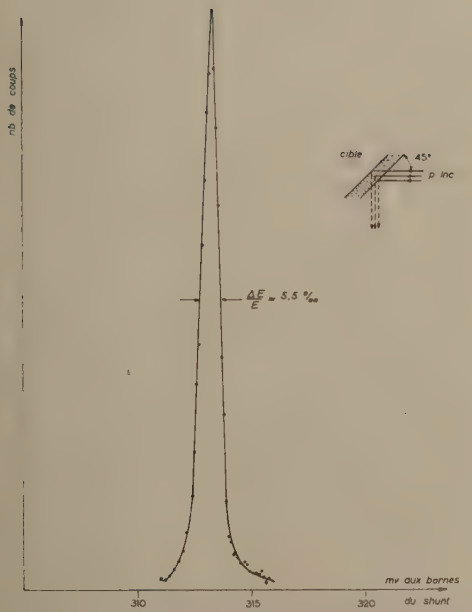

Fig. 6. Pic de diffusion sur ^{12}C (fente inclinée de — 30°).

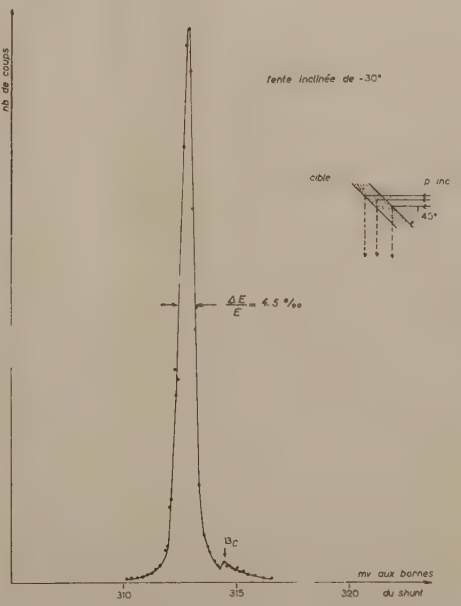

Fig. 7. Pics de diffusion sur ^{12}C, ^{13}C (fente inclinée de — 30°).

très importante; dans le cas favorable, nous avons obtenu d'abord 5.5 pour mille (fig. 6).

La différence existant entre ces largeurs à mi-hauteur des pics du carbone et de l'or peut être due à plusieurs causes: dépôt de carbone sur les deux côtés de la cible, élargissement dû à la cible car les particules traversent deux fois l'or, approximations faites sur ψ. Ainsi en disposant la cible de façon à avoir le même trajet des particules quel que soit l'endroit où se fasse la diffusion à l'intérieur ou à la surface de la cible (fig. 2), nous avons obtenu un pic de diffusion sur le carbone, dont la largeur à mi-hauteur était de 4 pour mille (fig. 7).

Au passage nous avons noté également une nette amélioration de la résolution du pic de diffusion, sur ^{16}O, bien que l'angle d'inclinaison de la fente de définition ne soit pas convenable.

Les résultats très encourageants obtenus sur le carbone nous montrent que l'astigmatisme introduit dans l'appareil doit donner entière satisfaction pour l'étude des réactions sur noyaux légers. Ainsi, il nous a été possible de séparer les pics de diffusion élastique de ^{12}C et ^{13}C distants en énergie de 35 keV pour une énergie incidente de 3.18 MeV.

NUCLEAR INSTRUMENTS 3 (1958) 73–79; NORTH-HOLLAND PUBLISHING CO. – AMSTERDAM

DIRECT-COUPLED AMPLIFIER FOR THE MEASUREMENT OF SMALL CURRENTS

B. R. F. KENDALL

Department of Physics, University of Western Australia, Nedlands

Received 17 March 1958

Methods for the reduction of grid current noise and leakage currents in direct-coupled preamplifier circuits are discussed. It is shown that, by combining a cathode follower preamplifier with a negative feedback output circuit, input grid resistors of very high value can be used. The construction and performance of an amplifier using these principles is described. Features of this circuit are a high zero stability and an adjustable time constant.

1. Introduction

During the course of work in the Mass Spectrometry Laboratory of this Department on the comparison of ion currents of the order of 10^{-14} ampere, it was found necessary to develop a direct-coupled amplifier capable of use with input grid resistors up to 10^{13} ohm in value, and suitable for operation with standard types of mass spectrometer ion collectors. Minimum fluctuation of the output zero was essential and an amplifier time constant adjustable from several seconds down to about 0.05 second was desired so that ion current transients could be investigated.

The amplifier to be described meets these requirements and also offers a number of advantages over more conventional circuits. Grid current noise originating in the preamplifier tube is minimised and the effects of leakage and grid currents in the preamplifier circuit are very greatly reduced. This allows the use of high values of grid resistor in the input circuit without the need for highly specialised electrometer tubes with very low grid current. These features are obtained with only moderate overall loop gain so that any tendency towards oscillation due to phase shift at the input grid is reduced. The amplifier has proved reliable in operation and is easily constructed from standard components.

2. General Theory

A comprehensive review of the theory and practice associated with the measurement of small direct currents has been given in a series of papers by Yarwood and Le Croissette[1]) and also by Jervis[2]). The general theory of direct-coupled amplifiers has been given by Kandiah and Brown[3]) and many others. In view of the extensive literature on this subject, the standard approximations for the effects of negative feedback with loop gains much greater than unity will be quoted without derivations.

3. Reduction of Grid Current Noise in the Electrometer Triode

Theoretical treatments of the contributions of various effects to the total noise observed in an electrometer triode measuring circuit have been given by Barnes and Silverman[4]), Hafstad[5]) and van der Ziel[6]).

In general the grid current I_g of such a tube may be expressed as

$$I_g = I_p - I_e \qquad (1)$$

where I_p is a contribution due largely to the flow of positive ions to the grid and emission of electrons by the grid, and I_e is the contribution due to flow of electrons to the grid.

The effective mean square voltage generated

[1]) J. Yarwood and D. H. Le Croissette, Electronic Engng. 26 (1954) 14, 64, 114.

[2]) M. W. Jervis, Electronic Engng. 26 (1954) 100.

[3]) K. Kandiah and D. E. Brown, Proc. Instn. Elect. Engrs. 99 pt (ii) (1952) 314.

[4]) R. B. Barnes and S. Silverman, Revs. Mod. Phys. 6 (1934) 162.

[5]) L. R. Hafstad, Phys. Rev. 44 (1933) 201.

[6]) A. van der Ziel, Physica 9 (1942) 177.

by the two components at the grid is proportional to their sum I_n, the effective noise current. Van der Ziel has shown that, using Hafstad's value of 2×10^{-15} A for I_n in the FP54 electrometer tube, the shot effect of the grid current makes a significant contribution to the total noise only for input grid resistances greater than about 2.5×10^{13} ohm. For most electrometer tubes, however, I_n may be much larger. It has been shown[7]), that for the 959 tube used as an electrometer the value is not less than about 10^{-14} A and may be considerably greater; while work in this laboratory has shown that in the case of the 5803 triode, grid bias voltages only a few hundred millivolts from the optimum can greatly increase I_e giving $I_n = 10^{-13}$ A or more. Under these conditions grid current shot noise becomes important for input grid resistances greater than about 5×10^{11} ohm.

Noise from this effect can be minimised by ensuring that the electrometer tube potentials are controlled under all conditions of operation so that I_n is kept low.

If the grid of an electrometer tube is allowed to float at its equilibrium potential, $I_g = 0$ and $I_p = I_e$. Above this potential, I_e increases rapidly. Below it, I_e falls to a very low value and the grid current is due mainly to the small and nearly constant current I_p. It follows that for minimum grid current shot noise the operating region should be at or below the equilibrium potential. Hafstad has reported a considerable improvement in the noise level for an FP 54 tube operated under these conditions.

Because the zero grid-current condition is readily detected by the amplifier itself without the use of special test equipment, this setting is normally used in the present instrument. Experience has shown, also, that there is less likelihood of high-frequency oscillation due to the internal grid-plate capacity if the electrometer tube is run under these conditions.

4. Reduction of Effect of Leakage and Grid Currents in the Preamplifier

For satisfactory operation of the preamplifier circuit, only a negligible proportion of the input current should flow from the collector (C in fig. 1) through the tube grid and via leakage resistances to earth. It follows that the input impedance of the system, R_1, must be low compared with both the leakage resistance from the collector line to earth, R_e, and the tube grid input impedance, R_{ge}, measured between grid and earth.

Let R_{gf} be the input impedance of the electrometer tube measured between grid and filament, and let R be the value of the input grid resistor. The input impedance between collector and earth of an amplifier which has negative feedback applied to the input grid resistor and which has an overall loop gain of G_3 is given by the expression

$$R_1 \approx R/G_3 \,. \tag{2}$$

It will be shown that G_3 for the amplifier to be described is adjustable between 10 and 250, but is normally operated at an intermediate value. Taking 100 as a typical value for G_3, it follows that if R_1/R_e is not to be greater than 0.01, then R must not be greater than R_e. In practice R_e is easily made greater than 10^{14} or 10^{15} ohm and so the leakage current from collector to earth is always negligible.

For a preamplifier circuit of cathode follower type with effective loop gain G_1,

$$R_{ge} \approx G_1 R_{gf} \,. \tag{3}$$

It follows that if a cathode follower type of preamplifier circuit is combined with the conventional negative feedback system described above, then from (2) and (3),

$$R \approx G_1 G_3 \left(\frac{R_1}{R_{ge}}\right) R_{gf} \,. \tag{4}$$

Such an arrangement has been used in the amplifier to be described, G_1 having a value of about 60.

Taking $R_1/R_{ge} = 0.01$ as the maximum allowable ratio, it can be shown that even if R_{gf} for the electrometer tube employed is as low as 10^{12} ohm, R may be as high as 6×10^{13} ohm without the grid current becoming significant relative to the total input current.

[7]) C. S. Wu and L. J. Rainwater, U. S. Atomic Energy Commission Report AECD-2049.

5. Advantages of Low overall Loop Gain

It follows from the preceding discussion that the product G_1G_3 for this amplifier lies between 600 and 15 000 although the overall loop gain is only between 10 and 250.

may give such a high hum output to a chart recorder as to greatly reduce its sensitivity.

With grid resistors of high value the phase shift in the feedback loop at the input grid may approach 90 degrees; this, combined with the

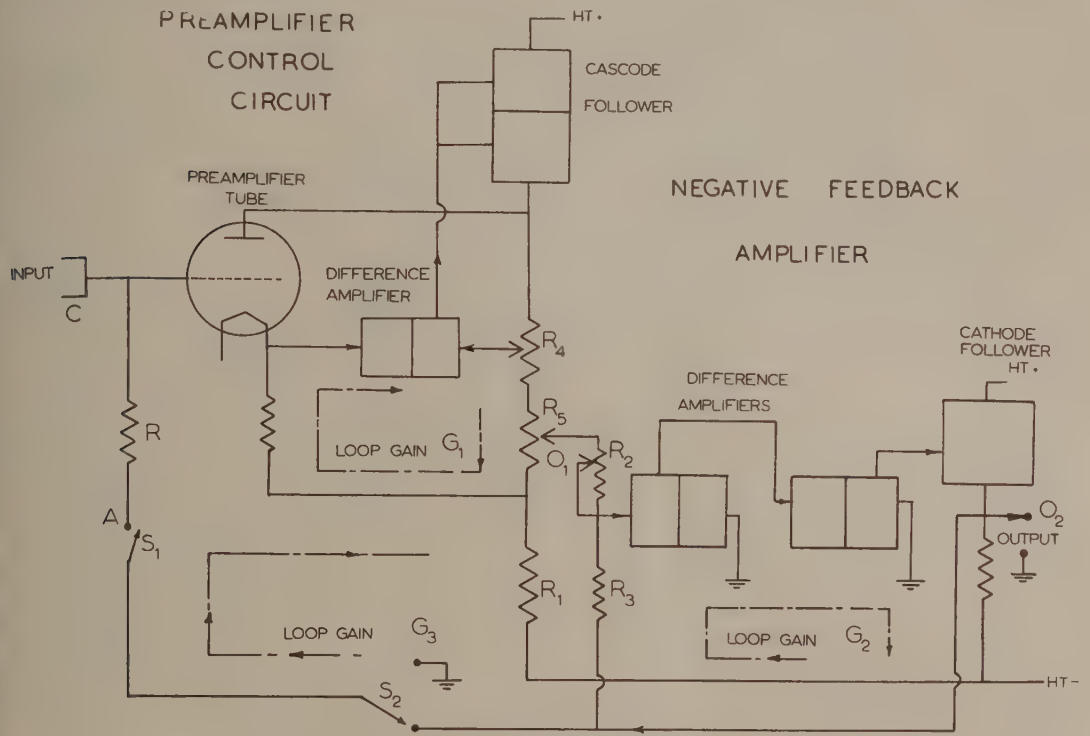

Fig. 1. Block diagram of the amplifier.

It can be shown that similar reductions in the effects of preamplifier tube grid current can be obtained using a conventional single-loop negative feedback amplifier with overall loop gain equal to G_1G_3. Because conventional mass spectrometer ion collectors have a substantial capacity to earth the negative feedback is usually applied to the end of the grid resistor, in order to reduce the input time constant to a reasonable figure. A number of difficulties arise when such a system is employed in a high-gain circuit.

Attenuation of the feedback signal at mains supply frequency is likely to be severe; in such a case slight hum pickup in the amplifier circuit

very high loop gain and other small phase shifts occurring elsewhere in the circuit, frequently causes the system to oscillate. Even if oscillation does not occur, the undesirable peaks in frequency response may lead to a considerable increase in the output noise level.

The amplifier to be described has been found to be comparatively free from these troublesome effects.

6. The Amplifier Circuit

The circuit consists of two main sections, each with a closed negative feedback loop, and with the output of the second fed to the input of the first by a connection to the input grid resistor.

The loop gains of these sections are G_1 and G_2, while G_3 is the overall loop gain of the whole system.

A block diagram of the amplifier is shown in fig. 1.

Section 2 is a conventional negative-feedback amplifier with variable gain. This allows reduction of the input system time constant to the desired value and contributes further to the reduction of leakage and grid-to-filament im-

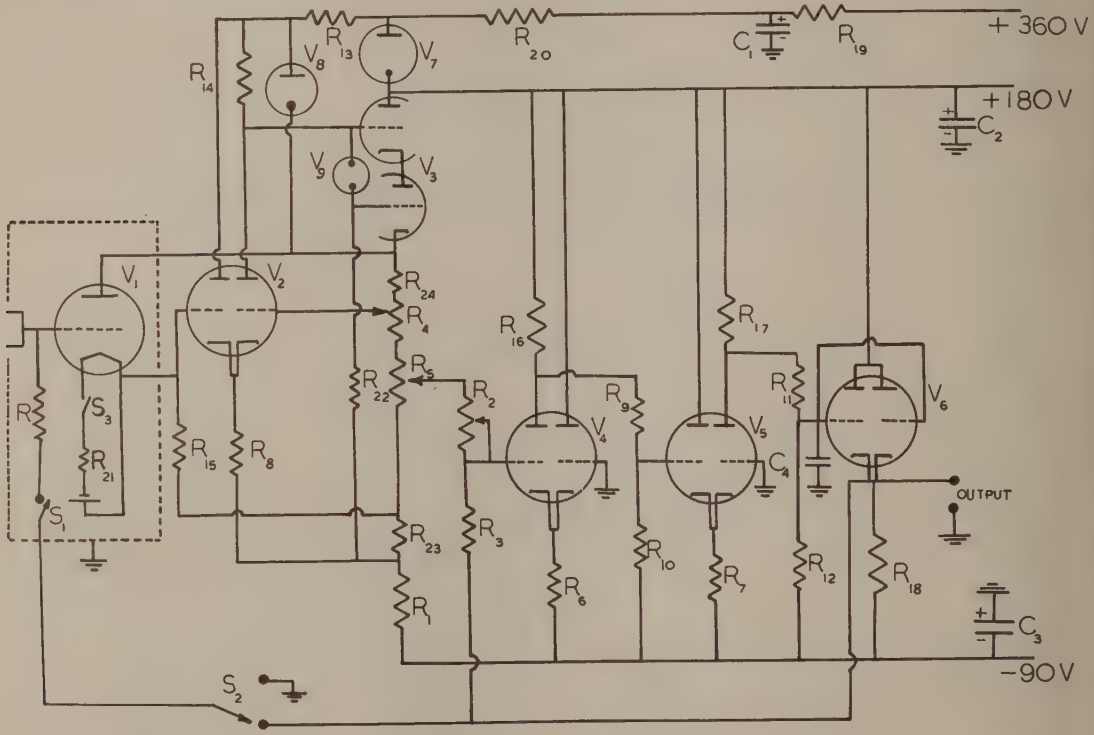

Fig. 2. Circuit diagram of the amplifier.

V_1:	Victoreen 5803	S_2:	S.P.D.T.	R_{19}:	2 kΩ
V_2, V_4, V_5:	12AX7	S_3:	S.P.S.T.	R_6, R_7, R_8:	68 kΩ
V_3, V_6:	12AT7	R, R_{21}:	see text	R_9, R_{10}, R_{11}, R_{12}, R_{13}:	500 kΩ
V_7:	0A2	R_1:	70 kΩ low temperature coeffct. Wire wound.	R_{14}, R_{15}:	220 kΩ
V_8:	85A2;			R_{16}, R_{17}, R_{22}:	160 kΩ
V_9:	NE2, NE2A or NT2.	R_2:	variable 0–500 kΩ	R_{18}:	15 kΩ
C_1, C_2, C_3:	16 mF 600 V	R_3:	5.6 MΩ	R_{20}, R_{24}:	4.7 kΩ
C_4:	0.005 mF.	R_4:	1 kΩ potentiometer	R_{23}:	10 kΩ
S_1:	see text	R_5:	2 kΩ potentiometer		

Section 1 consists of a cathode-follower electrometer circuit similar in principle to those described by Mühleisen[8]), Brewer[9]) and Murray[10]) This portion of the system is used as a control circuit for the electrometer tube, maintaining minimum grid current and contributing to the reduction of effects due to the finite grid-to-filament input impedance.

pedance effects in the preamplifier. It also provides a low-impedance output suitable for

[8]) R. Mühleisen, Z. f. Naturf. **6a** (1951) 667.

[9]) A. W. Brewer, J. Sci. Instr. **30** (1953) 91.

[10]) C. T. Murray, Dept. of Electrical Engineering, The University of Sydney, Private Communication†.

† To appear in Australian Atomic Energy Commission Report on Symposium on Peaceful Uses of Atomic Energy, Sydney (June 1958).

driving a moving coil meter or chart recorder.

A detailed circuit diagram of the amplifier is shown in fig. 2.

7. Preamplifier Control Circuit

This section of the circuit is a simplified version of that used by Murray as the basis of an amplifier with high input impedance and high zero stability. Murray, however, used a constant-current pentode in place of R_1 and reduced the system time constant to a low value by completely surrounding the preamplifier and collector assembly with a shield operated from the output (O_1 in fig. 1), the grid resistor being earthed at A. Such a method is not conveniently applicable to most existing mass spectrometer ion collectors, particularly in cases where a number of collectors are close together. Replacement of the constant current tube by a resistor eliminates one of the more critical portions of Murray's circuit. Although the effective loop gain G_1 is reduced from a very high value to about 60, this lower figure still gives satisfactory circuit operation.

The control circuit is basically of the cathode follower type. A signal appearing on the grid of the preamplifier tube causes a shift in the mean filament potential. This is amplified by a difference amplifier and fed to the grids of the cathode follower causing the upper end of the cathode resistor, from which the preamplifier plate supply is derived, to follow the input signal. Thus the plate and filament potenitals of the preamplifier tube follow the grid potential and this tube runs at nearly constant grid bias. Adjustment of the tapping on R_4 allows this constant bias to be set at that value for which the tube grid current is zero. The action of the control circuit will also raise the input impedance of the preamplifier tube R_{ge} measured between grid and earth to a value much greater thant the grid-filament input impedance R_{gf}, according to the relationship given earlier,

$$R_{ge} \approx G_1 R_{gf} .$$

The Victoreen 5803 electrometer triode was used in the preamplifier mainly because of its low filament current and its established reliability. Although the grid current and grid input admittance are higher than is the case for more specialised tubes, satisfactory results are still obtainable with this circuit.

8. Negative Feedback Amplifier

The shift in potential of O_1 in fig. 1 is proportional to and very nearly equal to the change in potential of the electrometer tube grid. This signal is amplified by two difference amplifiers and a low impedance output taken from O_2, the cathode of the cathode follower. From this point negative feedback is applied to the input of this section and to the input grid resistor at A. The loop gain G_2 is approximately 500 and is normally large relative to the ratio R_3/R_2, therefore

$$G_3 \approx R_3/R_2 . \qquad (5)$$

Adjustment of R_2 allows G_3 to be varied from 10 to a value approaching that of G_2. In normal use, a range of 10 to 250 is convenient. Because G_3 is much greater than unity, the output voltage at O_2 will be very nearly equal to the voltage across the grid resistor R. It is therefore proportional to the input current.

The input time constant, T, is given by

$$T = CR_1 \qquad (6)$$

where C is the input capacitance to earth of the collector assembly.

From (2) and (5)

$$T \approx CRR_2/R_3. \qquad (7)$$

The time constant may therefore be controlled by adjustment of R_2.

9. Constructional Data

Standard components and constructional procedures have been employed throughout, except in the preamplifier assembly. Unless otherwise specified, all resistors are carbon composition types of 1 watt rating and 10% tolerance.

Potentiometer R_5 should have a resolution appropriate to the accuracy of zero adjustment required, a 10-turn helical potentiometer being desirable for best results.

The preamplifier was built around a polystyrene rod which carries the contacts for the switch S_1. This assembly was enclosed in a light-tight housing which could be evacuated or filled with dry air when mounted on the mass spectrometer. External connections were made through an octal plug sealed into the housing, and to the switch arm which slides through O-ring seals in the housing, from which it is electrically insulated. Connection to the ion collector was made by a short flexible wire and a glass-insulated lead-through.

10. Power Supplies

A stable heater supply is essential. A commercial 6 volt battery charger with one or two 6 volt radio accumulators floating across its output has been found satisfactory.

The filament of the 5803 triode draws only 10 mA and is conveniently supplied from a 25 Ah, 2 volt accumulator with a 75 ohm series resistor, enclosed in a shielded box.

The high-tension voltages may be provided by conventional stabilised power supplies or from a single supply using low-impedance output tappings. A cathode-follower output tapping similar in principle to that used by Hibbard and Caro[11]) has been found very satisfactory. For optimum stability a mains stabiliser should be used.

If more than one amplifier is to be run from the same power supplies, or if output indicators of resistance lower than 1000 ohm are to be employed, the impedance to earth of the H.T. lines should be kept low (less than 200 ohm) to prevent amplifier interaction and oscillation.

Provision must be made for simultaneous application and removal of all H.T. voltages, and for opening of these lines in the event of power failure. If such precautions are not taken, high anode voltages may be applied to the electrometer tube during warming-up of the power supplies, shortening its life and increasing its long-term drift rate.

Maximum stability and reliability will be obtained if the amplifier is run continuously.

[11]) L. U. Hibbard and D. E. Caro, J. Sci. Instr. **30** (1953) 378.

11. Adjustment for Zero Grid Current

With the time constant control R_2 at maximum, S_2 switched to earth and grid leak switch S_1 closed, R_5 should be set to give zero output. S_1 is then opened allowing the grid to float and R_4 is set for zero output. S_1 is closed and output zeroed with R_5. The cycle is continued until the output zero shifts by less than about 0.25 volt when S_1 is closed. This completes adjustment. Switching S_2 to output completes the feedback loop and final zeroing with R_5 makes the amplifier ready for operation.

Adjustment may be hastened if a resistor high in value with respect to the grid resistor R is connected across S_1.

12. Linearity

The amplifier was designed for the accurate comparison of currents of the same order, rather than to give an output accurately equal to the input voltage. In fact, the low (but stable) gain G_3 of the system at longer time constant settings will cause the output voltage to be up to 10% different from the input voltage. Due to the high value of G_2, however, the output (for given time constant) will be proportional to the input within very much smaller limits, over a range of several volts.

13. Fluctuations of the Output Zero

Several chart recordings of output zero fluctuations have been taken, using a Brown model 153×12 Recorder modified to give improved frequency response.

Table 1 shows the maximum deviations of output zero over typical 1 minute periods, for three values of grid resistor. No measurements have been made with resistors of higher orders of magnitude because these were not readily available and their use was not essential; however, it is considered that operation with input resistors up to 5×10^{13} ohm in value should not present any difficulty, if the input capacity is kept reasonably low.

Comparison of the frequency response curves for the modified and unmodified recorder indicates that the equivalent noise figures for

TABLE 1

Short-term zero fluctuations

Grid resistor R (ohm)	Loop gain G_3	Amplifier time constant T (sec)	Max. deviation from zero in 1 minute (millivolt)	Equivalent RMS noise for unmodified Recorder (millivolt)
10^{11}	20	0.15	$\pm$ 0.12	0.02
10^{12}	20	1.5	$\pm$ 0.3	0.05
5×10^{12}	42	0.5†	$\pm$ 1.2	0.20

† Modified preamplifier housing and collector system with reduced input capacitance.

the latter case are less than one half of the quoted values in table 1.

It can also be shown from statistical considerations that the maximum measured deviations from zero are probably between three and five times the equivalent root mean square deviations.

It may therefore be concluded that the RMS noise if measured on the unmodified Brown recorder would not be larger than the figures given in the final column of table 1.

The long-term zero drift during continuous operation has been measured on several occasions and is normally less than about 1 mV per hour for grid resistors in the range 10^{11}–10^{12} ohm.

14. Acknowledgements

The author wishes to record his appreciation of the interest shown in this project by Mr. C. T. Murray of the University of Sydney. During 1955 Mr. Murray communicated details of his newly developed high stability amplifier to this laboratory and subsequently examples were constructed and tested by Dr. D. Greenhalgh and the author. Their stability was such as to justify the inclusion of similar features in the amplifier described in this paper.

Thanks are due also to Dr. P. M. Jeffery and Dr. W. F. Compston for their participation in many stimulating discussions and for much useful comment. The interest of Professor C. J. Birkett Clews in this project is gratefully acknowledged.

During the period in which this work was carried out, the author was the holder of a Research Studentship awarded by the Australian Atomic Energy Commission.

The project was supported financially by grants from Dr. K. W. Starr of Sydney, New South Wales, and from the University of Western Australia Research Grants Committee.

NUCLEAR INSTRUMENTS 3 (1958) 80–84; NORTH-HOLLAND PUBLISHING CO. – AMSTERDAM

DISTINGUISHING BETWEEN He^3 AND He^4 PARTICLES BY 'dE/dx' AND "E" MEASUREMENTS

R. W. P. McWHIRTER†, P. PALIT and E. H. BELLAMY

Department of Natural Philosophy, University of Glasgow

Received 20 January 1958

A new type of detector has been built to distinguish between He^3 and He^4 particles of a continuous energy spectrum ranging from about 10 to 30 MeV. It consists of two gridded ionisation chambers which measure the total energy of the particle in two fragments "E_1" and "E_2", in general E_1 being $< E_2$. The information is displayed in a cathode ray oscilloscope by a series of spots whose co-ordinates are proportional to the values of E_1 and E_2 for each particle. The positions of the spots are compared to calculated positions to determine the total energy and mass of the particle concerned. The apparatus has been used to study the reaction $\gamma + He^4 \rightarrow \pi^0 + He^4$ by picking up the recoil α-particle amidst a large background of He^3 and singly charged particles. It is currently being used to investigate the photodisintegration of oxygen, argon and krypton at high energies.

1. Introduction

A standard technique in high energy nuclear physics for distinguishing between particles of different mass is to measure simultaneously the specific ionisation and total energy of the particle. This method is particularly useful when the energy spectrum of the particles is continuous and when their momenta are sufficiently high to make the use of magnetic deflection both cumbersome and inefficient.

The method was earlier used to separate mesons from electrons and protons[1,2]) and was later extended to distinguish protons from deuterons[3]). Scintillation detectors are commonly used in these experiments but are unsuitable for distinguishing between He^3 and He^4 particles for the following reasons. Firstly, an extremely thin scintillator would be required for the dE/dx measurement. Thus a 15 MeV α-particle would lose about 5 MeV in passing through 0.003″ of plastic scintillator. Secondly, even for measuring the final energy of the particle, the non-linear variation of light output with energy loss from scintillating crystals for these densely ionising particles means that the effective separation between the two types is reduced and the necessary energy resolution is then difficult to achieve.

These considerations suggest that some form of gas ionisation counter should be used. Although the shortest pulse obtainable from these counters has much greater time duration than can be obtained from scintillation counters, the specific ionisation of the double charged particles is so high that their detection and resolution is not seriously affected even by the "pile up" of counts due to relatively high fluxes of electrons and photons.

2. Design and Construction

A device of the above nature has been built for studying the elastic photoproduction of neutral pions in helium, i.e., the reaction

$$\gamma + He^4 \rightarrow \pi^\circ + He^4$$

by detection of the recoil α-particles amidst a

† Now at U.K. Atomic Energy Research Establishment, Harwell, Berkshire, England.

[1]) T. Yamagata, M. Q. Barton, A. O. Hanson and J. H. Smith, Phys. Rev. **95** (1954) 574.

[2]) A. V. Tollestrup, J. C. Keck and R. M. Worlock, Phys. Rev. **99** (1955) 220.

[3]) B. Wolfe, A. Silverman and J. W. de Wire, Rev. Sci. Inst. **26** (1955) 504.

background of He^3 particles produced by reactions such as

$$\gamma + He^4 \rightarrow \begin{matrix} He^3 + n \\ He^3 + \pi^\circ + n \\ He^3 + \pi^- + p \end{matrix} .$$

The arrangement is shown in fig. 1. The γ-ray beam passed through a pipe filled with helium gas to a pressure of 2–5 atmospheres and the recoil helium nuclei were detected in two gridded ionisation chambers. These had a common H. T. electrode KL as shown, but the collector plates CD and GH were separate and measured 'dE/dx' and "E" respectively. Parts of GH and KL were bent outwards so as to include a reasonable solid angle of acceptance. The earthed guardring AB, and wire-conductors W, held at suitable electrostatic potentials with the help of the resistor chain R, maintained the required field distribution near the edges of the chamber. R consisted of miniature carbon resistors sealed inside glass tubes, so as to prevent "poisoning" of the chamber gas. An earthed strip EF was inserted between the two collector plates to reduce the capacity between them. This inter-electrode capacity had to be allowed for in analysing the data since the induced pulses between the two collectors gave a significant contribution to the observed pulse heights (30% was about the maximum value).

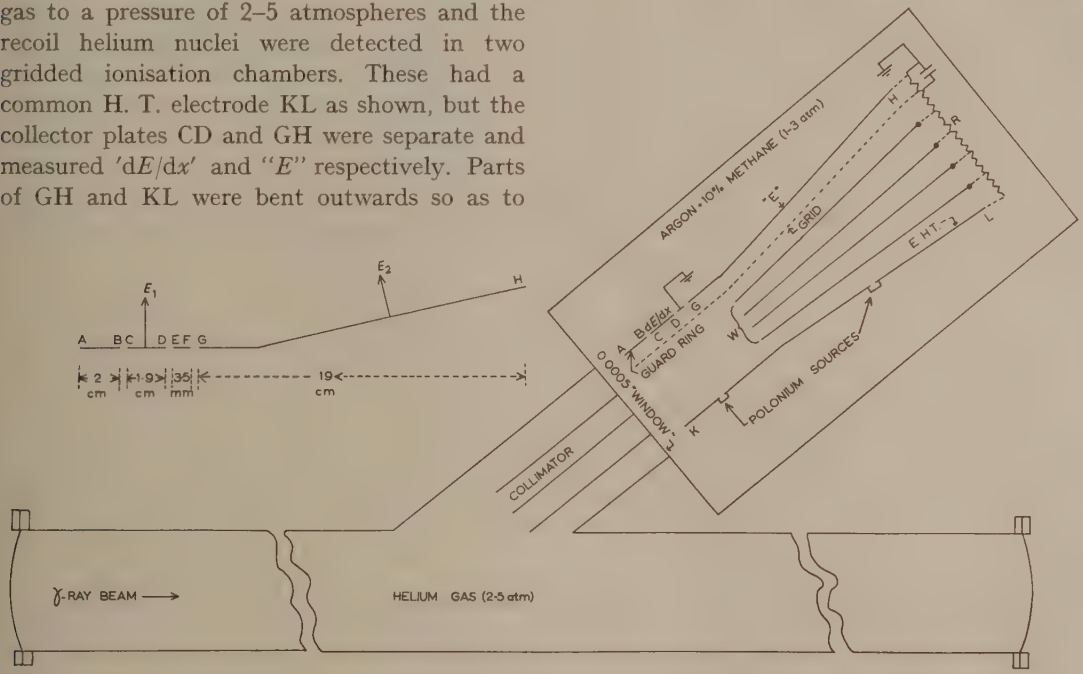

Fig. 1. General layout of the apparatus. Diagram is not to scale.

The precise value of this effect was estimated in two ways; firstly, by directly measuring the height of the pulse from each collector when a pulse of fixed voltage was applied to the other, and also by a direct measurement of the inter-electrode capacity C_{12} (2.2 pF) and the capacity of each collector to earth. The two sets of measurements were in mutual agreement. If C_{12} is increased, the separation between He^3's and He^4's is reduced.

Polonium sources were mounted at the back of the H.T. electrode and the α-particles emerged through small holes which partially collimated them. The chamber was filled with a mixture consisting of 90% argon and 10% methane to a pressure of 1 to 3 atmospheres and this gas mixture was separated from the helium in the target pipe by a "Melinex" window 0.0005" thick supported on a wire grid so as to be able to stand up to pressure differences of 1 to 2 atmospheres.

3. Operation and Characteristics

The mass and energy of the particle were determined from the energy losses E_1 and E_2 (or 'dE/dx' and "E"), as measured by the heights of the coincident pulses obtained from the pulse-height from desired heavy particles. The device essentially makes use of the different rise-times of a prompt pulse due to a single particle and a slowly rising "pile-up" pulse and after the inclusion of the second line, an electron

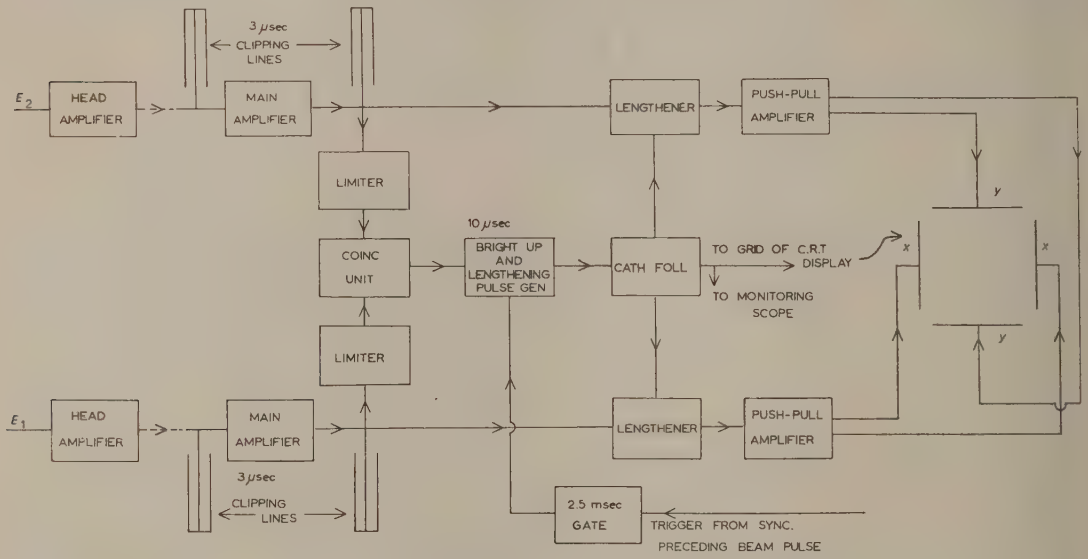

Fig. 2. Block diagram of the electronics.

collectors CD and GH when the particle passed from the target into the second ionisation chamber. The information was displaced on a cathode ray oscillograph, each coincidence giving rise to a spot whose x and y co-ordinates were proportional to E_1 and E_2 respectively. Fig. 2 gives the block diagram of the electronics. Square pulses of 3 μs duration were formed with shorted delay lines and after amplification, another 3 μs line was found necessary to eliminate the "pile-up" from the large number of electron pulses occurring during the bremsstrahlung beam pulse. This lasted for about 500 μs and for the run at a laboratory angle of 20°, it was estimated that approximately 100 electron pulses occurred during that time. With only one clipping line in each channel, this had the effect of superimposing the pulses from heavy particles on the top of a general background which was greatly reduced by the second line without the latter in any way affecting the pulse could only affect the height attributed to a heavy particle pulse if the two entered the chamber within three microseconds of each other.

The energy losses E_1 and E_2 varied between the limits 1.3 to 5 MeV and 2 to 23 MeV respectively. The statistical fluctuation on E_1 under typical conditions was about 25 keV. The distribution was still Gaussian and the Landau effect which makes the mean energy loss greater than the most probable energy loss was negligible under our conditions[4]).

The spots on the cathode ray screen were photographed, the normal running time per frame being 2 hours, the number of spots per frame varying between 7 and 20. The x- and y-axes for each frame were located using the pulses from the polonium α-sources fixed in each chamber. Coincidences were forced by joining the inputs

[4]) Rossi, High Energy Particles, (Prentice Hall Inc.) p. 31.

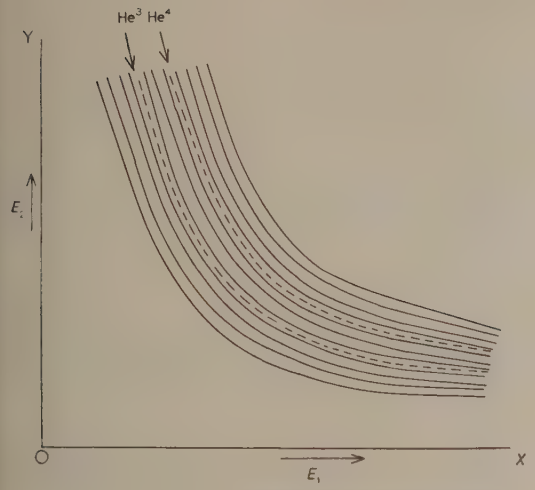

Fig. 3. Method of analysing the data (see text).

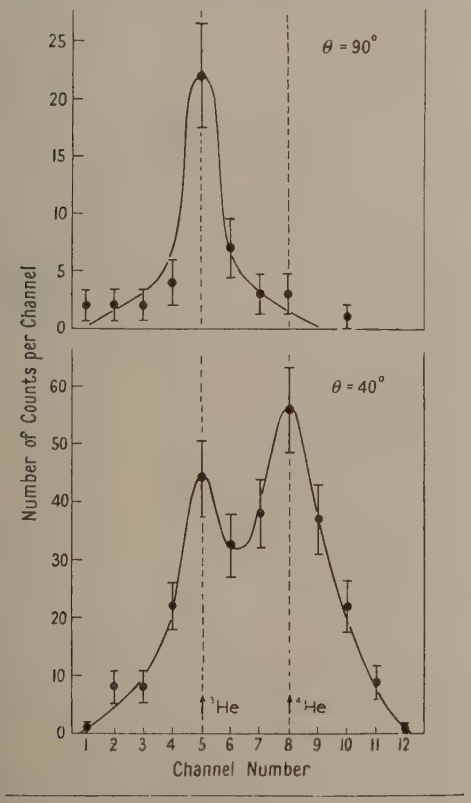

Figs. 4 and 5

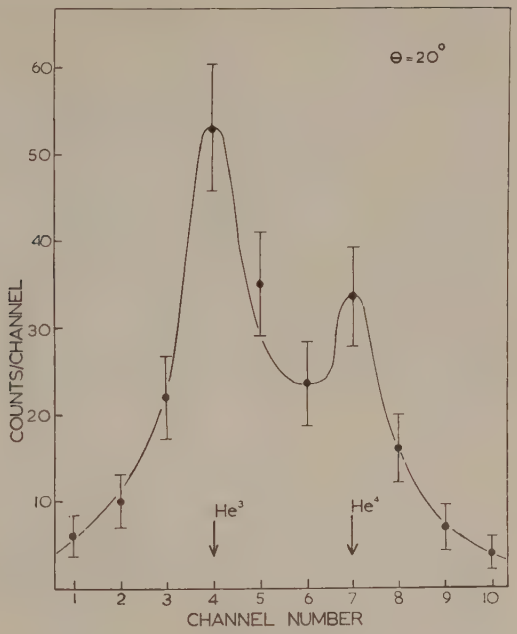

Fig. 6

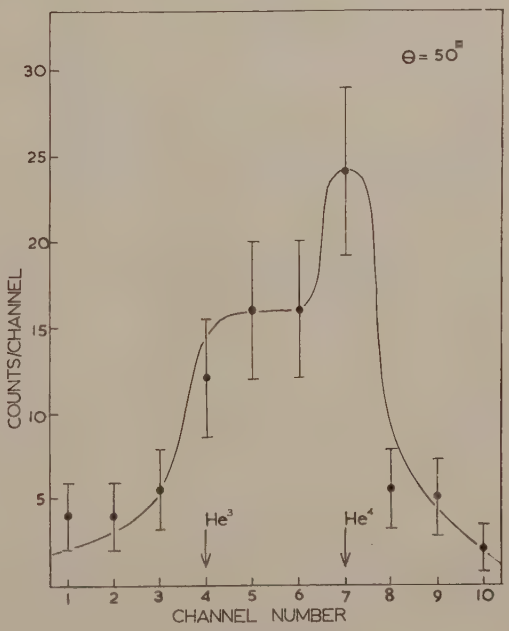

Fig. 7

Figs. 4, 5, 6 and 7. Typical curves showing the resolution of the detector at various angles.

of the coincidence unit and the x-axis was plotted by shorting to earth the input of the y-amplifier of the oscilloscope and vice-versa. This also afforded a calibration of the x-and y-deflections in terms of the energy loss, although the latter was done more accurately by repeating the procedure with a "wobble" superimposed at right angles to the deflections produced by the pulses from the polonium particles so that the spots were spread out in transverse direction and the region of maximum density could be accurately located. For any one set of runs the calibration measurements were in sufficient agreement for their average to be taken and used throughout.

The data was analysed in the following manner. The curves along which the spots were expected to lie were calculated on the basis of the calibration deflections, the geometry of the chamber, the gas pressure and the theoretical range energy relationships for the nuclei in argon. These were derived from the range energy data for air given by Rich and Madey[5]), the data of Bates[6]) being used to derive the relative stopping powers of air and argon below 5 MeV. The space between the curves and on either side of them was divided into channels of equal width by curves which closely followed the shape of the guiding ones (fig. 3). The number of points within each channel was then counted separately and thus a histogram was obtained. The resolution achieved is shown in figs. 4, 5, 6 and 7. Fig. 4 represents a run at a laboratory angle of 90° to the γ-ray beam. The kinematics of the reaction $\gamma + \mathrm{He}^4 \rightarrow \pi^\circ + \mathrm{He}^4$ rule out the possibility of emission of a He^4 particle at this angle. The histogram shows that not only was the intrinsic resolution of the device quite good, but that a peak was obtained at the proper channel which confirms that the basic analysis of the data was essentially correct, the calculated curves were of the proper shape and had the correct location. Coincidences were also obtained from a polonium α-source located so that α-particles passed through both chambers. By varying the gas pressure, the energy losses in each of the chambers were altered. There was good agreement between the observed and calculated position of the spots so obtained. Figs. 5, 6 and 7 represent the runs at 40°, 20° and 50° to the beam.

It can be seen from these histograms that the two types of nuclei are distinguishable and the device makes it possible to measure the flux of either He^3 of He^4 particles when both of them are present in comparable numbers. The apparatus is also being used to measure the relative yields of He^3 and He^4 particles from the photodisintegration of Oxygen, argon and krypton.

We would like to thank the synchrotron crew under Dr. McFarlane for running the synchrotron for us, and Professor P. I. Dee for his encouragement throughout.

[5]) M. Rich and R. Madey, Range Energy Tables (1954) U.C.R.L. 2301.

[6]) Bates, Proc. Roy Soc. A **106** (1924) 622.

NUCLEAR INSTRUMENTS 3 (1958) 85–89; NORTH-HOLLAND PUBLISHING CO. – AMSTERDAM

ON THE THEORY OF THE DIFFUSION CLOUD CHAMBER

IGOR SAAVEDRA

Laboratorio de Fisica Nuclear, Universidad de Chile, Santiago†

Received 10 February 1958

A revision is made of Shutt's theory by using more accurate expressions describing the transport phenomena in the chamber. This leads to a new expression for the temperature gradient. The importance of the correction thus introduced depends upon the particular components of the binary mixture considered.

1. Introduction

The theory of the diffusion cloud chamber was first discussed by Langsdorf in 1938[1]). An improvement of this theory was proposed by Succi and Tagliaferri[2]). A more complete description of the general mechanism was given by Shutt[3]). A summary of the existing theories has been given by Snowden[4]).

In this paper we shall revise the equations used by Shutt leading to an expression that describes the temperature distribution in the diffusion cloud chamber. In section 2 an exact expression for the mass flux is obtained by applying Chapman's diffusion theory[5]) to a binary mixture in the case that a temperature gradient is present. In the next section this equation is applied to the phenomena occurring in the chamber. A one-dimensional equation is obtained for the vapour flux and a diffusion equation that considers the temperature gradient is set up. In section 4 we show that the corresponding equations used by Shutt can only be valid if some particular assumptions are introduced, mainly that there is no temperature gradient. Our equations are then applied to the theory of the chamber following the same procedure used by Shutt. A new expression for the temperature gradient is thus obtained, and this is compared with Shutt's equation in the concluding section.

† Now at the Theoretical Physics Department, University of Manchester.

2. Thermal Diffusion in Binary Mixtures

The two constituents of a binary mixture are said to be diffusing relative to one another if the mean velocities of the two sets of molecules are not the same, that is, when $\bar{V}_1 - \bar{V}_2 \neq 0$, $\bar{V}_1$ and $\bar{V}_2$ being the mean absolutes (or relatives) velocities of each component.

According to Chapman and Cowling we have

$$\bar{V}_1 - \bar{V}_2 =$$

$$= -\left(\frac{n^2}{n_1 n_2}\right) D_{12} \left\{ \operatorname{grad}\left(\frac{n_1}{n}\right) + k_T \operatorname{grad}(\log T) \right\} ; \quad (1)$$

n is the overall number density (number of molecules per unit volume), n_1 and n_2 the partials number densities, D_{12} the binary diffusion coefficient. k_T the thermal diffusion ratio and T the absolute temperature.

Eq. (1) is only valid if the diffusion is purely thermal, i.e., in the absence of external forces and pressure gradients.

In order to determine $\bar{V}_1$ and $\bar{V}_2$ we use the fact that the total number of molecules crossing a fixed given surface per unit area and per unit time is a constant:

$$\sum_i n_i \bar{V}_i = C \, . \quad (2)$$

[1]) A. Langsdorf Jr., Rev. Sc. Instr. 10 (1939) 91.

[2]) C. Succi and G. Tagliaferri, Nuovo Cimento 9 (1952) 1092.

[3]) R. P. Shutt, Rev. Sc. Instr. 22 (1951) 730.

[4]) O. R. Frisch, Progress in Nuclear Physics Vol. 3 (Pergamon Press Ltd., 1953).

[5]) S. Chapman and T. G. Cowling, The Mathematical Theory of Non-Uniform Gases (Cambridge Univ. Press, 1953).

In this equation $\overline{V}_i$ is the mean absolute velocity of molecules of class i. In the case of a two-component system, eq. (2) becomes

$$n_1\overline{V}_1 + n_2\overline{V}_2 = C \,. \tag{3}$$

The physical meaning of C appears at once from the expressions of the two velocities. Combining (1) and (3), these are given by

$$\begin{aligned} \overline{V}_1 &= \frac{C}{n} - \left(\frac{n}{n_1}\right) D_{12}\left\{\operatorname{grad}\left(\frac{n_1}{n}\right) + k_T \operatorname{grad}(\log T)\right\} \\ \overline{V}_2 &= \frac{C}{n} - \left(\frac{n}{n_2}\right) D_{12}\left\{\operatorname{grad}\left(\frac{n_2}{n}\right) - k_T \operatorname{grad}(\log T)\right\} \,. \end{aligned} \tag{4}$$

The first term on the right-hand side of equation (4) represents a current common to the two materials. Thus it must be a convective term. We define the convection velocity ω as

$$\omega = \frac{C}{n} \,. \tag{5}$$

We shall show that eq. (5) coincides with the definition usually given to the convection velocity.

Let f_i be the mass flux of the i-component across a fixed surface. Then

$$f_i = n_i m_i \overline{V}_i$$

in which m_i is the mass of the molecules i. Introducing eq. (4)

$$\begin{aligned} f_1 &= \omega\,\rho_1 - nD_{12}\left\{\operatorname{grad}\left(\frac{\rho_1}{n}\right) + k_T m_1 \operatorname{grad}(\log T)\right\} \\ f_2 &= \omega\,\rho_2 - nD_{12}\left\{\operatorname{grad}\left(\frac{\rho_2}{n}\right) - k_T m_2 \operatorname{grad}(\log T)\right\} \,. \end{aligned} \tag{6}$$

From eq. (3) and the definitions for f_1 and f_2 we get

$$\omega = \frac{f_1}{nm_1} + \frac{f_2}{nm_2} \,. \tag{7}$$

If we suppose that the temperature is constant, eqs. (6) reduce to the well-known Fick's diffusion law in the corrected form to take into account the convection effect (Kuusinen[6])). It is interesting to note that the convective term appears in a natural way in the theory and it is not necessary to add it *a posteriori* as Kuusinen does.

[6]) K. Kuusinen, Ann. d. Physik **24** (1935) 445.

[7]) J. O. Hirschfelder, C. F. Curtiss and R. B. Bird, Molecular Theory of Gases and Liquids (John Wiley, 1954).

Finally, from (7) it is easy to show that for ideal gases is given by

$$\omega = f_1 v_1 + f_2 v_2$$

in which v_1 and v_2 are the specific volumes of each component. This expression is usually given for the convection velocity.

3. Application to the Diffusion Cloud Chamber

We shall apply the flux eqs. (6) obtained previously to the vapour component in a diffusion cloud chamber. On doing this we shall introduce some simplifications:

First we suppose that the side-wall effects are negligible, i.e. that the diffusion is only one-dimensional. Then, from eqs. (6) we get for the vapour flux:

$$f_1 = \omega\,\rho_1 - nD_{12}\{\partial(\rho_1/n)/\partial x + (k_T m_1/T)(\partial T/\partial x)\}. \tag{8}$$

Furthermore, the convection eq. (7) reduces to

$$\omega = \frac{f_1}{nm_1} \,, \tag{9}$$

as the flux of gas can be neglected with respect ot the flux of vapour.

The final form of the expression for the vapour flux is obtained after the substitution of ω in eq. (8), and by noticing that T is exclusively a function of x. We assume also that the total pressure in the chamber is constant, and thus $\partial n/\partial T \approx -n/T$. Finally, we notice that $n^2/n_2 \approx n$. Then we can write eq. (8) in the following way:

$$f^1 = -D_{12}\{\mathrm{d}(T\rho_1)/\mathrm{d}T + m_1 n\, k_T\}(1/T)(\mathrm{d}T/\mathrm{d}x) \,. \tag{10}$$

This expression describes the transport of vapour through the diffusion cloud chamber due to the existence of a temperature gradient.

Now we shall derive a differential equation which describes the change of vapour density with time. For that, we start with the continuity equation

$$\partial\rho_1/\partial t = -\operatorname{div} f_1 \,. \tag{11}$$

We write the exact expression (6) in the modified form

$$f_1 = -(n^2/n_2)\, D_{12} \operatorname{grad}(\rho_1/n) - (\rho/\rho_2)\, D_1{}^T \operatorname{grad}(\log T). \tag{12†}$$

† We have introduced here the binary thermal diffusion coefficient, $D_1{}^T$, by the equation $k_T = (\rho/n^2 m_1 m_2)(D_1{}^T/D_{12})$ in which ρ is the overall density of the mixture, and the coefficients k_T and D_{12} are defined in section 2. The definition of $D_1{}^T$ is according to Hirschfelder *et al.*[7]).

It can be shown that the approximated equation

$$\text{grad}\,(\rho_1/n) = (1/n)\,\text{grad}\,\rho_1 \qquad (13)$$

is valid even when the temperature is not constant, provided that n_1 is small compared to n^2 and that the rate of change with the temperature of the vapour number density $\mathrm{d}n_1/\mathrm{d}T$ is higher than that of the gas number density $\mathrm{d}n_2/\mathrm{d}T$.

The second term on the right-hand side of eq. (12) can be written approximately as *grad* $(D_1{}^T \log T)$, supposing that $D_1{}^T$ is independent of T and that ρ/ρ_2 is about equal to 1. The last assumption is clear as the vapour number density n_1 is small compared to the gas number density n_2.

Thus we write eq. (12) in the simplified form

$$f_1 \approx -D_{12}\,\text{grad}\,(\rho_1 + k'_T \log T) \qquad (14)$$

in which we have supposed D_{12} to be constant. Furthermore we have defined

$$k'_T \equiv D_1{}^T/D_{12} = (n^2 m_1 m_2/\rho)\,k_T\,. \qquad (14a)$$

Finally, by using the continuity eq. (11), we obtain the diffusion equation

$$\partial\rho_1/\partial T = D_{12}\,\nabla^2\,(\rho_1 + k'_T \log T)\,. \qquad (15)$$

4. Revision of the Theory of the Diffusion Cloud Chamber

4.1. EQUATIONS USED IN THE THEORY BY SHUTT

For the vapour flux through the chamber we have set up eq. (10). The corresponding equation used by Shutt is

$$f_1 = f_1\rho_1/\rho - D_{12}\,\mathrm{d}\rho_1/\mathrm{d}x\,. \qquad (16)$$

This is Fick's law, in the corrected form proposed by Kuusinen. But this law refers to diffusion under an isothermal equilibrium and, as the main physical fact in the diffusion cloud chamber is just the existence of a temperature gradient, it is not possible to use it, even as an approximation. Furthermore, the convective term $f_1\rho_1/\rho$ seems to be incorrect. By comparing it with the convective term defined by eqs. (8) and (9), it appears that it is valid only when the masses of the two kinds of molecules are the same. This condition obviously limits it to certain mixtures only.

In the same way, the diffusion equation used by Shutt,

$$\partial\rho_1/\partial t = D_{12}\,\nabla^2\rho_1 \qquad (17)$$

can be applied only when the temperature is constant. We have proposed instead an equation (eq. 15) that takes into account the existence of a temperature gradient.

4.2. CORRECTED EQUATION FOR THE TEMPERATURE GRADIENT

We shall now obtain an equation for the temperature gradient following the same treatment as given by Shutt, but using the equations obtained in section 3.

For the vapour flux we have eq. (10), namely:

$$f_1 = -D_{12}\,\{\mathrm{d}(T\rho_1)/\mathrm{d}T + nm_1k_T\}\,(1/T)\,(\mathrm{d}T/\mathrm{d}x)\,. \qquad (18)$$

Near a liquid drop, T and ρ_1 must depend only upon r, the distance from the drop. Shutt has shown that it is only intersting to consider the stationary solution of the differential equations that describe the temperature and vapour density distributions. So, we have for the temperature

$$\partial\,(r^2\partial T/\partial r)/\partial r = 0 \qquad (19)$$

and for the vapour density, according to eq. (15),

$$\partial\,\{r^2\partial\,(\rho_1 + k'_T \log T)/\partial r\}/\partial r = 0\,. \qquad (20)$$

For both equations we have the boundary conditions

$$\begin{aligned} r = r_0 \quad &, \quad T = T_\mathrm{d} \quad , \quad \rho_1 = \rho'_1(T_\mathrm{d}) \\ r = \infty \quad &, \quad T = T(x) \quad , \quad \rho_1 = \rho_1(x) \end{aligned} \qquad (21)$$

that is to say, at the surface of a drop ($r = r_0$, r_0 being the radius of the drop) the vapour density depends only on the vapour pressure of the liquid at the temperature of the drop (T_d), and far from the drop ($r \gg r_0$) ρ_1 and T are only functions of the height x.

Furthermore, at the surface of a drop,

$$(f_1)_{r=r_0} = (K/L)\,(\partial T/\partial r)_{r=r_0} \qquad (22)$$

in which K is the thermal conductivity and L the latent heat of the liquid. Integrating eq. (20) and by using eqs. (14) and (22), we get:

$$\Delta(T_d) = -(LD_{12}/K)\{\rho'_1(T_d) - \\ - \rho_1(x) + k'_T \log(T_d/T(x))\} \quad (23)$$

in which we have defined

$$\Delta(T_d) \equiv T_d - T(x) \ . \quad (24)$$

Applying Stokes' law to a drop falling under gravity we obtain

$$d(mv)/dt = -6\pi\mu r_0 v - mg \ . \quad (25)$$

Here m is the mass of a drop, $v = dx/dt$ its velocity, μ the viscosity coefficient and g the acceleration of gravity.

Shutt has shown that left-hand side of eq. (25) is negligible. Using the resulting equation and applying the continuity equation to the drop, it can be shown that,

$$(dm/dx) = (18\pi\mu/g\rho_d)(f_1)_{r=r_0} \quad (26)$$

ρ_d being the liquid density.

Now we integrate eq. (19) and use eqs. (22), (24) and (26). We obtain

$$d(m^{4/3})/dx = -\eta\Delta(T_d) \quad (27)$$

with

$$\eta = (18\mu K/Lg\rho_d^{2/3})(4\pi/3)^{4/3} \ . \quad (28)$$

In order to take into account the removal of vapour due to drop-wise condensation, we use the equation, proposed by Shutt,

$$df_1/dx = \int_x^{x_0}(dm(\xi, x)/dx)\, n(\xi)\, d\xi \\ + (dm(x_0, x)/dx)\int_{x_0}^{h} n'(\xi)\, d\xi \quad (29)$$

in which x_0 is the height in which condensation just begins, $m(\xi, x)$ the mass of a drop started at a height ξ and observed at x, $n(\xi)$ the number of condensation nuclei formed at ξ per unit volume and time, h the chamber height and $n'(\xi)$ the number of condensation formed in the region $x_0 \leqslant x \leqslant h$ that finally reaches the height $x = x_0$. Eq. (29) is valid in the region $0 \leqslant x \leqslant x_0$.

Finally, from eqs. (27), (29) and (18) we get, integrating by parts

$$-D_{12}\cdot x\cdot(\rho_1/T + d\rho_1/dT + nm_1k_T/T)(dT/dx) \\ = -\int_{T_0}^{T} D_{12}(\rho_1/T + d\rho_1/dT + nm_1k_T/T)\, dT \\ + \int_0^x x\,(d/dx)\left\{\int_x^{x_0}\left(\int_x^{\xi}\eta\Delta(T_d)\, dx\right)^{3/4} n(\xi)\, d\xi \right. \\ \left. + \left(\int_x^{x_0}\eta\Delta(T_d)\, dx\right)^{3/4}\int_{x_0}^{h} n'(\xi)\, d\xi\right\} dx \ . \quad (30)$$

This equation is valid only in the region $0 \leqslant x \leqslant x_0$. In the region $x_0 \leqslant x \leqslant h$, $df_1/dx = 0$ and the vapour flux is constant.

5. Comparison with Shutt's Theory

Eq. (30) can be compared directly with Shutt's equation, namely,

$$-[xD_{12}/(1 - \rho_1/\rho)]\,(d\rho_1/dT)\,(dT/dx) \\ = -\int_{T_0}^{T}[D_{12}/(1 - \rho_1/\rho)]\,(d\rho_1/dT)\, dT \\ + \int_0^x x\,(d/dx)\left\{\int_x^{x_0}\left(\int_x^{\xi}\eta\Delta\, T_d\, dx\right)^{3/4} n(\xi)\, d\xi \right. \\ \left. + \left(\int_x^{x_0}\eta\Delta\, T_d\, dx\right)^{3/4}\int_{x_0}^{h} n'(\xi)\, d\xi\right\} dx \quad (31)$$

in which ρ is the overall density of the mixture.

As $\rho_1 \ll \rho$, $(1 - \rho_1/\rho) \approx 1$ and the difference between the left-hand sides and the first term of the right-hand sides of eqs. (31) and (30) are the terms $\rho_1/T + nm_1k_T/T$ appearing in the latter. The term nm_1k_T/T probably can always be neglected, due to the fact that k_T is normally small. ρ_1/T will be considered later. The second terms of the right-hand side of both equations are also different, because $\Delta(T_d)$ (eq. (30)) is different from ΔT_d (eq. (31)). $\Delta(T_d)$ is given by eqs. (23) and (24), and ΔT_d is given by

$$\Delta T_d \equiv T_d - T(x) = -[LD_{12}/K\,(1 - \rho_1/\rho)_{r=r_0}] \\ \times [\rho'_1(T_d) - \rho_1(x)] \ . \quad (32)$$

By comparing eqs. (23) and (32) we see that, apart from the factor $(1 - \rho_1/\rho)_{r=r_0}$ which we have just discussed, both differ in the term $k'_T \log T_d/T(x)$ which appears in the former. Nevertheless, this term also is expected to be small, due to the logarithmic factor and because k'_T, as defined in eq. (14a), must be small.

The main difference between eqs. (30) and (31) is then due to the term ρ_1/T. In general little can be said about this term, because of the very different dependences of the vapour pressure with the temperatures for different sources of vapour.

Following Shutt, we write for the vapour density

$$\rho_1 = (M/RT)\cdot p \quad (33)$$

in which p is given by Thompson's formula

$$p = p'(T)\exp\{(M/RT\,\rho_d)(3/2)(4\pi\sigma^4\epsilon/e^2)^{1/3}\}, \quad (34)$$

σ being the surface tension and ε the dielectric constant of the liquid, e being the electron charge; $p'(T)$ is the vapour pressure and is given by Clapeyron's equation, namely

$$p'(T) = \exp\{B + (M/R) \int (L/T^2)\, \mathrm{d}T\} . \quad (35)$$

In eq. (35) we have preferred to take into account the temperature dependence of the latent heat† L. Finally, we get for the vapour density

$$\rho_l = (M/RT) \exp\{B + (M/RT\rho_d)\ (3/2)\ (4\pi\sigma^4\varepsilon/e^2)^{1/3} + (M/R) \int (L/T^2)\, \mathrm{d}T\} . \quad (36)$$

In order to compare eqs. (30) and (31) we consider

$$\rho_l/T + \mathrm{d}\rho_l/\mathrm{d}T = (\mathrm{d}\rho_l/\mathrm{d}T)\{(A - C)/(A - C - T)\} \quad (37)$$

† Shutt uses instead $p'(T) = \exp(B - E/T)$, E being a constant.

with $$A = ML/R$$

and $$C = (M/R\rho_d)\ (3/2)\ (4\pi\sigma^4\varepsilon/e^2)^{1/3} .$$

In rough calculations we have applied eq. (37) to the cases of methyl and ethyl alcohol[8]). For the methyl alcohol, A turns out to be big as compared with C and an average T, and so the correction is negligible. For ethyl alcohol, A is small as compared with C, and the corrective factor is of the order of 50%.

I wish to express my thanks to Professor A. Arias at the University of Chile for stimulating discussions, and to Professor L. Rosenfeld for his interest in this work and for giving me the possibility to pursue my studies at Manchester University. I also should like to thank the British Council for awarding me a scholarship.

[8]) International Critical Tables.

NUCLEAR INSTRUMENTS 3 (1958) 90–96; NORTH-HOLLAND PUBLISHING CO. – AMSTERDAM

RELATIVISTIC THEORY OF THE SPHERICAL ELECTROSTATIC ANALYZER

NEIL ASHBY†

Harvard University, Cambridge, Mass.

Received 24 February 1958

A general relativistic analysis of the properties of spherical electrostatic analyzers is presented, and applied to some special cases of interest. An important limitation on the allowable kinetic energies is shown to exist: for energies greater than a certain kinetic energy T_{max}, the spherical analyzer is not an effective focusing instrument. Expressions for the velocity and energy dispersions, and for the resolving power, are derived. A special case, in which the central angle of the analyzer is greater than $3\pi/2$, and which has desirable focusing properties, is briefly discussed.

1. Introduction

The possibility of using a sector of a spherical condenser as a focusing energy analyzer was first pointed out by Aston[1]). As in fig. 1, the instrument consists of two concentric spherical segments to which is applied a potential difference V_f, giving rise effectively to a Coulomb field between the plates. Charged particles emitted from a point A on the symmetry axis are deflected by the field and, in the low-energy limit, are brought to a focus at a point F on the axis.

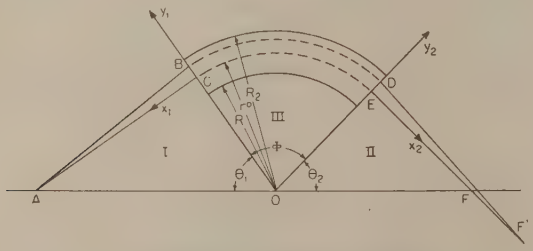

Fig. 1. Spherical Electrostatic Analyzer.

The theory for the extreme non-relativistic case has been given by Purcell[2]), who showed that the position of the focal point F is, to first order, independent of the direction in which particles are emitted. It is therefore possible to construct an instrument of very large useful aperture and high resolution. Several such instruments have been constructed, principally for use at relatively low kinetic energies[2,3]).

Recent experiments on β-decay in aligned nuclei have led to renewed interest in the spherical electrostatic analyzer as a means of obtaining concentrated beams of polarized electrons. The kinetic energies involved in such experiments, however, are comparable to the rest energies of the particles, and the effects of the relativity corrections become quite important. It is the object of this paper to present a detailed relativistic analysis of the focusing properties of the spherical analyzer.

2. Equations of Motion

We shall begin by solving the relativistic equations of motion for a charged particle in a Coulomb field, with arbitrary initial conditions. The results will then be applied to a variety of special cases.

The analyzer may be pictured as being generated by the rotation of the circular segments of radii R_1, R_2 in fig. 1, about the axis AOF. Let a potential difference V_f be established between these two concentric spherical sectors. This gives rise to an electric field which is assumed to fall off strictly as $1/r^2$ between the plates and which

† National Science Foundation Predoctoral Fellow, Harvard University.

[1]) F. W. Aston, Phil. Mag. 38 (1919) 710.
[2]) E. M. Purcell, Phys. Rev. 54 (1938) 818.
[3]) Brown, Craig and Williamson, Rev. Sci. Inst. 22 (1951) 952.

ends abruptly at the edges of the sectors; that is, the electric field vanishes for $\theta < 0$, $\theta > \Phi$. Here, θ is the polar angle measured from OC. In practice, one attempts to eliminate the effect of the fringing field by placing shields near the edges of the condenser. Herzog[4]) has shown how this is done quite accurately for the fringing field of a plane parallel-plate condenser; we shall follow the customary treatment in assuming that this is also possible for the spherical condenser.

Choosing the potential to be zero at a distance $r = r^0$ from O, with $R_1 < r^0 < R_2$, the potential is given by

$$V(r) = -\frac{V_f R_1 R_2}{R_2 - R_1}\left(\frac{1}{r} - \frac{1}{r^0}\right) \tag{1}$$

the potential difference between the plates being

$$V_f = V(R_2) - V(R_1) \ . \tag{2}$$

The force on a particle of charge q is directed radially inward, and has the magnitude

$$f = |\, q\varepsilon \,| = \frac{qV_f R_1 R_2}{R_2 - R_1}\cdot\frac{1}{r^2} \equiv \frac{k_1}{r^2} \tag{3}$$

where k_1 is a positive constant. The value of k_1 will later be fixed by the energy of the particles which are being focussed:

$$k_1 = \frac{qV_f R_1 R_2}{R_2 - R_1} > 0 \ . \tag{4}$$

Since only radial forces act, a particle will remain in the azimuthal plane $\varphi = \varphi_0$ into which it is emitted. Therefore, by symmetry, we need consider only the paths of particles in one plane φ_0. The radial equation of motion is

$$\frac{\mathrm{d}}{\mathrm{d}t}(m\dot{r}) = mr\omega^2 - f \tag{5}$$

where $\dot{\theta} = \omega$ is the angular velocity. Another consequence of the fact that the force is entirely radial is that angular momentum must be conserved:

$$\frac{\mathrm{d}}{\mathrm{d}t}(mr^2\omega) = 0 \ . \tag{6}$$

Finally, the law of conservation of energy gives

$$\frac{\mathrm{d}}{\mathrm{d}t}(mc^2) = -f\dot{r} = -\frac{k_1\dot{r}}{r^2} \ . \tag{7}$$

[4]) R. Herzog, Z. f. Physik 97 (1935) 596.

The latter equation may be solved immediately:

$$mc^2 = \frac{k_1}{r} + k_2 \tag{8}$$

where k_2 is a constant of integration. The angular momentum eq. (6) yields

$$mr^2\omega = k_3 \tag{9}$$

where k_3 is the angular momentum taken with respect to the point O.

The radial equation may now be solved by means of the substitution $u = 1/r$, for by using eq. (9) we have that $m\dot{r} = -k_3\mathrm{d}u/\mathrm{d}\theta$ so the radial equation becomes

$$\frac{\mathrm{d}^2u}{\mathrm{d}\theta^2} + u = \frac{k_1 m}{k_3^2} = \frac{k_1^2 u}{c^2 k_3^2} + \frac{k_1 k_2}{c^2 k_3^2} \ . \tag{10}$$

Putting

$$\Gamma = (1 - k_1^2/c^2k_3^2)^{-1/2} \tag{11}$$

$$A = \frac{k_1 k_2}{c^2 k_3^2}\Gamma^2 \tag{12}$$

we obtain a solution in the form

$$u = 1/r = A + A_1\cos(\theta/\Gamma) + A_2\sin(\theta/\Gamma) \ . \tag{13}$$

A_1, A_2 are integration constants whose values are fixed by the initial conditions on r, $\dot{r}$, θ and $\dot{\theta}$. The appearance of the factor $1/\Gamma$ in the arguments of the above solution is the principal source of relativistic corrections to the classical theory. It gives rise to effects which correspond to precession of the elliptical orbits of particles moving in a Coulomb field; in the low-energy limit, Γ reduces to unity. However, as will be seen, Γ increases with increasing energy and strongly affects the focusing properties of the condenser.

Referring to fig. 1, we suppose that particles of energy

$$E^0 = m^0c^2 = \frac{m_0c^2}{\sqrt{1 - (\beta^0)^2}} \equiv \gamma m_0c^2 \tag{14}$$

pass from the source A to C where they enter the field; within the field, the path is circular with radius $r = r^0$, and after passing out of the field at E, the path crosses the axis at F. The fact that particles of this particular energy stay in a circular orbit fixes the value of V_f (i.e., k_1), for from eq. (5), if there is no radial velocity we have

$$\frac{\mathrm{d}}{\mathrm{d}t}(m^0\dot{r}^0) = 0 = m^0r^0(\omega^0)^2 - k_1/(r^0)^2 \tag{15}$$

so that $$k_1 = m^0\gamma^0(v^0)^2 \tag{16}$$

where $v^0 = \beta^0 c = \omega^0\gamma^0$ is the velocity.

Before proceeding, a few comments about notation are appropriate: in general, the path ACEF, which we refer to as the "normal path", is described by symbols having superscript 0 (E^0, β^0, etc.). A path differing slightly from ACEF is described in regions I and II by symbols without superscripts or primes (E, β, $\cdots$), and in region III by primed symbols (E', β', $\cdots$). The constants Γ, A, A_1, A_2, k_2, k_3 are left unprimed.

Now consider a path ABDF which deviates slightly from the normal path ACEF as follows: let a particle have initial position $r' = r^0(1 + \alpha')$ $\theta' = 0$ at the edge of the field, and let its velocities in the r and θ directions be v'_r, v'_θ respectively, at this point. If then the relativistic mass of the particle is determined by the formula

$$m'c^2 = m^0c^2\,(1 + \Delta') = \frac{m_0c^2}{\sqrt{1 - (\beta')^2}} \tag{17}$$

where Δ' is small, and where the velocity of the particle is

$$\beta' = v'/c = \frac{1}{c}\,(v'_r{}^2 + v'_\theta{}^2)^{1/2} \tag{18}$$

then one can easily show that

$$v' = v^0\,(1 + \Delta')^{-1}\left(1 + \frac{\Delta'(\Delta' + 2)}{(\beta^0)^2}\right)^{1/2}. \tag{19}$$

This enables us to find k_3, for from eqs. (9), (18) and (19),

$$\begin{aligned} k_3 &= m'r^0\,(1 + \alpha')\,v'_\theta = m^0r^0\,(1 + \alpha')\,v^0 \\ &\times [1 + (\beta^0)^{-2}\,\Delta'\,(\Delta' + 2)]^{1/2}\,(1 + \varepsilon'^2)^{-\frac{1}{2}} \end{aligned} \tag{20}$$

where we have put $\varepsilon' = v'_r/v'_\theta$. The constant k_2 may be found from the energy equation (8):

$$m'c^2 = \frac{k_1}{r^0\,(1 + \alpha')} + k_2 = \frac{m^0\,(v^0)^2}{1 + \alpha'} + k_2 \tag{21}$$

and therefore

$$k_2 = \frac{m^0c^2}{1 + \alpha'}\,[(1 + \alpha')\,(1 + \Delta') - (\beta^0)^2]\,. \tag{22}$$

A and Γ may be evaluated from the definitions. We find

$$\Gamma = \left[1 - \frac{(1 + \varepsilon'^2)\,(\beta^0)^2}{(1 + \alpha')^2\,[1 + (\beta^0)^{-2}\,\Delta'\,(\Delta' + 2)]}\right]^{-1/2} \tag{23}$$

$$A = \frac{(1 + \varepsilon'^2)\,[(1 + \alpha')\,(1 + \Delta') - (\beta^0)^2]}{r^0\,(1 + \alpha')^3\,[1 + (\beta^0)^{-2}\,\Delta'\,(\Delta' + 2)]}\,\Gamma^2\,. \tag{24}$$

Finally, we have to determine A_1 and A_2. From the condition that $r' = r^0(1 + \alpha')$ at $\theta' = 0$ we have

$$\frac{1}{r^0\,(1 + \alpha')} = A + A_1 \tag{25}$$

and $\dot{r}' = v'_r$ at $\theta' = 0$ gives:

$$\dot{u}' = -\frac{v'_r}{(r^0)^2\,(1 + \alpha')^2} = \frac{A_2\dot{\theta}'}{\Gamma} = \frac{A_2v'_\theta}{\Gamma r^0\,(1 + \alpha')} \tag{26}$$

or, solving for A_2 and using the definition of ε',

$$A_2 = -\frac{\Gamma\varepsilon'}{r^0\,(1 + \alpha')}\,. \tag{27}$$

Thus, the solution of the radial equation of motion becomes:

$$\begin{aligned} \frac{1}{r'} = A\,[1 - \cos(\theta'/\Gamma)] + \frac{1}{r^0\,(1 + \alpha')}\cos(\theta'/\Gamma) - \\ - \frac{\Gamma\varepsilon'}{r^0\,(1 + \alpha')}\sin(\theta'/\Gamma)\,. \end{aligned} \tag{28}$$

This is exact. Although it is complicated, it is expressed only in terms of parameters describing the normal path (β^0, r^0), and parameters (α', Δ', ε') which are for our purposes small. Thus, we may easily investigate small deviations from the normal path by making approximations in (28).

3. Particle Trajectories

Up to this point we have discussed only the motion inside the field. To describe the motion in regions I and II, let coordinate systems (x_1, y_1), (x_2, y_2) be set up as indicated in fig. 1, with origins at C and E, respectively. The source is taken to be at the point A, a distance $p^0 = r^0 \sec\theta_1$ from O. The effects of finite source size may be partially included in the analysis by supposing the source to have finite extension along the axis OA. Thus, let a particle be emitted from a point on the axis a distance

$$p = p^0\,(1 + \alpha) \tag{29}$$

from O, with velocities v_r, v_θ, in the $+y_1$, $-x_1$ directions. Let its energy be

$$E = m^0c^2\,(1 + \Delta) = mc^2\,. \tag{30}$$

It will travel in the field-free region with constant velocity, till it intersects the edge of the field at C. In region I, then, the equation of the path will be

$$\frac{y_1 - p^0\alpha\cos\theta_1}{x_1 - p^0(1+\alpha)\sin\theta_1} = -\varepsilon \tag{31}$$

where we have put

$$\varepsilon = v_r/v_\theta . \tag{32}$$

Here, Δ measures a small fractional spread in the energies of the emitted particles; for a monoenergetic source, $\Delta = 0$. ε gives a measure of the spread in directions of the velocities.

To find α', note that putting $x_1 = 0$ in eq. (31) gives y_1 as the distance $r^0\alpha'$ from C, so

$$y_1|_{x_1=0} = r^0\alpha' = \varepsilon\, p^0(1+\alpha)\sin\theta_1 + p^0\alpha\cos\theta_1$$

which gives

$$\alpha' = \alpha + \varepsilon(1+\alpha)\tan\theta_1 . \tag{33}$$

To obtain the connection between Δ and Δ', it is necessary to apply a small correction to the energy as the particle passes into the field at B. Since the field is electrostatic, the sum of potential and kinetic energies must remain constant. However, we are treating the electric field as though it ended abruptly at the edge of the condenser, and in such a field energy is not conserved. To correct for this, we allow the kinetic energy to change discontinuously at B. Outside the field, the total energy is given by eq. (30), and this must be equal to the kinetic plus rest plus potential energies just inside the field, which gives

$$E = E' = m^0c^2(1+\Delta') - \frac{k_1}{r^0(1+\alpha')} + \frac{k_1}{r^0} \tag{34}$$

and solving for Δ', we obtain

$$\Delta' = \Delta - (\beta^0)^2\frac{\alpha + \varepsilon(1+\alpha)\tan\theta_1}{1+\alpha+\varepsilon(1+\alpha)\tan\theta_1} . \tag{35}$$

Lastly, we need the relation between ε and ε'. Having entered the field, the energy correction must appear as a change in the angular velocity, while the radial velocity remains the same. This is because we have effectively neglected components of the electric field normal to the radius. Also, it corresponds to the fact that, in optics, when a beam of waves passes through a boundary between two media of different refraction indices, normal components of the velocity are changed while tangential components are not. Thus, at B, $v_r = v'_r$ and

$$\varepsilon' = \frac{v'_r}{v'_\theta} = \frac{v_r}{v_\theta}\frac{v_\theta}{v'_\theta} = \varepsilon\frac{\beta^0}{\beta'}\sqrt{\frac{1+\varepsilon'^2}{1+\varepsilon^2}} \tag{36}$$

where the ratio β^0/β' may be obtained from the identity:

$$m^0c^2(1+\Delta') = \frac{m_0c^2(1+\Delta')}{\sqrt{1-(\beta^0)^2}} = \frac{m_0c^2}{\sqrt{1-(\beta^0)^2}} . \tag{37}$$

Introducing the abbreviation δ_1 such that eq. (36) takes the form

$$\varepsilon' = \varepsilon\delta_1 \tag{38}$$

then δ_1 will differ from unity by infinitesimals of first order in α, Δ and ε.

Thus, under the assumed conditions, eqs. (33), (35), and (38) upon substitution into (23)–(24) and thence into (28) give us the path in III. We have yet to connect this to the path in region II. At D, the distance from E is $y_2 = r'_f - r^0$, where the subscript f hereafter refers to quantities evaluated just inside the field at D. If the equation of the path in II is

$$y_2 = mx_2 + b \tag{39}$$

we have

$$b = r'_f - r^0 . \tag{40}$$

To find m, note that $m = \dot{y}_2/\dot{x}_2$ evaluated just outside the field. We again have to match boundary conditions on the velocities. If $\varepsilon'_f = (v'_r/v'_\theta)_f$, then by virtue of the reversibility of the motion of charged particles in an electrostatic field, we must have an equation similar to eq. (36):

$$\varepsilon'_f = m\sqrt{\frac{1+\varepsilon'^2_f}{1+m^2}}\frac{\beta^0}{\beta'_f} \tag{41}$$

where $c\beta'_f$ is the velocity evaluated at $\theta = \Phi$. We abbreviate this by putting

$$m = \delta_2\varepsilon'_f \tag{42}$$

where δ_2 differs very little from unity. To evaluate δ_2, we first define a quantity Δ'_f by means of

$$m^0c^2(1+\Delta') + V(r^0[1+\alpha']) = m^0c^2(1+\Delta'_f) + V(r'_f)$$

and solving for Δ'_f,

$$\Delta'_f = \Delta' + (\beta^0)^2 r^0\left(\frac{1}{r'_f} - \frac{1}{r^0(1+\alpha')}\right) . \tag{43}$$

Then from the identity

$$m^0c^2(1+\Delta'_f) = \frac{m_0c^2(1+\Delta'_f)}{\sqrt{1-(\beta^0)^2}} = \frac{m_0c^2}{\sqrt{1-(\beta'_f)^2}} \tag{44}$$

the ratio β^0/β'_f may be obtained. These equations

allow us to determine δ_2 to any desired degree of accuracy. Both of the quantities δ_1, δ_2 are, for our purposes, important only to first order in ε, in the special case $\alpha = \Delta = 0$. For later reference, we give here the results for this case:

$$\delta_1 = 1 + \varepsilon\,(1 - (\beta^0)^2)\tan\theta_1 + \cdots \tag{45}$$

$$\delta_2 = 1 - \varepsilon\,(1 - (\beta^0)^2)\,[\tan\theta_1 \cos(\Phi/\gamma) + \gamma \sin(\Phi/\gamma)] + \cdots \tag{46}$$

where $\gamma = [1 - (\beta^0)^2]^{-1/2}$. Returning now to the evaluation of m, we have

$$m = \delta_2 (v'_r/v'_\theta)_f = \delta_2 \left(\frac{\dot{r}'}{r'\dot{\theta}'}\right)_f = -\delta_2 r'_f \left[\frac{\mathrm{d}}{\mathrm{d}\theta'}\left(\frac{1}{r'}\right)\right]_f . \tag{47}$$

The final result is the equation of the path in region II:

$$y_2 = \frac{1 - \delta_2 x_2 \{ A\Gamma^{-1}\sin(\Phi/\Gamma) - A\,[1 - \cos(\Phi/\Gamma)] + \dfrac{\Gamma^{-1}}{r^0(1+\alpha')}\sin(\Phi/\Gamma) - \dfrac{\varepsilon'\cos(\Phi/\Gamma)}{r^0(1+\alpha')}\}}{\dfrac{1}{r^0(1+\alpha')}\cos(\Phi/\Gamma) - \dfrac{\Gamma\,\varepsilon'\sin(\Phi/\Gamma)}{r^0(1+\alpha')}} - r^0 . \tag{48}$$

4. Focusing Properties

The above equation contains all the information necessary to investigate fully the properties of the condenser. In this section we will not be concerned with the effects of source size, so hereafter we set $\alpha = 0$. A qualitative picture of the focusing characteristics may now be obtained as follows: let the angles θ_1, θ_2 reduce to zero. Then the particles always move in a pure Coulomb field, and for a monoenergetic source, the solution (28) reduces to:

$$\frac{1}{r} = \frac{1}{r^0}\,[1 - \varepsilon\gamma \sin(\theta/\gamma)] \tag{49}$$

where we have kept only the first-order term in ε. In this example, the "focus" should be at the point for which r is independent of ε, to first order; thus, the coefficient of ε in the above equation must vanish. This will be true if

$$\theta = \gamma\pi = \pi + \pi\frac{T}{m_0c^2} \tag{50}$$

where T is the kinetic energy. Thus the focus F' falls on the axis only in the exact low-energy limit, $T \to 0$. The central angle by which it misses the axis is proportional to the kinetic energy, and as $T \to m_0c^2$, F′ approaches the source again. Hence, there is an upper limit to the kinetic energy for which focusing may conveniently be obtained. In this case, it is $T_{\max} = m_0c^2$.

By virtue of the axial symmetry, the locus of points F′ form a ring about the axis, which we shall refer to as the *ring focus*. In addition to this, there is a focal point F on the axis; all particles pass near F, independently of the plane $\varphi = \varphi_0$ into which they are emitted.

To find the position of the focus in the general case, the distance $x_{F'}$ from E to the ring focus will be determined by the fact that at F′, y_2 is independent of the parameter ε to first order. This is expressed by evaluating

$$\left.\frac{\partial y_2}{\partial \varepsilon}\right|_{\varepsilon = 0} = 0 \tag{51}$$

and solving for x_2. If for example one were interested in use of this instrument as an energy analyzer, after solving eq. (51) for a particular Δ, one would substitute the result $x_2 = x_{F'}$ back into eq. (48), thus obtaining a parametric representation of the position of F′ in the (x_2, y_2) coordinate system, in terms of Δ. This procedure is quite general and gives the position of the ring focus for any value of Δ and α, although when Δ and α are not small the necessary calculations become very laborious.

We shall consider in detail only the simplest case, $\alpha = \Delta = 0$. Application of the above procedure yields in a straightforward way the result:

$$x_{F'} = r^0 \frac{\tan\theta_1 \cos(\Phi/\gamma) + \gamma \sin(\Phi/\gamma)}{\gamma^{-1}\tan\theta_1 \sin(\Phi/\gamma) - \cos(\Phi/\gamma)} . \tag{52}$$

Defining an angle θ'_1 such that

$$\tan\theta'_1 = \gamma^{-1}\tan\theta_1 \tag{53}$$

we can put eq. (52) in the form

$$x_{F'} = -\gamma r^0 \tan(\Phi/\gamma + \theta'_1) . \tag{54}$$

For a given Φ and θ_1, this is a monotonically increasing function of γ. Its minimum value occurs for $\gamma = 1$—the extreme non-relativistic limit—and coincides with the point F, since

$\Phi + \theta_1 = \pi - \theta_2$ and then $x_{F'} = r^0 \tan \theta_2$. For small kinetic energies, the distance of the ring focus from F is proportional to the kinetic energy:

$$x_{F'} = r^0 \tan \theta_2 + \frac{T}{m_0 c^2} r^0 \left\{ \tan \theta_2 + \right.$$

$$\left. + \left(\Phi + \frac{1}{2} \sin 2\theta_1 \right) \sec^2 \theta_2 \right\} + \cdots . \qquad (55)$$

From the form of eq. (54), it is evident that $x_{F'}$ is a rapidly increasing function of energy. In fact, $x_{F'} \to \infty$ when the argument of the tangent approaches $\pi/2$. This sets an upper limit on the energy for which a ring focus may exist; for energies greater than this maximum, the beam emerging into region II from the condenser will be divergent.

$\varepsilon = 0$, $x_2 = x_{F'}$. A convenient measure of the energy dispersion is denoted by D'_E and is defined as the beam width at the focus due to a fractional dispersion in energy Δ at the source, divided by Δ. We find:

$$D'_E = r^0 \left(\frac{\gamma^4 + 1}{\gamma^2 - 1} \right)$$

$$\times \left[1 - \gamma \tan (\Phi/\gamma + \theta'_1) \sin (\Phi/\gamma) - \cos (\Phi/\gamma) \right] . \qquad (57)$$

From this one may obtain the velocity dispersion, D'_β, at the ring focus by noting that if Δ_β is the fractional dispersion in velocity which corresponds to Δ, then

$$\Delta = (\gamma^2 - 1) \Delta_\beta \qquad (58)$$

so that $D'_\beta = r^0 (\gamma^4 + 1) [1 - \gamma \tan (\Phi/\gamma + \theta'_1)$

$$\times \sin (\Phi/\gamma) - \cos (\Phi/\gamma)] . \qquad (59)$$

TABLE I

Maximum kinetic energies in units of $m_0 c^2$

θ_1 \ Φ	30°	45°	60°	75°	90°	105°	120°	135°	150°	165°	180°
0°	—	—	—	—	0	0.17	0.33	0.50	0.67	0.83	1.00
15°	—	—	—	0	0.17	0.33	0.50	0.67	0.84	1.00	—
30°	—	—	0	0.17	0.35	0.52	0.69	0.86	1.02	—	—
45°	—	0	0.20	0.38	0.57	0.74	0.92	1.09	—	—	—
60°	0	0.25	0.48	0.69	0.89	1.09	1.28	—	—	—	—
75°	0.43	0.77	1.07	1.34	1.59	1.83	—	—	—	—	—

The value of this maximum energy is then found by solving the transcendental equation

$$\Phi/\gamma + \tan^{-1} \left[\frac{1}{\gamma} \tan \theta_1 \right] = \frac{\pi}{2} . \qquad (56)$$

These results are tabulated in table 1, for various values of θ_1 and Φ. For relativistic electrons, these maximum energies appear to be rather low, although for alpha particles, this would not be a very important limitation.

It is to be expected that the relativistic effects will cause a deterioration of the resolving power of the instrument. This may easily be investigated using eq. (48): suppose there is a point source at A which emits particles in the $-x_1$ direction, with an energy parameter $\Delta \neq 0$. After passing thru the condenser, the beam will have a finite spread which may be found from eq. (48) by substituting $\alpha = 0$,

At the ring focus, following Purcell[2]) we define a resolving power, or reduced dispersion, D, as the energy (or velocity) dispersion divided by the residual beam width due to the spread in directions of the velocities of the emitted particles, which is of order ε^2. To find this residual beam width, we have to carry out an expansion of y_2, evaluated at the point $x_2 = x_{F'}$, to second order in ε. Calling this width $W_{F'}$, the result is:

$$W_{F'} = r^0 \varepsilon^2 \{ \cos^2 (\Phi/\gamma) [\tan \theta'_1 + \tan (\Phi/\gamma)]^2 +$$

$$+ (1 - \tan^2 \theta_1) \gamma^2 [\cos (\Phi/\gamma) + \sin (\Phi/\gamma) \tan (\Phi/\gamma + \theta'_1)] -$$

$$- \gamma^2 + \left(1 - \frac{1}{\gamma^2} \right) [\gamma^2 \tan^2 \theta_1 + \gamma \tan (\Phi/\gamma + \theta'_1)$$

$$\times \tan \theta_1 \cos (\Phi/\gamma)] - \left(\gamma - \frac{1}{\gamma} \right) \sin (\Phi/\gamma) \tan \theta_1 \Big\} \qquad (60)$$

and the resolving power is then

$$D' = \frac{D'_E \text{ or } D'_\beta}{W_{F'}} . \qquad (61)$$

Even though the point F is not a focal point of high resolution, one may be interested in the dispersion at this point because of the very large effective aperture which is available. In that case, one obtains the velocity dispersion

$$D_\beta = r^0 (\gamma^4 + 1) \left[\frac{1}{\gamma} \tan \theta_2 \sin (\Phi/\gamma) - \cos (\Phi/\gamma) + 1\right]. \tag{62}$$

To get the resolving power, the width of the trace to first order in ε is

$$W_F = r^0 \varepsilon \cos (\Phi/\gamma) \left[\tan \theta_1 + \tan \theta_2 + \right.$$
$$\left. + \tan (\Phi/\gamma) \left(\gamma - \frac{1}{\gamma} \tan \theta_1 \tan \theta_2\right)\right] . \tag{63}$$

5. Special Case: $\Phi = 270^0 + \phi$

It is interesting to consider the geometry of fig. 2, in which the central angle Φ of the condenser is greater than 270°. Such an instrument would have several advantages, in spite of the physical difficulties involved in its construction. The ranges of allowable energies which are useful for applications are greatly extended, although there are still limitations on the maximum energies.

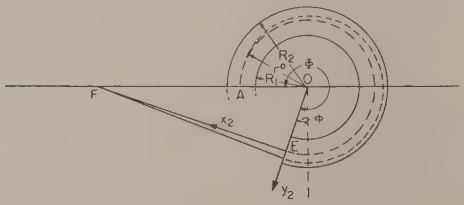

Fig. 2. Analyzer with central angle $\Phi = (3\pi/2) + \phi$.

The principal advantage is, that for each given central angle Φ, there exists one energy for which the ring focus falls exactly at the point F on the axis, behind the source. To see this comes about, let a point source be placed in the field at A. The particles travel around the origin, emerging from the field at the angle $\Phi = (3\pi/2) + \phi$. For such a case, we may still use the expression (54) to find the ring focus. It will be at

$$x_{F'} = -r^0 \gamma \tan \left[\left(\frac{3\pi}{2} + \phi\right) \cdot \frac{1}{\gamma}\right] . \tag{64}$$

The condition for the existence of a ring focus is $0 < x_{F'} < \infty$ and this leads to the condition

$$\frac{1}{2} + \frac{\phi}{\pi} < \frac{T}{m_0 c^2} < 2 + \frac{2\phi}{\pi} . \tag{65}$$

Thus, one may extend the range of energies for which focusing is possible by allowing the particles to remain in the field over a greater portion of their path.

If it is possible to choose γ so that $x_{F'} = r^0 \cot \phi$, then the ring focus will fall on the axis. This energy is determined by solution of the transcendental equation

$$-\gamma r^0 \tan \left[\frac{1}{\gamma}\left(\frac{3\pi}{2} + \phi\right)\right] = r^0 \cos \phi . \tag{66}$$

The results are given in table 2.

TABLE 2

$\Phi = 270° + \phi$. Kinetic energies for which ring focus falls on the axis, in units of m/c^2

ϕ	20°	30°	45°	60°	75°
T/m_0c^2	1.22	1.13	1.05	1.01	0.92

6. Conclusion

A general method of analyzing the spherical electrostatic condenser in the relativistic case has been developed and applied to some special cases of interest. An important limitation on the allowable kinetic energies has been shown to exist. Apart from our approximate treatment of the fringing field, the method of analysis is capable of great accuracy. Further improvements in the theory may be made by a more refined treatment of fringing effects.

7. Acknowledgement

The author is very grateful to Prof. K. T. Bainbridge, who suggested this problem, for a great deal of advice and encouragement, and for many valuable discussions.

NUCLEAR INSTRUMENTS 3 (1958) 97–103; NORTH-HOLLAND PUBLISHING CO. – AMSTERDAM

DAS ENTKOPPLUNGSGLIED IN DER Hf-TRANSMISSIONSLINIE EINES MIKROTRONS

H. REICH

Physikalisch-Technischen Bundesanstalt, Braunschweig

Received 17 February 1958

Three types of decoupling elements in the transmission line between magnetron and resonator of a microtron are investigated with respect to their power consumption and efficiency: a shunt resistance, an attenuator pad and a ferrite isolator ("Uniline" type S 161 of the firm Cascade Research/USA).

The equations governing the VSWR and the power distribution ratios resonator/load are derived and compared with measurements.

It is shown, that the shunt resistance rules out the attenuator. The uniline type used here does not give a better power efficiency than the shunt resistance. There only remain the other advantages of a ferrite isolator: ease of installation, uncritical setting of the phase shifter, and better isolation of the magnetron in the case of flash-over.

Zum frequenzstabilen Betrieb eines magnetronerregten Resonators mit hohem Q-Wert muss die Transmissionslinie ein Entkopplungs- oder Dämpfungsglied enthalten. Es gibt hierfür verschiedene Ausführungsarten, die sich in ihren physikalischen Eigenschaften stark unterscheiden. Bei der Erprobung der Resonatorkammer des 5 MeV-PTB-Mikrotrons wurden drei Typen näher untersucht: ein Parallelwiderstand, ein Abschwächer und ein Ferritisolator, die Uniline-Type S 161 der Firma Cascade Research/USA.

1. Theorie

Das ungefähre Verhalten der verschiedenen Entkopplungsglieder lässt sich aus den vereinfachenden Schaltbildern der Abbildungen 1 und

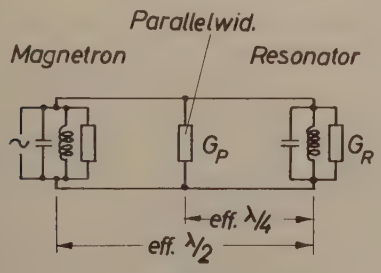

Abb. 1. Ersatzschaltbild beim Parallelwiderstand.

2 nach den Regeln der Hochfrequenztechnik ablesen. Es werden folgende Buchstaben benutzt (Leitwerte in Einheiten des charakteristischen Leitwerts der Leitung):

G_P = Leitwert des Parallelwiderstands,

G_R = Resonatorleitwert bei Resonanz, an einem Ort der Transmissionslinie gemessen, an dem bei Verstimmung der Leitwert ∞ erscheint (*Verstimmung-Kurzschlussort*, vgl.[1])),

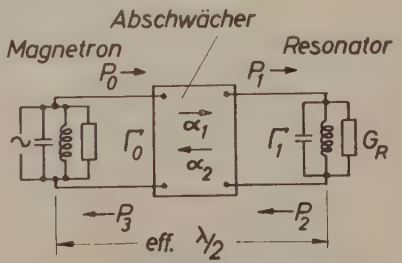

Abb. 2. Ersatzschaltbild beim Abschwächer.

λ = Leitungswellenlänge,

P_0, P_1 = Leistung der hinlaufenden Welle vor bzw. hinter dem Abschwächer,

[1]) Es wird vorausgesetzt, dass am Verstimmung-Kurzschlussort bei Abstimmung auf maximale Erregung des Resonators ein reiner Wirkleitwert entsteht. Das trifft genau genommen nicht zu, die Admittanz enthält noch einen kleinen (negativen) Blindleitwert, der von der Selbstinduktivität der Koppelschleife Transmissionslinie-Resonator (s. Abb. 4) herrührt. Vgl. z.B. E. L. Ginzton, Microwave Measurements (New York, 1957) S. 399. Für die hier angestellten Betrachtungen kann diese Tatsache aber unbeachtet bleiben, zumal sich der Blindleitwert im Bedarfsfall (unter gleichzeitiger Veränderung des Verstimmung-Kurzschlussortes) abgleichen lässt.

P_2, P_3 = entsprechende Leistungen der reflektierten Welle,
$|\Gamma_0| = (P_3/P_0)^{1/2}$ = Betrag des Spannungs-Reflexionskoeffizienten vor dem Abschwächer,
$|\Gamma_1| = (P_2/P_1)^{1/2}$ = Betrag des Spannungs-Reflexionskoeffizienten vor dem Resonator,
$\alpha_1 = P_1/P_0$ = Bruchteil der hindurchgelassenen Leistung in Vorwärtsrichtung,
$\alpha_2 = P_3/P_2$ = Bruchteil in Rückwärtsrichtung,
α = Sonderfall, in welchem $\alpha_1 = \alpha_2 = \alpha$ ist,
$10 \log (1/\alpha)$ = Dämpfung in dB,
r = *Welligkeit* = Verhältnis der Spannung im Maximum zu der im Minimum der stehenden Welle in der Transmissionslinie (= G bzw. G^{-1} in einer Leitung, die mit dem reellen Leitwert G abgeschlossen ist). Sofern nicht anders angegeben, ist das vorn am Magnetron gemessene r gemeint.

In beiden Schaltungen muss die elektrische Länge der Transmissionslinie $n\lambda/2$ ($n \leq$ ganze Zahl) betragen, um die unvermeidlichen "Zieherscheinungen" im erwünschten Sinne verlaufen zu lassen[2]).

Die Existenz einer Dämpfung ist in erster Linie für den Anschwingvorgang des mit Impulsen betriebenen Magnetrons wichtig. Im ersten Moment wirkt der Resonator so, als ob er verstimmt sei, d.h. wie ein Leitungskurzschluss. Zum Vergleich der verschiedenen Dämpfungsarten ist es daher zweckmässig, folgende Messgrössen zu betrachten:

(1) Die Welligkeit r_V bei verstimmtem Resonator, die nicht zu gross werden darf, wenn das Magnetron noch sicher anschwingen soll.

(2) Die Welligkeit r_R bei auf Resonanz abgestimmten Resonator, die massgebend für die dem Magnetron nicht abgenommene Leistung ist. Der Leistungsreflexionskoeffizient beträgt

$$\frac{P_{\text{refl.}}}{P_{\text{einf.}}} = \left(\frac{r_R - 1}{r_R + 1}\right)^2 . \tag{1}$$

(3) Das Aufteilungsverhältnis L der im Resonator zu der im Dämpfungsglied umgesetzten Leistung.

[2]) Eine Diskussion der Zieherscheinungen wird in der z.Z. vorbereiteten Veröffentlichung über das 5 MeV-PTB-Mikrotron gegeben.

Zwischen r_V, r_R und L einerseits und den Grössen G_P bzw. α_1, α_2 und G_R anderseits bestehen die im folgenden aufgestellten Beziehungen, die allerdings streng nur für eine feste Frequenz, also ohne Berücksichtigung der Zieherscheinungen gelten.

1.1. PARALLELWIDERSTAND

Um beim Anschwingen wirksam zu sein, muss der Leitwert G_P um die Strecke $(2n - 1)\,\lambda/4$ vor dem Resonator liegen. An den Ort von G_P transformiert beträgt der Resonatorleitwert bei Resonanz G_R^{-1}. Da man zur Erzielung einer günstigen Leistungsaufteilung und Anpassung stets $G_P \leqslant 1$ und $G_P + G_R^{-1} \geqslant 1$ wählen wird, ergibt sich

$$r_V = G_P^{-1} \quad \text{(Minimumsort } \lambda/4 \text{ vor } G_P) \tag{2}$$

$$r_R = G_P + G_R^{-1} \quad \text{(Minimumsort in } G_P) \tag{3}$$

$$L = (G_P G_R)^{-1} \tag{4}$$

Aus gemessenen Werten r_V und r_R kann man damit G_P und G_R ermitteln.

1.2. ABSCHWÄCHER

Der Aufstellungsort des in beiden Richtungen reflexionsfrei angenommenen Abschwächers ist beliebig, die Dämpfung für die hin- und die rücklaufende Welle gleich ($\alpha_1 = \alpha_2 = \alpha$). Im Gegensatz zum Parallelwiderstand sind r_R und L stets optimal bei $G_R = 1$, doch bedeuten kleine Abweichungen davon noch keine erhebliche Verschlechterung.

Die entsprechenden Gleichungen lauten

$$r_V = \frac{1 + \alpha}{1 - \alpha} , \tag{5}$$

$$r_R = \frac{1 + |\Gamma_1|\,\alpha}{1 - |\Gamma_1|\,\alpha} , \tag{6}$$

$$L = \frac{1 - \Gamma_1^2}{1/\alpha - 1 + \Gamma_1^2 (1 - \alpha)} \approx \frac{1}{1/\alpha - 1} , \tag{7}$$

wobei $|\Gamma_1| = (G_R - 1)/(G_R + 1)$ ist. Der Fehler der Näherung in Gl. (7) ist $< 10\%$, solange $\alpha < 0.83$ und $|\Gamma_1| < 0.24$ (d.h. $0.61 < G_R < 1.63$) ist, was leicht eingehalten werden kann.

Aus den gemessenen Werten von r_V und r_R lassen sich umgekehrt α aund G_R ermitteln:

$$\alpha = \frac{r_V - 1}{r_V + 1} , \tag{8}$$

$$\left.\begin{matrix} G_R \\ G_R^{-1} \end{matrix}\right\} = \frac{r_V - r_R}{r_V r_R - 1}, \text{ sofern } \left\{\begin{matrix} G_R \leqslant 1 \\ G_R \geqslant 1 \end{matrix}\right. . \quad (9)$$

Um r_V etwas zu verkleinern, kann man an geeigneter Stelle vor dem Abschwächer einen Transformator, z.B. einen $\lambda/4$-Transformator mit der charakteristischen Admittanz $Y_{Tr} > 1$, einfügen. Dieser ist aber auch bei Resonanz wirksam. Um seinen Einfluss hier zu vermindern, wird man G_R auf einen Wert > 1 erhöhen, jedoch nicht zu viel, weil damit r_R (s. Gl. (6)) und die Leistungsreflexion am Hohlraum ansteigt. Das Optimum liegt bei einem r_R-Wert zwischen 1 und Y_{Tr}. r_V und r_R sind in diesem Falle zu ersetzen durch

$$r'_V = r_V / Y_r^2 \quad (10)$$

$$r'_R = Y_{Tr}^2 / r_R \quad (11)$$

Y_{Tr}^2 errechnet sich als Funktion von G'_R, r'_V und r'_R zu

$$Y_{Tr}^2 = (G_R/2)\,(r'_R - 1/r'_V) + \\ + \{[(G_R/2)\,(r'_R - 1/r'_V)]^2 + r'_R/r'_V\}^{1/2} . \quad (12)$$

Nach diesen Gleichungen berechnete Betriebswerte sind in Tab. 1 zuzammengestellt, wobei für den Ferritisolator die Werte der Uniline-Type S 161 bei der benutzten Frequenz (2.8 GHz) eingesetzt sind. Für Parallelwiderstand und Abschwächer wurden in den ersten drei Spalten solche Werte angenommen, dass $L = 3$ herauskommt.

Beim Parallelwiderstand hat man die Wahl, zur Erzielung des gleichen L entweder r_R oder r_V jeweils zu Lasten des anderen zu begünstigen. Zwei mögliche Kombinationen sind in der Tabelle aufgeführt. Die erste zielt auf ein stabiles Anschwingen des Magnetrons ab ($r_V = 2.5$), wodurch wegen $r_R = 1.6$ nach Gl. (1) im Resonanzbetrieb eine Leistungsreflexion von 5.3% in Kauf genommen werden muss; bei der zweiten ist die Leistungsreflexion geringer (2%) auf Kosten des r_V. Beim Abschwächer, erste Spalte, fällt der hohe, auf Frequenz-Instabilität hindeutende r_V-Wert auf. Es wurde deshalb die Verwendung eines Transformators zwischen

Tabelle 1

	Parallelwiderstand		Abschwächer		Uniline
G_P	0.4	0.33	—	—	$\alpha_1 = 0.76$
α	—	—	0.75	0.61	$\alpha_2 = 0.042$
G_R	0.833	1	1	1.2	1
r_R	1.6	1.33	1	1.5†	1
r_V	2.5	3	7	2.5†	1.44
L	3	3	3	1.6	3.13

† Hier sind r'_R bzw. r'_V nach Gl. (11) bzw. Gl. (10) angegeben, wobei Y_{Tr}^2 zu 1.68 angenommen wurde.

1.3. FERRITISOLATOR

Es ist $\alpha_1 > \alpha_2$, und es ergeben sich die Formeln

$$r_V = \frac{1 + \sqrt{\alpha_1 \alpha_2}}{1 - \sqrt{\alpha_1 \alpha_2}}, \quad (13)$$

$$r_R = \frac{1 + |\Gamma_1| \sqrt{\alpha_1 \alpha_2}}{1 - |\Gamma_1| \sqrt{\alpha_1 \alpha_2}}, \quad (14)$$

$$L = \frac{1 - \Gamma_1^2}{1/\alpha_1 - 1 + \Gamma_1^2 (1 - \alpha_2)} \approx \frac{1}{1/\alpha_1 - 1} . \quad (15)$$

Magnetron und Abschwächer vorgesehen, durch den r_V auf Kosten von r_R verbessert wird (Gl. (10) und (11)). Die Verschlechterung von r_R wurde zu einem Teil durch die Wahl eines $G_R > 1$ wieder ausgeglichen. Bei Annahme von r'-Werten, die etwa den r-Werten beim Parallelwiderstand, erste Spalte, entsprechen, gelangt man zu den in der zweiten Spalte beim Abschwächer wiedergegebenen Zahlen. Es zeigt sich, dass jetzt das Leistungs-Aufteilungs-

verhältnis wesentlich ungünstiger ist. Der Abschwächer ist also auch noch bei Einschaltung des Transformators dem Parallelwiderstand unterlegen. Das beste Wertetripel r_R, r_V und L ergibt sich für die Uniline. Ob sie bezüglich der Leistungsausnutzung dem Parallelwiderstand wirklich überlegen ist, hängt aber davon ab, bei welchem maximalen r_V-Wert das Magnetron noch frequenzstabil anschwingt.

2. Versuchsanordnung

Die Messungen bei hoher Leistung wurden mit dem Magnetron 4 J 47 ($\lambda = 10.7$ cm), die vorbereitenden Messungen mit einem 100 mW-Reflexklystron durchgeführt, das gegen Rückwirkungen aus der Messleitung durch einen

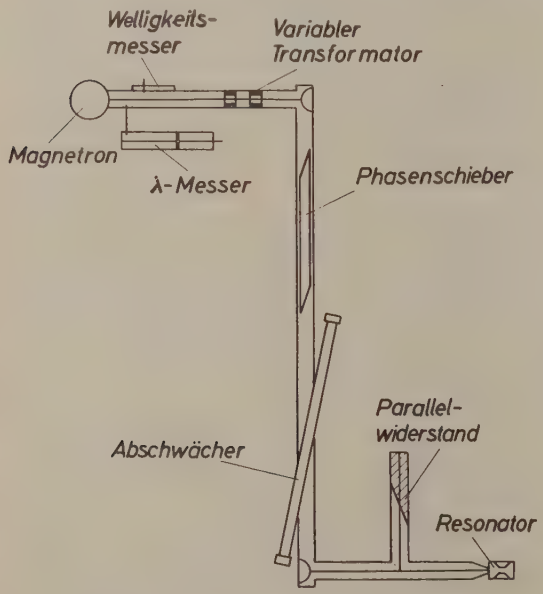

Abb. 3. Gesamtplan des Wellenleiter-Systems.

12 dB-Abschwächer geschützt war. Das Wellenleitersystem ist in Abb. 3 skizziert. Der Resonator war dem von Henderson u.a.[3]) beschriebenen ähnlich mit dem Unterschied, dass die Hf-Energie aus einer konzentrischen Transmissionslinie mittels Schleifenkopplung zugeführt wurde (Abb. 4). Durch Verdrehen der Schleife liessen sich beliebige G_R-Werte reproduzierbar einstellen. Die Resonatorabstimmung erfolgte durch Hineindrücken des einen Kegels, der in eine gewellte Membran eingelötet war. Es konnte die gesamte Resonanzkurve (Leistungs-Halbwertsbreite < 1.8 MHz) durchfahren werden. Um dabei das Magnetron nicht zu schädigen, wurde es nur mit 15 kV- (anstatt 25 kV-) Impulsen betrieben. Die maximale Erregung des Resonators wurde bei den Klystronmessungen mittels Detektor in der Resonatorwand, beim Magnetronbetrieb aus der Maximalenergie der im Resonator beschleunigten Elektronen bestimmt. Trotz der herabgesetzten Magnetronleistung war die Intensität der durch Feldemission entstandenen Elektronen für die Leuchtschirmbeobachtung im Magnetfeld ausreichend. Die Höchstenergien betrugen 200–300 keV (s.u.). Der elektrische Abstand Magnetron-Resonator war bei allen Anordnungen der gleiche (ca. 16 λ).

2.1. PARALLELWIDERSTAND

Beim Parallelwiderstand (Abb. 4) kann die Auffindung des $(2n - 1)$ $\lambda/4$-Abstandes zum Resonator in einfachen Fällen rechnerisch nach der von Demos u.a.[4]) für Rechteckrohre beschriebenen Methode erfolgen. Wir haben ihn am Klystronmessplatz experimentell bestimmt, was in drei Schritten vor sich ging:

(1) Messung ohne Seitenarm. Ermittlung des Verstimmung-Kurzschlussortes in der Gegend des Raumes A.

(2) Messung mit Seitenarm ohne Resonator. Ein verschiebbarer Kurzschlussstempel und ein reflexionsfreier Abschluss im Raum A stellten $G_R = \infty$ und $G_R = 1$ dar. Im Probierverfahren wurden verschiedene G_P-Werte zwischen 0.3 und 1 und der richtige Abstand Kurzschlussstempel-Seitenarm gefunden. Er ist dadurch gekennzeichnet, dass bei ihm r am kleinsten ist, dass G_P bei $G_R = \infty$ und $G_R = 1$ entsprechend den Gleichungen (2) und (3) denselben Wert ergibt, und dass der Abstand zwischen den Minimumsorten für $G_R = \infty$ und $G_R = 1$ $\lambda/4$ beträgt. Der richtige Abstand Kurzschluss-

[3]) C. Henderson, F. F. Heymann und R. E. Jennings, Proc. Phys. Soc. B **66** (1953) 654.

[4]) P. T. Demos, A. F. Kip und J. C. Slater, J. Appl. Phys. **23** (1952) 53.

stempel-Seitenarmmitte ist experimentell etwas grösser als $\lambda/4$, weil die Leitungswellenlänge im Gebiet der Abzweigung variiert.

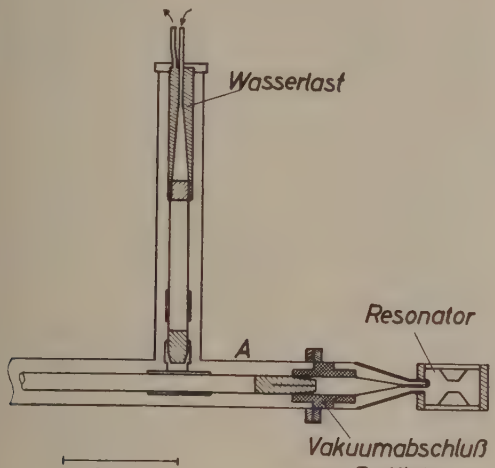

Abb. 4. Parallelwiderstand und Resonator. Der Trolitul-Vakuumverschluss muss zur Vermeidung von Störungen mindestens 10 cm von der Abzweigung entfernt sein. Er wurde mit Pizein eingekittet und aussen zusätzlich durch Madenschrauben fixiert.

(3) Bemessung des Abstandes Seitenarm-Resonator so, dass der nach (1) ermittelte Verstimmung-Kurzschlussort auf den nach (2) ermittelten Ort des Kurzschlussstempels zu liegen kommt. Die Genauigkeit, mit welcher der Abstand ermittelt werden muss, wird dadurch bestimmt, dass bei merklichen Abweichungen davon hohe Spannungen der stehenden Welle in der Leitung zwischen dem Resonator und dem Seitenarm, verbunden mit Überschlagsgefahr und Leistungsverlusten, auftreten.

Zur Herstellung verschiedener G_P-Werte dienten $\lambda/4$ Transformatoren im Seitenarm. Sie bestanden aus Hülsen verschiedenen Durchmessers die an ihren Enden als federnde Lamellen ausgebildet waren und auf dem Innenleiter verschoben werden konnten. Der Seitenarm war am Ende durch eine Wasserlast reflexionsfrei abgeschlossen. Durch Messung von r_V wurde für jeden Transformator entsprechend Gl. (2) der G_P-Wert bestimmt.

2.2. ABSCHWÄCHER

Den Abschwächer (Abb. 5) bildeten zwei wasserdurchflossene Kunststoffrohre (ø innen 3.8, ø aussen 8.5 mm), die sich im Innern des Rechteckhohlleiters über je 20 cm Länge erstreckten und zu einem Teil ihrer Länge eine spitz auslaufende Gummischnur (3.1 mm ø) enthielten. Die Gummischnüre ragten gleichweit in den Hohlleiter hinein. Durch Verschieben beider Rohre konnte die Dämpfung in sehr weiten Grenzen variiert werden. Der Abstand der Rohre in der Leitungsrichtung betrug $(3/4)\,\lambda$ (genau genommen etwas weniger: hier 115 anstatt 120 mm, um für eine mittlere Einstellung die Wellenlängenverkürzung durch die Wasseradern zu berücksichtigen). Dadurch blieb die Welligkeit stets < 1.15. Zur Ermittlung von α in Abhängigkeit von der Einstellung der Rohre wurde ein Detektor mit bekannter

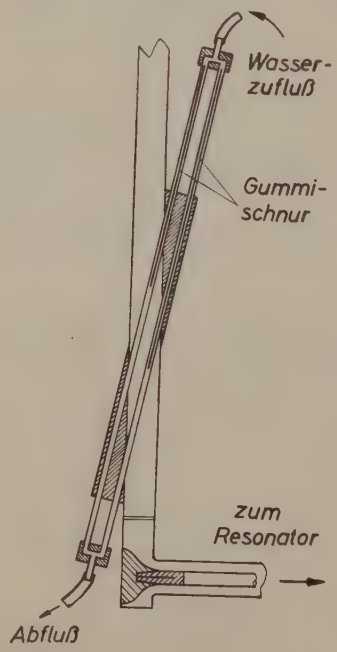

Abb. 5. Der Abschwächer.

Kennlinie hinter dem Abschwächer angebracht und die Leitung reflexionsfrei abgeschlossen. Ohne Wasser in den Rohren ist die Abschwächung gleich Null, $\alpha = 1$.

2.3. UNILINE

Die Uniline wurde in der gleichen Weise wie der Abschwächer (Abb. 5) eingesetzt.

3. Ergebnisse

Abb. 6 zeigt einige typische, mit dem Magnetron aufgenommene Admittanzkurven im Smithdiagramm. Bei grosser Dämpfung ergeben sich wie bei den Klystronmessungen nahezu Kreise, bei geringer dagegen schwachgekrümmte Kurven. Die Endpunkte V_1 und V_a der Kurven bedeuten "Verstimmung" des Resonators durch Bewegung des Kegels (s. Abschnitt 2) von der Resonanzstellung aus nach "innen" bzw. "aussen".

Die Streckung der Kurven mit abnehmender Dämpfung ist eine Wirkung der langen Linie (long line effect) und der zunehmenden Zieherscheinung. Bei V_a schwingt das Magnetron mit kleiner, bei V_1 mit grosser Wellenlänge, sofern der Phasenschieber richtig auf "$\lambda/2$-Abstand" zwischen Magnetron und Resonator eingestellt war. Weicht seine Einstellung hiervon ab, dann ändert sich die Wellenlänge beim Durchstimmen des Resonators an gewissen Stellen sprunghaft, und die bisher zwischen V_1 und V_a liegende grosse Lücke in der Admittanzkurve rückt an eine andere Stelle; V_1 und V_a liegen dann dicht beieinander.

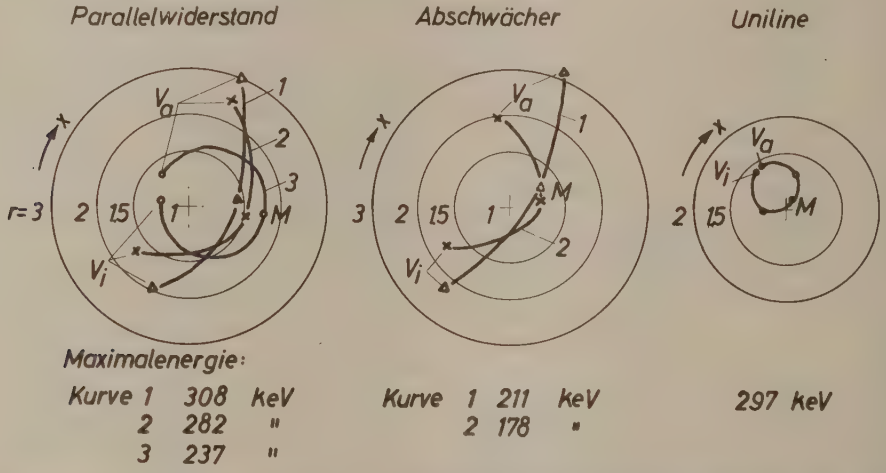

Abb. 6. Admittanzkurven im Smithdiagramm. V_a = Resonatorverstimmung bei aussenliegendem, V_i bei innen liegenden Kegel, M = Maximalerregung des Resonators. x = Abstand des Minimumsortes von einem generatorwärts gelegenen Bezugspunkt der Transmissionslinie aus (1 Umlauf = $\lambda/2$). Die Vakuum-Wellenlängen betrugen bei den Kurven 1 des Parallelwiderstandes und des Abschwächers ziemlich übereinstimmed bei V_a 106.43, bei M 106.68 und bei V_i 107.10 mm. Die Wellenlängen beim Admittanzkreis der Uniline lagen zwischen den Grenzen 106.64 und 106.79 mm. Die Maximalenergie, die man erzielen würde, wenn man ohne Dämpfung arbeiten könnte, beträgt etwa 400 keV.

Tabelle 2

Experimentell erreichte Werte bei Erregung des Magnetrons mit 15 kV-Impulsen

	Parallelwiderstand	Abschwächer	Uniline
Kleinstmögliche Dämpfung	$G_P = 0.36$	$\alpha = 0.54$	s. Tab. 1
Maximale Energie, keV	308 ± 15	211 ± 10	297 ± 5
Leistungsaufteilung L	3.1	1.2	3.1

Mit abnehmender Dämpfung wird die genaue $\lambda/2$-Einstellung des Phasenschiebers immer kritischer und die Schwingungsfrequenz des Magnetrons unsicherer, bis schliesslich kein einwandfreier Dauerbetrieb mehr möglich ist. In Tab. 2 sind die bei den kleinstmöglichen Dämpfungen erreichten Maximalerregungen des Hohlraums, gemessen durch die Energie der beschleunigten Elektronen, aufgeführt; die Fehlergrenzen geben die Schwankungsbreite bei Wiederholung der Versuche an. Die Werte für G_P und α wurden den beschriebenen Klystronmessungen entnommen, da die am Magnetron gefundenen r_V-Werte, aus denen sich G_P und α nach den Gleichungen (2) und (8) ebenfalls berechnen liessen, wegen der Zieherscheinungen uneinheitlich sind. Sie werden durch wellenlängenabhängige Reflexionen in der Transmissionslinie beeinflusst. Die Vergrösserung des Resonatorleitwerts G_R durch die Feldelektronenemission macht sich bei den Maximalspannungen von 300 kV erst wenig bemerkbar. Die dadurch hervorgerufene Unsicherheit bei der Bestimmung der Leistungsaufteilung L ist kleiner als 10%.

4. Diskussion

Die Versuche bestätigen die vermutete Überlegenheit des Parallelwiderstandes über den Abschwächer (Tab. 2). Es sieht so aus, als ob die r_V-Werte auch quantitativ die kleinstmögliche Dämpfung bestimmen, gleichgültig, um welchen Typ der Dämpfung es sich handelt (vgl. die ähnliche Lage der Endpunkte der beiden Kurven 1 in Abb. 6). Es ist denkbar, dass bei einer Verkleinerung des Abstandes Magnetron–Resonator die kleinstmögliche Dämpfung noch etwas weiter verringert werden kann. Die mit der Uniline erreichte Leistungsausnutzung übertrifft nicht die mit dem Parallelwiderstand erreichte; allerdings besitzt die hier benutzte Type eine verhältnismässig grosse Abschwächung in Vorwärtsrichtung (1, 2 dB). Es bleiben jedoch die sonstigen Vorteile eines Ferritisolators: seine bequeme, vom Ort unabhängige Einbauweise, die unkritische Einstellung des Phasenschiebers und die bessere Isolation des Magnetrons im Fall von Überschlägen im Resonator oder in der Leitung.

Herrn Dipl.-Phys. Trier danke ich für seine Unterstützung bei der Durchführung der Messungen.

NUCLEAR INSTRUMENTS 3 (1958) 104–108; NORTH-HOLLAND PUBLISHING CO. – AMSTERDAM

INVESTIGATION OF A BETA-RAY SPECTROMETER WITH A TRIANGULAR FIELD

INGVAR LINDGREN

Institute of Physics, University of Uppsala, Uppsala

Received 29 March 1958

A long lens beta-ray spectrometer with a pure "triangular" field is here investigated theoretically. A point source as well as a disk source is considered. It is shown that the effect of the source width on the resolution is much smaller with this field than with a uniform field. The spherical aberration is rather large, but the maximum luminosity at a given resolution is larger than with a uniform field. The results are in agreement with experiments.

1. Introduction

The long lens beta-ray spectrometer is widely used because of its high transmission. The field is usually approximately uniform, which gives a fairly low spherical aberration. The uniform field spectrometer has been investigated by several authors[1–3]). Often, however, it is necessary to use rather large sources to get high intensities. In such cases the uniform field is not particularly suitable, since the broadening of the ring-focus from the source width is equal to the source diameter.

It is the purpose of this paper to show that in a "triangular" field, that is an axially symmetrical field with linearly increasing field strength on the axis from zero at the source, the effect of a disk source is largely reduced. In fact, at an emission angle of 20° the minimum width of the beam bundle is less than 1/5 of the source diameter. This minimum does not occur exactly at ring-focus, where the spherical aberration has its minimum. But in spite of this the triangular field gives a higher luminosity than the uniform field does.

The triangular field is suitable in coincidence spectrometers, since the field strength is zero at the source. A field of approximately triangular shape has been used in a coincidence spectrometer by Gerholm[4]). In experiments together with the author it was shown that the minimum width of the total beam bundle (inclusive broadening due to the spherical aberration under ordinary conditions of operation is smaller than the source diameter.

2. Equations of Motion

The triangular field has been investigated by calculations of different electron trajectories.

In an axially symmetrical magnetic field the vector potential satisfies in cylindrical coordinates (r, φ, z) the equation

$$\frac{\partial^2 A}{\partial r^2} + \frac{\partial}{\partial r}\left(\frac{A}{r}\right) + \frac{\partial^2 A}{\partial z^2} = 0 \,.$$

The solution can be expressed

$$A(r, z) = \frac{1}{2} B_0(z)\, r - \frac{1}{2}\frac{B''_0(z)}{2\cdot 4} r^3 + \\ + \frac{1}{2}\frac{B_0^{(4)}(z)}{2\cdot 4\cdot 4\cdot 6} r^5 - \cdots,$$

where $B_0(z)$ is the field strength on the axis.

The equations of motion of an electron (with the charge $-e$ and the mass m) are in an axially symmetrical magnetic field[5])

$$\begin{cases} \ddot{r} = -\left(\frac{e}{m}\right)^2 \left(A - \frac{C}{r}\right)\left(\frac{\partial A}{\partial r} + \frac{C}{r^2}\right) \\ \ddot{z} = -\left(\frac{e}{m}\right)^2 \left(A - \frac{C}{r}\right)\frac{\partial A}{\partial z} \\ \dot{\varphi} = \frac{e}{m}\left(A - \frac{C}{r}\right)\frac{1}{r} \,. \end{cases}$$

[1]) E. Persico, Rev. Sci. Instr. **20** (1949) 191.
[2]) J. W. M. De Mond, Rev. Sci. Instr. **20** (1949) 160 and 616.
[3]) F. H. Schmidt, Rev. Sci. Instr. **23** (1952) 361.
[4]) T. R. Gerholm, Rev. Sci. Instr. **26** (1955) 1069.
[5]) L. S. Goddard, Proc. Phys. Soc. **56** (1944) 372.

The last equation at once gives the constant $C = r_0 A_0 - (m/e)\, r_0^2\, \dot{\varphi}_0$, the subscript $_0$ indicating initial values. Substituting the series for A into these equations, one obtains

$$\left\{\begin{aligned}
\ddot{r} &= -\left(\frac{e}{m}\right)^2 \left[\frac{1}{4} B_0^2 r - \frac{1}{8} B_0 B''_0 r^3 + \right. \\
&+ \left(\frac{3}{256} B''^2_0 + \frac{1}{128} B_0 B_0^{(4)}\right) r^5 - \cdots \\
&\left. - \frac{C^2}{r^3} + C\left(\frac{1}{8} B''_0 r - \frac{1}{96} B_0^{(4)} r^3 + \cdots\right)\right] \\
\ddot{z} &= -\left(\frac{e}{m}\right)^2 \left[\frac{1}{4} B_0 B'_0 r^2 - \right. \\
&- \frac{1}{32} (B'_0 B''_0 + B_0 B'''_0)\, r^4 + \cdots \\
&\left. - C\left(\frac{1}{2} B'_0 - \frac{1}{16} B'''_0 r^2 + \cdots\right)\right].
\end{aligned}\right.$$

The equations then become

$$\left\{\begin{aligned}
\ddot{\rho} &= -\beta_0^2 \rho + \frac{1}{2} \beta_0 \beta''_0 \rho^3 - \\
&- \left(\frac{3}{64} \beta''^2_0 + \frac{1}{32} \beta_0 \beta_0^{(4)}\right) \rho^5 + \cdots \\
&+ 4 \frac{C'^2}{\rho^3} - C'\left(\frac{1}{2} \beta''_0 \rho - \cdots\right) \\
\ddot{\zeta} &= -\beta_0 \beta'_0 \rho^2 + \frac{1}{8} (\beta_0 \beta''_0 + \beta_0 \beta'''_0)\, \rho^4 - \cdots \\
&+ C'\left(2\beta'_0 - \frac{1}{4} \beta'''_0 \rho^2 + \cdots\right)
\end{aligned}\right.$$

and $$C' = \frac{C}{D^2 B_1} = \frac{1}{2} \rho_0 \sin\alpha \sin\varphi_0 ,$$

the dots now representing derivates with respect to τ.

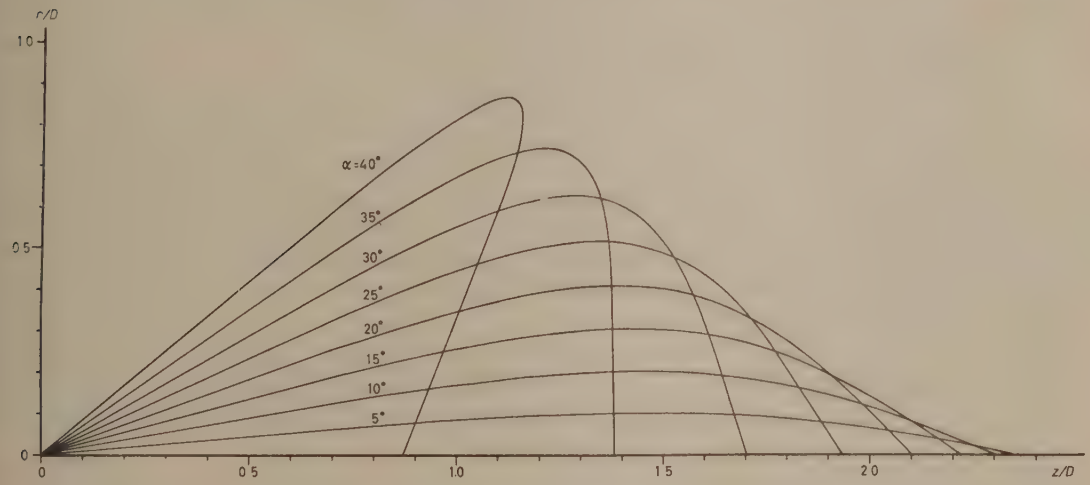

Fig. 1. Electron trajectories in a triangular field from a point source on the axis for different emission angles.

If the initial velocity is assumed to be parallel to the plane $\varphi = 0$, the constant C can be written $C = (m/e)\, v\, r_0 \sin\alpha \sin\varphi_0$, where v is the velocity and α the emission angle. If the electron crosses the axis the constant C is zero.

To get a suitable dimensionless form of the equations of motion the following substitutions are made,

$$\rho = \frac{r}{D}, \quad \zeta = \frac{z}{D}, \quad \tau = \frac{t}{T}, \quad \beta_0(\zeta) = \frac{B_0(z)}{B_1},$$

where $$D = \frac{2mv}{eB_1} \quad \text{and} \quad T = \frac{2m}{eB_1}$$

(B_1 so far arbitrary).

In a triangular field $B_0(z) = kz$, where k is a constant. If the field strength B_1 above is chosen to be $B_1 = kD$, one gets

$$D = \sqrt{\frac{2mv}{ek}} \quad \text{and} \quad T = \sqrt{\frac{2m}{ekv}}$$

and the equations of motion become

$$\left\{\begin{aligned}
\ddot{\rho} &= -\rho\zeta^2 + \frac{\rho_0^2}{\rho^3} \sin^2\alpha \sin^2\varphi_0 \\
\ddot{\zeta} &= -\rho^2 \zeta + \rho_0 \sin\alpha \sin\varphi_0 .
\end{aligned}\right.$$

3. Point Source

With a point source the equations of motion are reduced to

$$\begin{cases} \ddot{\rho} = -\rho\zeta^2 \\ \ddot{\zeta} = -\rho^2\zeta \, . \end{cases}$$

These equations have been solved numerically for different values of α (see appendix). Some electron trajectories are shown in fig. 1.

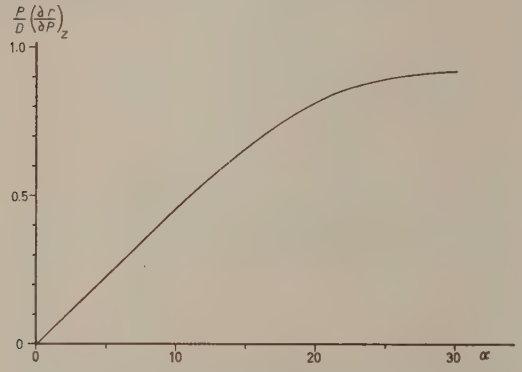

Fig. 2. The momentum dispersion at ring-focus as a function of the emission angle.

The spherical aberration is determined graphically from the trajectories. In calculations of the resolution it is assumed that a baffle system of the Hubert[6]) type is used. That is, the beams are confined outwards by a number of edges on the envelope of a certain momentum and inwards by a single edge.

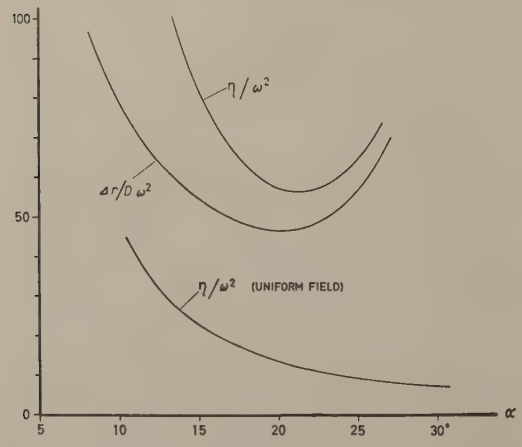

Fig. 3. The ring-focus width (Δr) and the resolution (η) in a triangular field as functions of the emission angle. The resolution in a uniform field is given for comparison.

With emission angles in the interval $\alpha \pm \Delta\alpha$, the width of ring-focus is approximately $\Delta r = \frac{1}{2}(\partial^2 r/\partial\alpha^2)_z\,(\Delta\alpha)^2$. The *base resolution* is defined $\eta = \Delta p/p$, where Δp is the *base width* of the momentum curve. This gives

$$\eta = \Delta r/p\left(\frac{\partial r}{\partial p}\right)_z = \frac{1}{2}\left(\frac{\partial^2 r}{\partial\alpha^2}\right)_z (\Delta\alpha)^2/p\left(\frac{\partial r}{\partial p}\right)_z .$$

The momentum dispersion $(\partial r/\partial p)_z$ (see fig. 2) has been determined graphically by means of the relation

$$\left(\frac{\partial r}{\partial p}\right)_z = \frac{\mathrm{d}D}{\mathrm{d}p}\left(\rho - \zeta\frac{\partial\rho}{\partial\zeta}\right) = \frac{D}{2p}\left(\rho - \zeta\frac{\partial\rho}{\partial\zeta}\right).$$

The ring-focus width and the resolution are given in fig. 3 as functions of the emission angle. The resolution has a minimum for a given gathering power $\omega \approx \Delta\alpha \sin\alpha$ at an emission angle of about 22°. The resolution of a uniform field has also been given in the same figure.

4. Disk Source

Some electron trajectories starting from different points off the axis have been calculated for $\alpha = 20°$. Fig. 4 shows trajectories for $r_0/D = 0.05$ and four values of φ_0, and in fig. 5 the width of the beam bundle for small sources is given. The minimum width is about $0.18 \times 2r_0$, that is less than 1/5 of the source diameter. At ring-focus with $\alpha = 20°$ ($z/D \approx 1.82$) the width is about 0.40 times the diameter.

With a gathering power ω and a source diameter $2s$ the width of the total beam bundle at ring-focus has the form

$$\Delta r = a\omega^2 + 2bs \, .$$

The maximum luminosity $L = \pi s^2\omega$ for a given resolution η is then

$$L_{\max} = 4\pi \cdot 5^{-5/2}\, a^{-1/2}\, b^{-2}\left[p\left(\frac{\partial r}{\partial p}\right)_z \eta\right]^{5/2}$$

and the optimum values of ω and s are

$$\omega_{\mathrm{opt}} = \left(\frac{Lb^2}{4\pi a^2}\right)^{1/5} \quad \text{and} \quad s_{\mathrm{opt}} = \left(\frac{2L^2 a}{\pi^2 b}\right)^{1/5}.$$

At the optimum conditions of operation the contribution of the source width to the ring-focus width is four times that of the spherical aberration. This rule is valid as long as the expression above for Δr holds. If the broadning

[6]) M. P. Hubert, Comptes Rendus **230** (1950) 1464.

due to the source width has a minimum at a point different from ring-focus, then the minimum of the total width may occur at some intermediate point. At such a point the width also contains a term linear in ω, and it can therefore be supposed that the total width has its minimum very near ring-focus.

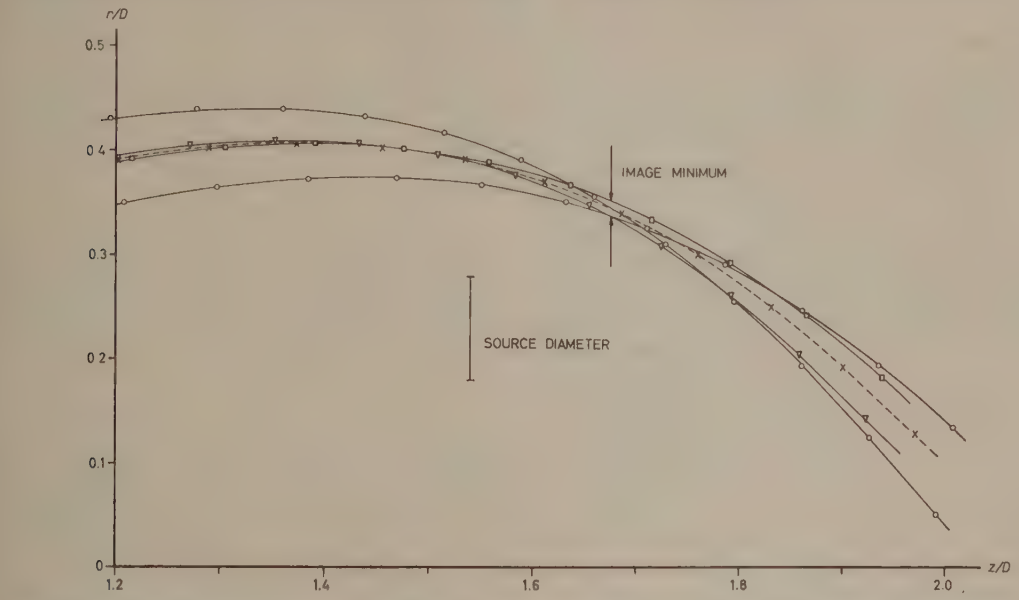

Fig. 4. Part of the trajectories from a disk source with the diameter $0.1D$. The full curves start from different points of the periphery of the source and the dotted curve from the center. The emission angle (α) is 20°.

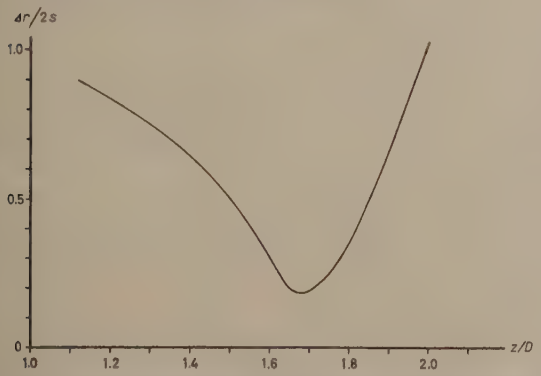

Fig. 5. The broadening due to the source width for small sources as a function of the distance from the source, ($\alpha = 20°$).

The maximum luminosity with a triangular field at $\alpha = 20°$ is approximately

$$L_{max} = 0.12\, D^2\, \eta^{5/2} .$$

In order to compare this value with that of other types of spectrometers, the luminosity is devided by the length times the diameter of the spectrometer (A), giving

$$L_{max}/A = 0.070\, \eta^{5/2} .$$

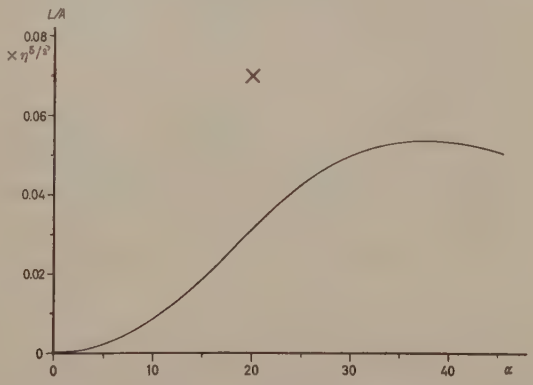

Fig. 6. The maximum luminosity of a uniform field spectrometer divided by the cross-section area of the spectrometer (curve). The cross represents the same quantity of a triangular field spectrometer at an emission angle of 20°.

The corresponding quantity of a uniform field spectrometer is given in fig. 6 as a function of

the emission angle. It is seen that the triangular field gives a higher luminosity at $\alpha = 20°$ than the uniform field does at the optimum conditions of operation ($\alpha \approx 35°$).

5. Discussion

The triangular field shape is certainly not the most suitable for a long-lens spectrometer. The broadening of the beam bundle due to the finite source width has, as shown above, a minimum between the source and the ring-focus. Therefore, with some field shape between the triangular and the uniform one, the two minima might coincide, which would give a large increase in luminosity. Such a field would probably also give a much smaller spherical aberration than the pure triangular field. This assumption is supported by investigations made by Ramberg and Blaugrund[7]) recently. They have for a point source investigated a field, triangular near the source and uniform for the rest, and shown that the spherical aberration is almost constant, when the length of the triangular part is small but rapidly increasing beyond a certain point.

6. Acknowledgement

The author is much indebted to Docent T. R. Gerholm for several stimulating discussions and to Professor Kai Siegbahn for his interest.

This work has been supported by the Swedish Atomic Committee.

[7]) Y. Ramberg and A. E. Blaugrund, Rev. Sci. Instr. 28 (1957) 286.
[8]) W. E. Milne, Bull. Nat. Res. Council 92 (1933) 71.
[9]) D. R. Hartree, Manch. Lit. Phil. Soc. 77 (1933) 91.

7. Appendix

A.1. NUMERICAL INTEGRATION OF THE EQUATION $(d^2y/dx^2) = f(x, y)$

The ordinary differential equation $y'' = f(x, y)$ can be rapidly integrated by the following method of Störmer and Milne[8, 9]).

The solution is assumed to be known in a number of equidistant points, $y_0, y_1, y_2, \cdots y_n$, $(y_k = y(a + kh))$. The value of y_{n+1} is then obtained with the following formulas,

$$\Delta y_n = \Delta y_{n-1} + h^2\left[y''_n + \frac{1}{12}\Delta^2 y''_{n-2} + \right.$$

$$\left. + \frac{1}{12}\Delta^3 y''_{n-3} + \frac{19}{240}\Delta^4 y''_{n-4} + \cdots\right] = \Delta y_{n-1} +$$

$$+ h^2\left[y''_n + \frac{1}{12}\Delta^2 y''_{n-1} - \frac{1}{240}\Delta^4 y''_{n-2} + \cdots\right],$$

where

$$\Delta y_k = y_{k+1} - y_k, \qquad \Delta^2 y_k = \Delta y_{k+1} - \Delta y_k, \text{ etc.}$$

A preliminary value of y_{n+1} is calculated by means of the first expression for Δy_n and then, after completition of the difference scheme, corrected with the second expression.

The starting points can usually be obtained by expanding the solution in a power series. If this expansion is impossible or difficult the starting values can often be obtained with sufficient accuracy by successive approximations of the following formulas,

$$\Delta y_0 = hy'_0 + h^2\left[\frac{1}{2}y''_0 + \frac{1}{6}\Delta y''_0 - \right.$$

$$\left. - \frac{1}{24}\Delta^2 y''_0 + \frac{1}{45}\Delta^3 y''_0 - \frac{7}{480}\Delta^4 y''_0 + \cdots\right]$$

$$\Delta y_1 = \Delta y_0 + h^2\left[y''_1 + \frac{1}{12}\Delta^2 y''_0 - \frac{1}{240}\Delta^4 y''_0 + \cdots\right]$$

etc.

NUCLEAR INSTRUMENTS 3 (1958) 109–115; NORTH-HOLLAND PUBLISHING CO. – AMSTERDAM

FIELDS IN SLANTED-GAP EXCITED RECTANGULAR DUCTS

J. VAN BLADEL

Midwestern Universities Research Association† and Department of Electrical Engineering, University of Wisconsin

Received 12 October 1957

Revised Manuscript Received 15 April 1958

Some features of the electromagnetic field in a rectangular wave-guide, cut in two by a plane making an angle θ with the guide's longitudinal axis, are examined. The field is excited by a voltage applied across the two halves of the guide. Several values of θ, frequency (between zero and cut-off), and aspect ratio of the cross-section are considered. The problem is of interest for the design of particle accelerators, and, with this particular application in mind, data are presented for the energy and momentum kicks which particles experience when crossing the gap.

1. Introduction

One of the methods used to accelerate particles in a circular accelerator consists of cutting the walls of the vacuum tank by a transverse cross-section, and applying an alternating voltage $V \cos \omega t$ across the lips of the resulting gap. The plane of the gap is normally perpendicular to the axis of the accelerator "doughnut". In some cases, however, a slanted gap of the type depicted in fig. 1 is of interest:

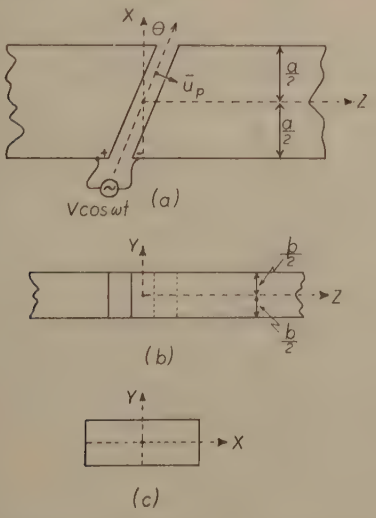

Fig. 1. Gap-excited accelerator (a) top view (b) side-view (c) cross-sectional view.

† Supported by Contract AEC AT (11-1)-384.

(a) either because it applies a lateral momentum kick to the particles, and in so doing counteracts some undesirable feature of their trajectories (betatron oscillations, R.F. knock-out, etc.);

(b) or because the shape of the focusing magnets is incompatible with the use of a straight radial gap, as appears to be the case with the spiral magnets now being considered at MURA[1]).

One often endeavours, by proper design of the external sources of excitation (cavities, two-wire lines connected right across the gap, etc.), to obtain a gap voltage which is constant in phase and magnitude all along the gap contour. This, presumably, would result in the particles being subjected to an accelerating voltage independent of position within the vacuum chamber. If the gap is very narrow, such a voltage will impress a tangential field of the form

$$\boldsymbol{E}_t = V \cos \omega t \, \delta(p) \, \boldsymbol{u}_p \qquad (1)$$

across the gap surface. In eq. (1), V is a constant, p is the direction perpendicular to the gap profile in the plane tangent to the guide boundary, and $\boldsymbol{u}$ is a unit vector. A common procedure in accelerator calculations consists of assuming a δ function behaviour similar to (1)

[1]) K. R. Symon, D. W. Kerst, L. W. Jones, L. J. Laslett and K. M. Terwilliger, Phys. Rev. **103** (1956) 1837.

for the electric field *within* the vacuum chamber, and of neglecting the effects of the magnetic field. With such an assumption, one finds out that a particle of charge q and velocity $\boldsymbol{v}$, crossing the plane of the gap at time $t_0 = \varphi_0/\omega_0$, is subjected to an energy increase $qV \cos \varphi_0$, and a lateral momentum kick $-(qV/v) \cos \varphi_0 \operatorname{tg} \theta \boldsymbol{u}$. The purpose of this paper is to investigate how good this "δ-function approximation" actually is. The investigation is restricted to rectangular cross-sections, a configuration which is currently used in MURA work.

2. Field Calculations

The actual value of the electromagnetic field in the gap region can be computed from a knowledge of the tangential field in the gap, as given by (1). Green's dyadic methods[2]) or, equivalently, a normal modes formalism[3]) are suitable for the purpose. The formulas one ends up with are extremely long[4]), and will not be reproduced here. A few representative results, obtained on an IBM 704 computer, are worth mentioning, however. Figs. 2 and 3 show the variation of E_Z and H_Y along the main axis of the guide, and give an idea of the penetration of the transverse magnetic and electric modes within the vacuum chamber. Clearly, as the frequency is raised, more and more of the vicinity of the gap is occupied by the field region. The unit of frequency is $f_c = c/2a$, the overall cut-off frequency of the guide, a value which is not reached in practical accelerator design. The flatness of the "doughnut" is measured by the aspect ratio $\tau = a/b$.

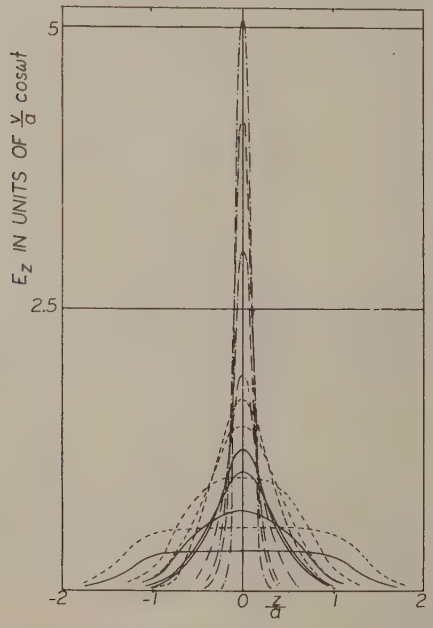

Fig. 2. E_z along the main axis $X = Y = 0$. Full, dashed, dot-dashed lines correspond to (a) $\tau = 1$, $f = 0$, (b) $\tau = 1$, $f = 0.75\, f_c$, (c) $\tau = 5$, $f = 0$ respectively. The most peaked curve of each family refers to $\operatorname{tg} \theta = 0$, the other three, in decreasing order of peak value, to $\operatorname{tg} \theta = 0.5$, 1 and 2.

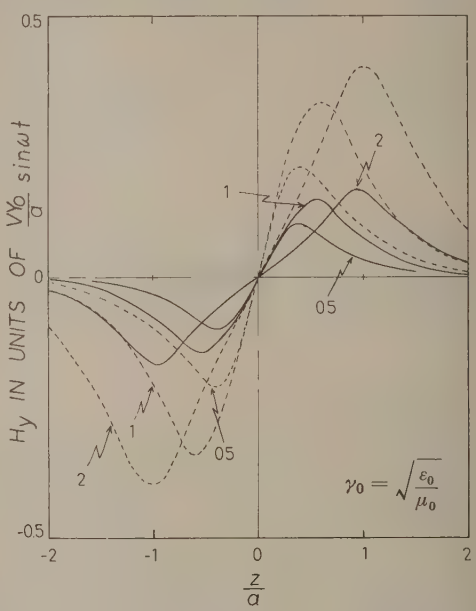

Fig. 3. H_y along the main axis $X = Y = 0$. The curves are labeled according to the value of $\operatorname{tg} \theta$. Full and dashed curves correspond to $f = 0.5\, f_c$ and $f = 0.75\, f_c$ respectively. Square cross-section.

The electric field in the O X Z plane is depicted in fig. 4 for a square cross-section. The shape of the lines of force is adequately suggested by the direction of the field vectors. The figure gives an idea of the spread of the electric field

[2]) P. M. Morse and H. Feshbach, Methods of Theoretical Physics (McGraw-Hill Co., New York, 1953) Ch. 13.

[3]) J. van Bladel, paper accepted for publication in Zeitschrift für Angewandte Mathematik und Physik.

[4]) J. van Bladel, MURA Internal Report 337 (August, 1957).

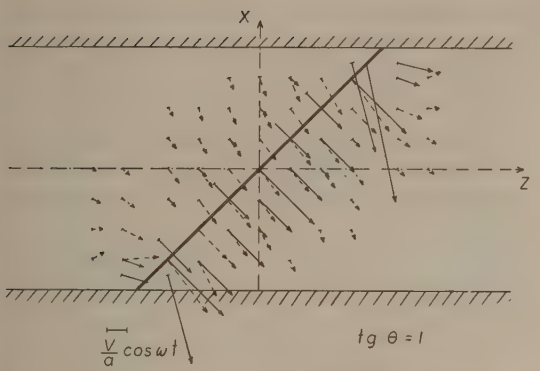

Fig. 4. Electric field in the $Y = 0$ plane for $\tau = 1$. Full and dashed arrows correspond to $f = 0$ and $f = 0.75\, f_c$ respectively.

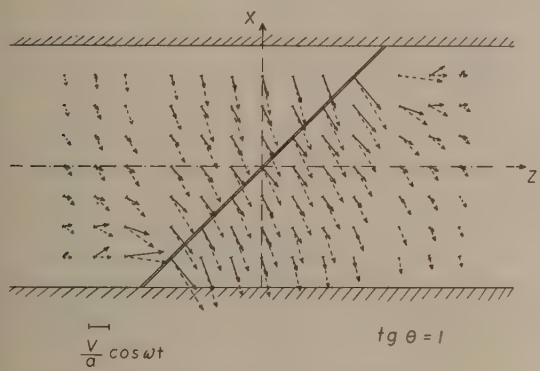

Fig. 5. Electric field in the $Y = 0$ plane for $\tau = 5$ (full arrows), and in the $Y = b/4$ plane for $\tau = 1$ (dashed arrows). In both cases $f = 0$.

over the gap region, and shows the deviation from a δ-function distribution. The concentration around the immediate vicinity of the plane of the gap is more pronounced when the vacuum chamber if flatter, and when points close to the gap itself are considered. This is evidenced by fig. 5. More detailed results for a gap perpendicular to the accelerator axis can be found elsewhere[5]).

Knowledge of the field at each point of the vacuum chamber allows one, in principle at least, to predict accurately the trajectories of particles incident on the gap region. General formulas taking velocity and angle of incidence into account are of a complicated nature, and will not be considered here. Considerable simplification, however, is afforded when the particle travels in a direction parallel to the accelerator axis, and the gap voltage is not of such magnitude as to materially alter the particle's linear motion upon crossing of the gap region. A knowledge of the energy and lateral momentum kicks impressed on the particle is of great interest in those circumstances. The remainder of the present paper is devoted to a discussion of these kicks, the formulas governing their behavior being deduced from a more general analysis published elsewhere[6]).

[5]) J. van Bladel, J. Appl. Phys. **28** (1957) 1479.
[6]) J. van Bladel, Nuclear Instruments **3** (1958) 52.

3. Energy Calculations

The longitudinal energy kick, for a particle crossing the $Z = 0$ plane when the gap voltage is equal to $V \cos \varphi$, turns out to be

$$\Delta \mathscr{E}(X, Y) = q \int_{-\infty}^{+\infty} E_Z(X, Y, Z, t)\, \mathrm{d}Z = qV_1 \cos \varphi + qV_2 \sin \varphi\,.$$

with the following expressions for V_1 and V_2:

$$V_1(X, Y) = -\frac{16\,V}{\pi^2} \cos\left(\operatorname{tg}\theta \frac{\nu}{\beta}\frac{\pi}{2}\right) \sum_{m=1,3}^{\infty} \sum_{n=1,3}^{\infty} \frac{(-1)^{\frac{m+n}{2}} \cos\dfrac{m\pi X}{a} \cos\dfrac{n\pi Y}{b}}{m^2 + n^2\tau^2 + \left(\dfrac{1}{\beta^2} - 1\right)\nu^2} \cdot \frac{m}{n} \cdot \left(1 + \frac{n^2\tau^2}{m^2 - \left(\operatorname{tg}\theta \dfrac{\nu}{\beta}\right)^2}\right), \quad (2)$$

$$V_2(X, Y) = -\frac{16\,V}{\pi^2} \sin\left(\operatorname{tg}\theta \frac{\nu}{\beta}\frac{\pi}{2}\right) \sum_{m=0,2}^{\infty} \sum_{n=1,3}^{\infty} \frac{(-1)^{\frac{m+n+1}{2}} \sin\dfrac{m\pi X}{a} \cos\dfrac{n\pi Y}{b}}{m^2 + n^2\tau^2 + \left(\dfrac{1}{\beta^2} - 1\right)\nu^2} \cdot \frac{m}{n} \cdot \left(1 + \frac{n^2\tau^2}{m^2 - \left(\operatorname{tg}\theta \dfrac{\nu}{\beta}\right)^2}\right). \quad (3)$$

In these expressions, $\nu = f/f_c$ is the frequency measured in terms of the cut-off value, $\beta = v/c$ is the velocity measured in terms of the velocity of light.

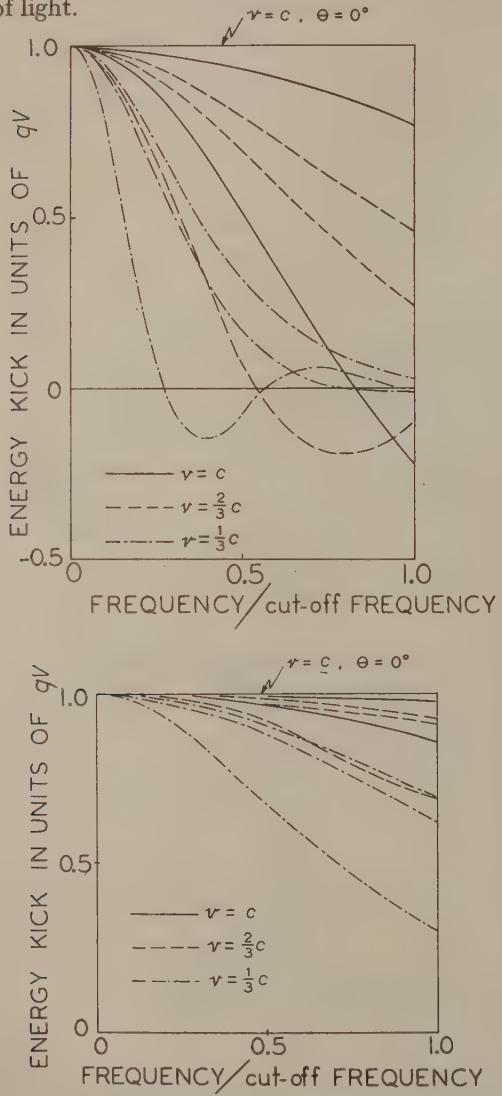

Fig. 6. "In phase" energy kick as a function of frequency, for $X = Y = 0$ and (a) $\tau = 1$, (b) $\tau = 5$. For each value of velocity, the three curves refer, starting from the uppermost, to $\theta = 0°$, 30°, 60° respectively.

The physical significance of the "in phase" voltage V_1 is clear. It is the voltage kick impressed on a particle crossing the $Z = 0$ plane when the gap voltage is maximum. The frequency dependence of V_1, for particles moving along the main axis of the guide, is depicted in fig. 6. It will be noticed that the full value of the gap voltage is obtained when the gap is perpendicular to the axis, and the particle travels at the velocity of light. For slanted gaps and lower velocities, the effective gap voltage is reduced by phase effects, even to the point of becoming "decelerating" for certain values of the parameters. This is further illustrated by fig. 7, where the variation of V_1 throughout the

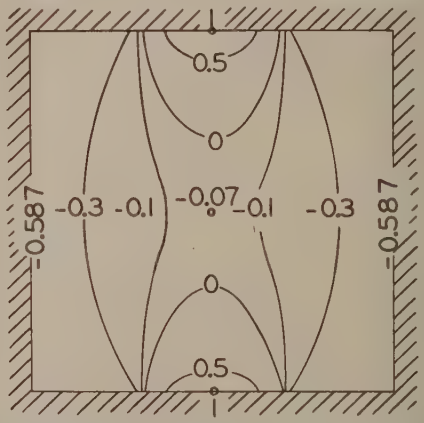

Fig. 7. Distribution of the "in phase" energy kick throughout a square cross-section. Parameters: $\theta = 60°$, $\nu = 0.5$, $v = \frac{1}{3}c$. Curves labeled in units of qV.

cross-section is displayed for a rather extreme set parameters. The voltage is seen to be decelerating for most of the points of the cross-section. When the slant angle is reasonably low, however, a more regular behavior is obtained. For a gap perpendicular to the axis, in particular, the effective voltage varies smoothly from the center of the guide, where it is minimum, towards the edges, where its value is equal to V. Still more particularly, the effective voltage is equal to V all through the cross-section for particles traveling at the velocity of light. This interesting result, by the way, is a characteristic property of perpendicular gaps, and is independent of the shape of the duct (rectangular, circular, etc.)[6]).

The physical significance of the "quadrature" voltage V_2 is equally clear. It is the voltage impressed on a particle crossing the $Z = 0$ plane

when the gap voltage is zero, and is becoming negative. It is immediately apparent that V_2 vanishes for a gap perpendicular to the axis, and parameters, is shown in fig. 9. It will be noticed that, in accordance with eq. (3), the quadrature voltage vanishes along the O Y axis. Its variation within the duct is more and more accurately represented by the "δ-function approximation" when (a) the velocity increases, (b) the frequency decreases, (c) the cross-section becomes flatter, (d) the slant angle decreases. The same conclusions are valid for the "in phase" voltage.

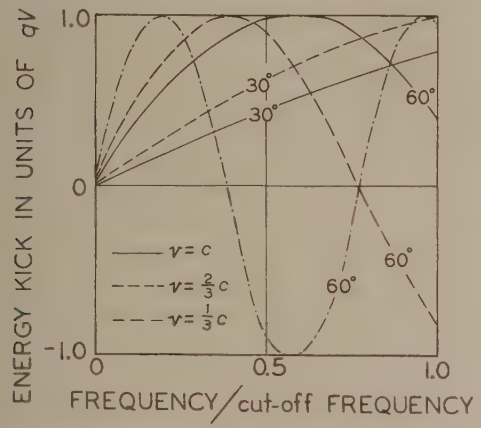

Fig. 8. "Quadrature" energy kick as a function of frequency, for $X = a/2$, $Y = 0$; and two values of θ. These curves are the same for all values of τ.

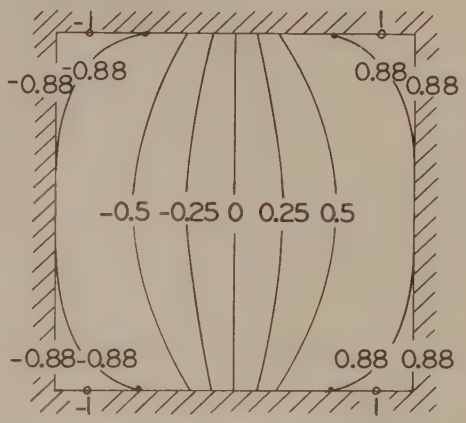

Fig. 9. Distribution of the "quadrature" energy kick throughout a square cross-section. Parameters: $\theta = 60°$, $\nu = 0.5$, $v = \frac{1}{3}c$. Curves labeled in units of qV.

that its existence can, in consequence, be ascribed to the presence of a slant angle. The frequency dependence of V_2, for particles moving along the center of the narrow wall of the duct, is depicted in fig. 8. The variation of V_2 throughout the cross-section, for an extreme set of

4. Lateral Momentum Kick Calculations

The lateral momentum kick is given by the formula

$$\Delta \boldsymbol{p}\,(X, Y) = q \int_{-\infty}^{+\infty} \boldsymbol{E}_{\text{transv.}}\,(X, Y, Z, t)\,\mathrm{d}t + q\mu_0 v \int_{-\infty}^{+\infty} [\boldsymbol{u}_Z \times \boldsymbol{H}\,(X, Y, Z, t)]\,\mathrm{d}t = \frac{qV}{C}\,\boldsymbol{p}_1 \cos\varphi + \frac{qV}{C}\,\boldsymbol{p}_2 \sin\varphi$$

where $\boldsymbol{p}_1$, the "in phase" momentum kick expressed in units of qV/c, is equal to

$$\boldsymbol{p}_1\,(X, Y) = \frac{16\nu}{\pi^2} \sin\left(\operatorname{tg}\theta\,\frac{\nu}{\beta}\,\frac{\pi}{2}\right) \left\{ \boldsymbol{u}_X \sum_{m=0,2}^{\infty} \sum_{n=1,3}^{\infty} \frac{(-1)^{\frac{m+n+1}{2}} \cos\dfrac{m\pi X}{a} \cos\dfrac{n\pi Y}{b}}{\varepsilon_m \cdot n \cdot \left[m^2 + n^2\tau^2 + \left(\dfrac{1}{\beta^2} - 1\right)\nu^2\right]} \cdot \left[\frac{1}{\beta^2} - 1 - \frac{n^2\tau^2 \operatorname{tg}^2\theta}{m^2 - \left(\operatorname{tg}\theta\,\dfrac{\nu}{\beta}\right)^2}\right] \right.$$

$$\left. - \boldsymbol{u}_Y \cdot \tau \cdot \left(\frac{1}{\beta^2} + \frac{\operatorname{tg}^2\theta}{\beta^2} - 1\right) \sum_{m=0,2}^{\infty} \sum_{n=1,3}^{\infty} \frac{(-1)^{\frac{m+n+1}{2}} \cdot m \cdot \sin\dfrac{m\pi X}{a} \cdot \sin\dfrac{n\pi Y}{b}}{\varepsilon_m \left[m^2 + n^2\tau^2 + \nu^2\left(\dfrac{1}{\beta^2} - 1\right)\right]\left[m^2 - \left(\dfrac{\nu \operatorname{tg}\theta}{\beta}\right)^2\right]} \right\}, \tag{4}$$

ε_m is Neumann's factor, equal to 2 for $m = 0$, to 1 for $m = 1, 2, 3, \ldots$

The "quadrature" momentum kick, on the other hand, turns out to be

$$\boldsymbol{p}_2(X, Y) = \frac{16\,\nu}{\pi^2}\cos\left(\operatorname{tg}\theta\,\frac{\nu\pi}{\beta\,2}\right)\left\{\boldsymbol{u}_X \sum_{m=1,3}^{\infty}\sum_{n=1,3}^{\infty}\frac{(-1)^{\frac{m+n}{2}}\sin\frac{m\pi X}{a}\cos\frac{n\pi Y}{b}}{n\left[m^2+n^2\tau^2+\left(\frac{1}{\beta^2}-1\right)\nu^2\right]}\left[\frac{1}{\beta^2}-1-\frac{n^2\tau^2\operatorname{tg}^2\theta}{\beta^2\left[m^2-\left(\operatorname{tg}\theta\,\frac{\nu}{\beta}\right)^2\right]}\right]\right.$$

$$\left.+\,\boldsymbol{u}_Y\cdot\tau\cdot\left(\frac{1}{\beta^2}+\frac{\operatorname{tg}^2\theta}{\beta^2}-1\right)\sum_{m=1,3}^{\infty}\sum_{n=1,3}^{\infty}\frac{(-1)^{\frac{m+n}{2}}\cdot m\cdot\cos\cdot\frac{m\pi X}{a}\sin\frac{n\pi Y}{b}}{\left[m^2+n^2\tau^2+\nu^2\left(\frac{1}{\beta^2}-1\right)\right]\left[m^2-\left(\operatorname{tg}\theta\,\frac{\nu}{\beta}\right)^2\right]}\right\}. \qquad (5)$$

The lateral momentum kick in the center of the guide is of particular interest. Eqs. (4) and (5) show that it consists of an "in phase" component only, that its direction is parallel to the broad wall of the guide, and that its magnitude decreases with the slant angle of the gap. Its frequency dependence is plotted in fig. 10. A conclusion already reached in the analysis of the voltage kick can be confirmed here: the δ-function approximation is good as long as sufficiently high velocities and low frequencies are considered. To emphasize this conclusion still more, the variation of $\boldsymbol{p}_1$ throughout a square cross-section is shown in fig. 11 for a rather extreme set of parameters. The actual value of the momentum kick, as given in this figure, is far from the value predicted by the δ-function approximation. The latter value is, in particular, independent of the Y coordinate, a result which is not confirmed by the exact analysis.

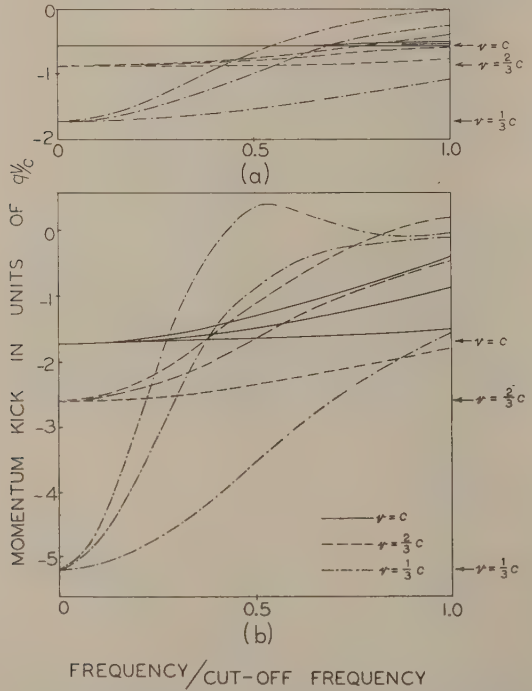

Fig. 10. X component of the "in phase" momentum kick along the main axis $X = Y = 0$, for three velocities and for (a) $\theta = 30°$, (b) $\theta = 60°$. The three curves of each family correspond, reading down from the uppermost, to $\tau = 1$, 2, 5. The arrows indicate the value predicted by the δ-function approximation.

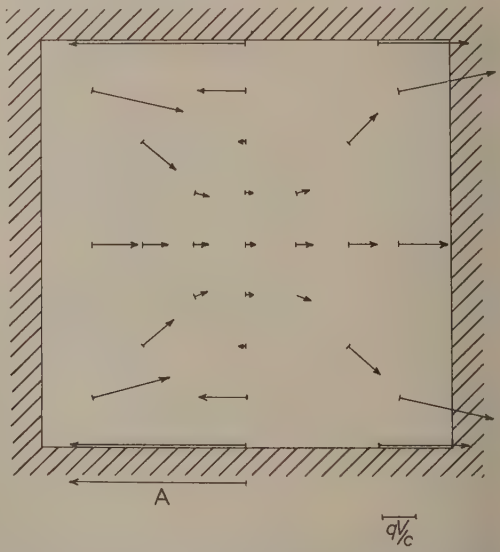

Fig. 11. "In phase" lateral momentum kick for $\theta = 60°$, $v = 0.5$, $v = \frac{2}{3}c$. The arrow bearing the indication "A" indicates the value which the δ-function approximation predicts for points located on the OY axis.

The δ-function approximation predicts that the lateral momentum kick vanishes for a gap perpendicular to the axis. An exact analysis, on the contrary, shows that, because of the presence of magnetic forces, the quadrature momentum kick does not vanish under these

conditions. Its frequency dependence, for points located halfway towards the walls on the O X and OY axes, is depicted in fig. 12. The kick vanishes everywhere for particles traveling at the velocity of light, this in accordance with a very general property established elsewhere[6]). It will be noticed, from fig. 12, that the momentum kick at points located on the OX axis rapidly becomes negligible as the cross-section becomes flatter and flatter. This is not true, however, fo

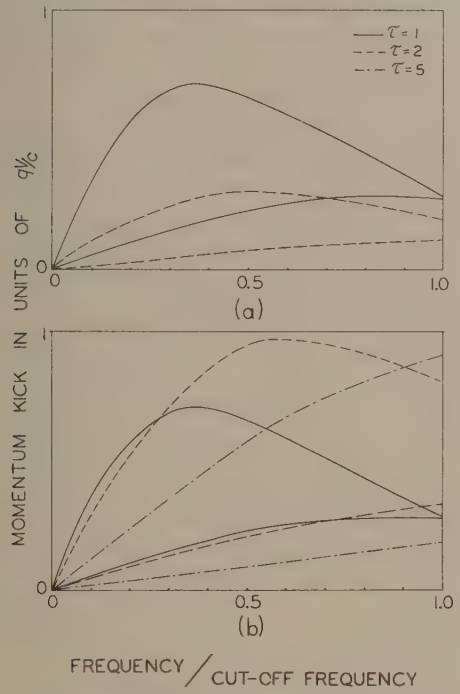

Fig. 12. "Quadrature" lateral momentum kick for $\theta = 0°$, $\nu = 0.5$, $v = \frac{3}{5}c$ and (a) $X = a/4$ $Y = 0$, (b) $X = 0$ $Y = b/4$. Each aspect ratio is represented by two curves, the upper curve corresponds to $v = \frac{1}{5}c$, the lower curve to $v = \frac{3}{5}c$. The momentum kick for $\tau = 5$, in fig. 12a, is too small to be plotted with accuracy, and has been omitted.

points located on the OY axis, a consideration of importance with the flat "doughnuts" used in the design of the MURA machine. Finally, the variation of the quadrature momentum kick throughout a square cross-section is shown in fig. 13 for a representative set of parameters. There, again, a gap perpendicular to the main axis is considered (space limitations forbid inclusion of more data on slanted gaps).

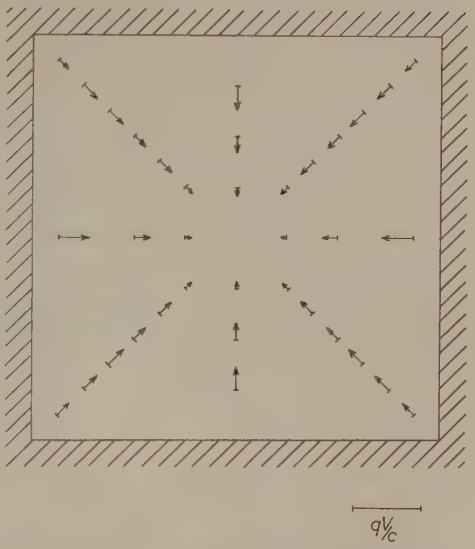

Fig. 13. "Quadrature" lateral momentum kick for $\nu = 0.5$, $v = \frac{3}{5}c$ and $\theta = 0°$. The particles cross the plane of the gap at the moment the gap voltage goes through zero.

5. Conclusion

The constancy of voltage phase and amplitude all along the gap contour is not realized with the driving systems commonly encountered in practice (e.g. the single coaxial line driving the gap in one point). The main qualitative results of the present analysis should still remain valid, however, for instance: that the omission of magnetic field effects, and the assumption of a δ-function behavior for the electric field, yield acceptable results only in the limit of low frequencies and high velocities. Figs. 6 to 13 give an idea of the errors introduced by these simplifying assumptions. One result of particular importance was the existence of a lateral momentum kick in circumstances where the δ-function approximation predicted its absence. This fact should be kept in mind when R.F. knockout and betatron oscillations problems are considered.

6. Acknowledgment

The lengthy calculations supporting the numerical data of this paper have been very ably programmed by Mr. J. McNall on MURA's IBM 704 computer.

NUCLEAR INSTRUMENTS 3 (1958) 116–118; NORTH-HOLLAND PUBLISHING CO. – AMSTERDAM

20 Mc/s SCALING CIRCUIT

B. COLLINGE and G. B. HUXTABLE

Nuclear Physics Research Laboratory, Liverpool 3

Received 25 March 1958

A scaling circuit is described which will operate at frequencies greater than 20 Mc/s. Particular attention is paid to reliable triggering.

1. General

Fast scale of two circuits are required in many applications: frequency meters, time interval measuring equipment, high speed data processing and particle counting in nuclear physics experiments.

The speed of operation of the conventional Eccles-Jordon trigger circuit, shown in fig. 1,

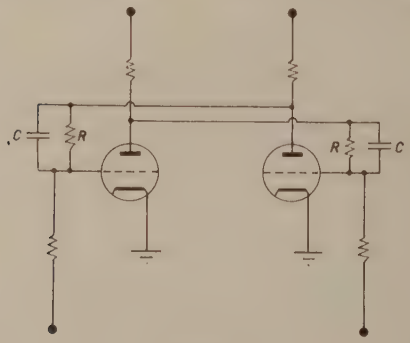

Fig. 1

may be increased by the use of peaking coils clamping diodes and coupling cathode followers[1,2]). These circuits require close tolerance design and may be rather complicated. If secondary emitting pentodes are used then a very fast scaling circuit[3]) is possible but in which there is difficulty in stabilising the quiescent current.

However the principal difficulty in achieving high speed operation is that of obtaining reliable triggering. In order to achieve this it is necessary to make the value of the time constant CR, shown in fig. 1, larger than the value needed to make the resistance network frequency independent. This time constant then provides a memory and the circuit, during a transition form one stable state to the other, uses this memory to achieve reliable triggering. However, if a scale of two is designed for fast operation

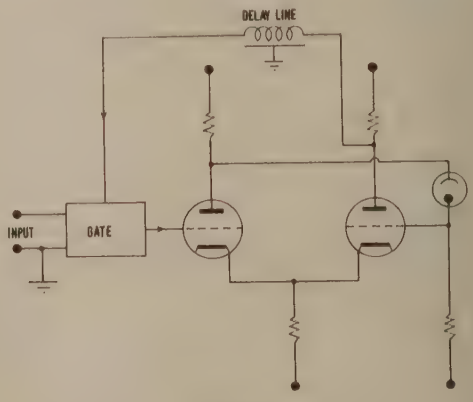

Fig. 2

then the value of C must be reduced in order to keep the anode capacity small. Thus high speed operation and reliable triggering are mutually exclusive and the situation becomes very difficult when operating frequencies greater than 10 Mc/s are attempted.

This circuit described here makes use of a

[1]) B. Chance, V. Hughes, E. F. Mac Nichol, D. Sayre and F. C. Williams, Waveforms (Mc Graw Hill Publishing Company Inc., New York, 1949) Radiation Laboratory, Series 19.

[2]) M. Nakamura, Rev. Sci. Inst. 28 (1957) 1015.

[3]) J. Fischer and J. Marshal, A Ten-Millimicrosecond Scaler, Proc. Natl. Electronics Conf. 9 (1954).

delay line to provide a memory of the previous history of the circuit. Triggering is found to be more reliable than that of conventional circuits.

The principle of the circuit is shown in fig. 2. The scale of two consists of a cathode coupled flip-flop circuit. The bias is arranged so that the circuit has two stable states and pulses of alternate sign are required at the left hand control grid to change the state of the circuit. These pulses are provided by the gate circuit. The polarity of the pulse from the gate is decided by the state of the scale of two which is D.C. connected to the gate. If the input pulses to the gate have a duration which is shorter than the delay line, then the gate is switched after an input pulse and after the scale of two has reached its new state. The triggering action is thus quite positive.

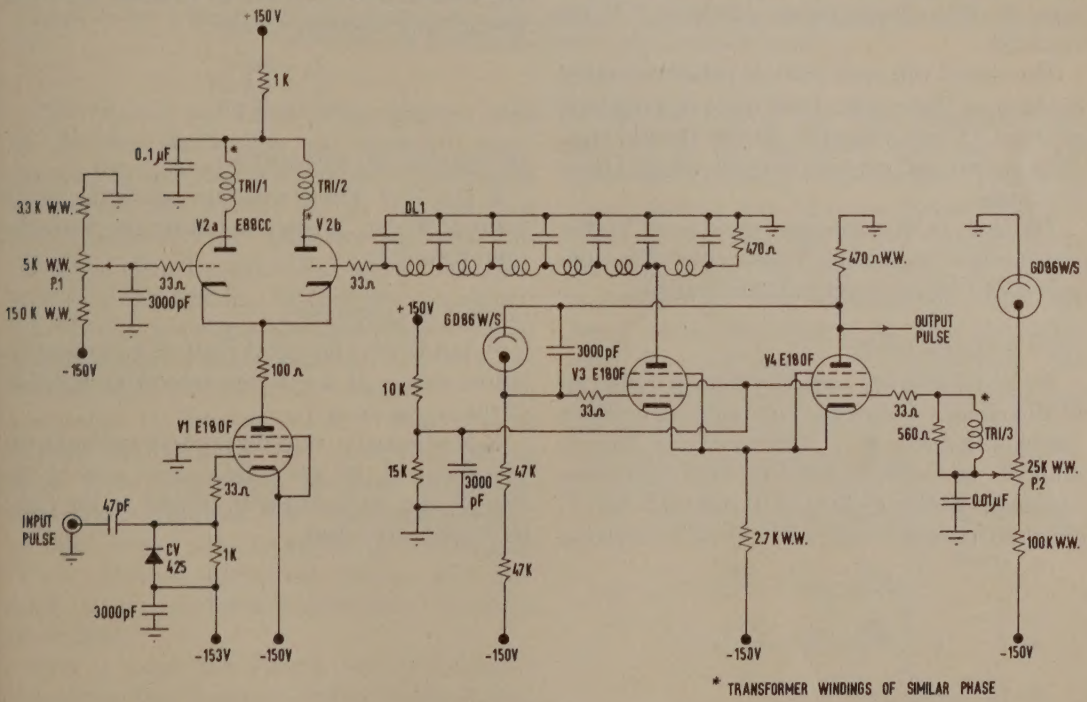

Fig. 3

2. Scale of Two Circuit

2.1. GATE CIRCUIT

A complete scale of two circuit is shown in fig. 3. The gate consists of V_1 and V_2. Positive input pulses are fed on to the control grid of V_1 and each pulse turns on a current of about 50 mA in the common cathode lead of the double triode V_2. The D.C. connection from the scale of two, which consists of valves V_3 and V_4, biases V_{2b} so that this current flows in the anode circuit of V_{2a} or V_{2b} and hence through one or other of the primary windings of the transformer TR_1. Because the primary windings are in opposite phase, the pulse across the secondary, which is connected to the triggering grid of the scale of two, has a polarity which depends on the state of the scale of two. Therefore, every input pulse at the gate, produces a pulse of the correct sign at the input grid of the scale of two which then changes its state.

The valves in the gate circuit are normally not conducting and so large peak currents are possible. This allows wide band transformers to be used.

2.2. SCALE OF TWO CIRCUIT

The scale of two consists of two cathode

coupled video pentodes. The cross connection from anode to grid is by means of a neon lamp and there is no loss of signal amplitude from the anode of V_3 to the grid of V_4. The value of anode load is therefore small and the time constant is of the order of 10 mμs. The delay line which controls the gate circuit is 25 mμs long and so the gate is switched after the scale of two has reached a steday state.

2.3. PERFORMANCE

The scale of two circuit and the gate shown in fig. 3 will scale continuously at a frequency of at least 20 Mc/s. Input pulses of about 5 V are required.

The circuit will scale pairs of pulses separated by 40 mμs. These pulses must have an amplitude of about 5 V and a duration greater than 10 mμs. Rectangular and exponential pulse shapes have been used.

The limit to the switching speed is set by the transformer bandwidths. Transformers free from over shoot would result in faster scaling.

2.4. A SCALE OF FOUR

A scale of four has been constructed using two of the circuits described. The coupling between stages consisted of a differentiating circuit, amplifier and cathode follower. This circuit was capable of scaling at 20 Mc/s. It has been used to drive a trochotron scale of 100 with a resolving time of about 0.1 μs. This circuit has been used in experimental equipment designed for use with the Liverpool University Synchrocyclotron.

3. Acknowledgment

The authors wish to thank Mr. F. H. Wells of A.E.R.E. Harwell for a most helpful discussion on fast scaling circuits and Mr. D. F. Scott who constructed and tested the circuits.

4. Appendix

DETAILS OF LUMPED DELAY LINE

DL 1 consists of 6 sections of 25 turns of 34 swg wound on $\frac{1}{4}''$ distrene former.

$$Z_0 = 500\,\Omega$$
$$L = 2.5\,\mu\text{H}$$
$$C = 10\,\text{pF}.$$

DETAILS OF TRANSFORMER T_1

T 1/1, 2, 3. Three windings consisting of 20 turns of 36 swg. Wound on ferroxcube pot cores type FX 1011.

CIRCUIT ADJUSTMENTS

P_1 is adjusted for equal positive and negative pulses measured across the secondary winding of the transformer T_1.

P_2 is adjusted so that the positive and negative excursions of the left hand control grid of the trigger pair, measured with respect to the right hand grid, are equal.

NUCLEAR INSTRUMENTS 3 (1958) 119–120; NORTH-HOLLAND PUBLISHING CO. – AMSTERDAM

NOTES TO THE EDITOR

UMWANDLUNG EINES IM BINÄREN ZAHLENSYSTEM ANGEZEIGTEN IMPULSHÖHENSPEKTRUMS IN EINE REGISTRIERTE KURVE†

S. WAGNER

Physikalisch-Technische Bundesanstalt, Braunschweig

Received 21 April 1958

A simple method is described allowing to transform a pulse spectrum pattern displayed as binary numbers on a cathode ray screen of a multichannel analyzer into a recorded curve.

Zur Analyse von Impulshöhenspektren wird oft der von Hutchinson und Scarrott[1]) angegebene Vielkanalanalysator benutzt. Bei diesem Gerät wird die Anzahl der in die einzelnen Impulshöhenintervalle (Kanäle) sortierten Impulse auf dem Leuchtschirm einer Kathodenstrahlröhre im binären Zahlensystem angezeigt, d.h. über der jeweiligen Kanalzahl (entsprechend einer bestimmten Horizontalablenkung des Elektronenstrahls) erscheinen als schwach oder stark leuchtende Punkte die Stellen (0 oder 1) einer binären Zahl (Abb. 2). Die Auswertung der auf diese Weise angezeigten Spektren ist im allgemeinen zeitraubend. Für viele Zwecke genügt es aber, wenn das Spektrum in Form einer Kurve vorliegt, deren schrittweise Aufzeichnung das im folgenden beschriebene Verfahren ermöglicht.

Abb. 1 zeigt das Prinzip der verwendeten Schaltung. Den einzelnen Stellen einer auf dem Leuchtschirm angezeigten binären Zahl, die übertragen werden soll, sind Tasten zugeordnet, bei deren Betätigung geeignet gewählte Widerstände (R_1 bis R_{10}), die sich wie $1:2:4:\ldots 2^9$ verhalten, in der Weise parallel geschaltet werden, dass durch den Widerstand R_{12} ein dem Wert der Zahl proportionaler Storm fliesst. Sobald alle Stellen einer Zahl eingetastet sind, wird die an R_{12} abfallende Spannung U_m mit Hilfe eines Kompensationsschreibers†† gemessen und registriert. Der Kompensationsschreiber ist dabei so geschaltet, dass er den Quotienten aus den Spannungen U_m und $U_s = U_e\ R_{14}/(R_{13} + R_{14})$ registriert, damit Schwankungen von U_e die Anzeige nicht beeinflussen. R_{11} dient zur Definition des Nullpunktes im Schreiber[2]). Der Registriervorgang verläuft im einzelnen so, dass

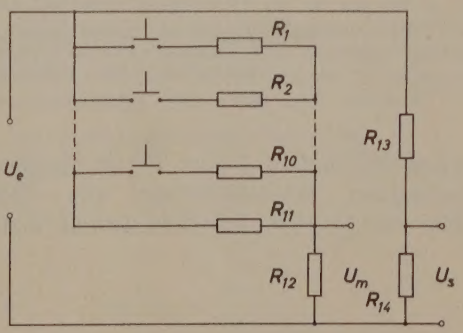

Abb. 1. Prinzip der Schaltung.

U_e zunächst abgeschaltet ist, während die Zahl eingetastet wird. Dabei werden nur diejenigen Tasten gedrückt, die den als "Eins" angezeigten Stellen der binären Zahl entsprechen. Dann

† Mitteilung aus der Physikalisch-Technischen Bundesanstalt.

†† Grundsätzlich können zu diesem Zweck auch andere registrierende Messgeräte verwendet werden.

[1]) G. W. Hutchinson und G. G. Scarrott, Phil. Mag 42 (1951) 792.

[2]) R. L. Gordon, J. sci. Instr. 30 (1954) 431.

wird U_e eingeschaltet, der Kompensator gleicht ab und der Papiervorschub läuft an (ggf. um die Abgleichzeit verzögert). Ein Schaltrad am Papiervorschub schaltet U_e wieder ab, wirft die Tasten aus und beendet den Vorschub nach

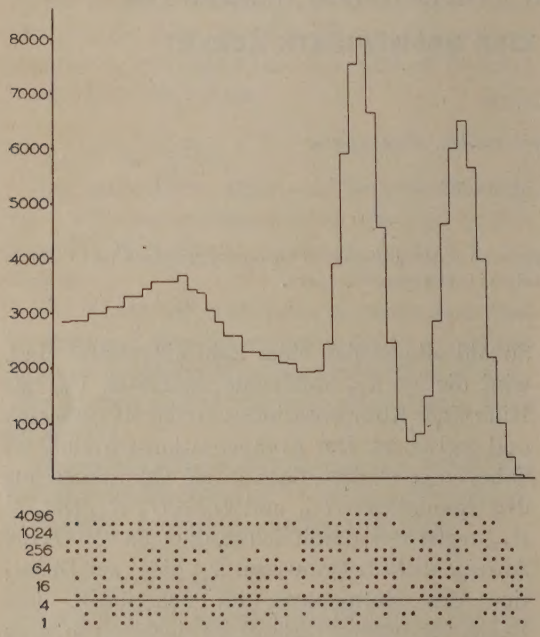

Abb. 2. Beispiel für die Übertragung eines Spektrums. (Ausschnitt aus einem ^{60}Co-Spektrum.) *Unten*: Anzeige auf dem Leuchtschirm der Kathodenstrahlröhre des Vielkanalanalysators im binären Zahlensystem (freie Stelle–Null, •-Eins). *Oben:* Übertragenes Spektrum.

wenigen Millimetern. Einige Relais führen die verschiedenen Schaltfunktionen aus. Dieser Zyklus wird für jeden Kanal wiederholt, so dass sich ein stufenförmiger Kurvenzug† ergibt (Abb. 2).

In dem Gerät werden Magnettasten verwendet, die in Blockform angeordnet sind, so dass sie blind bedient werden können. Die Einstellzeit des Kompensationsschreibers beträgt im vorliegenden Fall maximal 1 s, die Papiervorschubgeschwindigkeit 2400 mm/h (Schreibbreite 250 mm). Auf jeden Kanal des Analysators entfällt eine Registrierlänge von 3 mm. Zusammen mit der Eintastung ergibt sich auf diese Weise eine Registrierdauer von etwa 6 s pro Kanal††.

Insgesamt sind 10 Tasten vorhanden, so dass 1023 die höchste einstellbare Zahl ist. Bei Verwendung geeigneter Messwiderstände und bei einer Unsicherheit der Anzeige von maximal $\pm$ 0.2% (Einstellunsicherheit + Linearitätsabweichung) ergibt sich eine Gesamtunsicherheit von weniger als 0.5%. Der relative statistische Fehler kann dadurch klein gemacht werden, dass pro Kanal entsprechend viele Impulse analysiert, aber nur die wesentlichen Stellen der Impulszahl zur Auswertung herangezogen werden, (das sind die Stellen oberhalb der horizontalen Linie in Abb. 2).

Ich danke Herrn Ing. H. J. Barrenscheen für seine wertvolle Mitarbeit sehr.

† Bei Verwendung eines Punktdruckers anstelle eines Linienschreibers würde sich eine Punktfolge ergeben.

†† Diese Zeit kann dadurch noch verkürzt werden, dass nach dem Abgleich des Kompensators bereits die nächste Zahl eingetastet wird, während der Schreiber noch die vorhergehende registriert; U_e ist dabei abgeschaltet.